# MOLECULAR DYNAMICS SIMULATIONS AND MICROSCOPIC HYDRODYNAMICS OF NANOSCALE LIQUID STRUCTURES

A Thesis
Presented to
The Academic Faculty

by

Wei Kang

In Partial Fulfillment
of the Requirements for the Degree
Doctor of Philosophy in the
School of Physics

Georgia Institute of Technology
April 2008

# MOLECULAR DYNAMICS SIMULATIONS AND MICROSCOPIC HYDRODYNAMICS OF NANOSCALE LIQUID STRUCTURES

Approved by:


Professor Uzi Landman, Advisor
School of Physics
*Georgia Institute of Technology*

Professor Mei-Yin Chou
School of Physics
*Georgia Institute of Technology*

Professor Ari Glezer
School of Mechanical Engineering
*Georgia Institute of Technology*

Doctor W. D. Luedtke
School of Physics
*Georgia Institute of Technology*

Doctor Jianping Gao
School of Physics
*Georgia Institute of Technology*



Date Approved: January 24, 2008

*To my parents,*

*who teach me observing the world with my own eyes.*

# ACKNOWLEDGEMENTS

First, I would like to express my deep and sincere gratitude to my advisor Professor Uzi Landman, for his broad vision, deep insight, and sparking inspiration throughout the entire course of my PhD study.

I'm deeply indebted to Dr. W. D. Luedtke and and Dr. Jianping Gao for their stimulating discussions and unselfish helps.

I also would like to thank all the other members of the Computational Material Science Center for their helps and discussions.

Finally, I want to thank my wife Zhu Ma. Her love and understanding have been supporting me all these difficult years.

# TABLE OF CONTENTS

# LIST OF TABLES

# LIST OF FIGURES

# SUMMARY

The dynamics of liquid structures is of fundamental interest in both theoretical investigations and industrial applications. Self-similarity, scaling, and pattern formation phenomena taking place in a variety of liquid structures have attracted attention for a long time. Many applications, such as ink-jet printing, spraying and fuel injection are based to the dynamics of liquid structures. The size of liquid structures in present-day applications is rapidly decreasing, even to the scale where macroscopic hydrodynamical equations may break down so that understanding the hydrodynamics in the microscale is becoming an increasingly important subject.

In this thesis, issues pertaining to the dynamics of nanoscale liquid systems, such as nanojets and nanobridges, in vacuum as well as in ambient gaseous conditions, are explored using both extensive molecular dynamics simulations and theoretical analyses. The simulation results serve as "theoretical experimental data" (together with laboratory experiments when available) for the formulation, implementation, and testing of modified hydrodynamic formulations, including stochastic hydrodynamics. These investigations aim at extending hydrodynamic formulations to the nanoscale regime. In particular, the instability, and breakup of liquid nanobridges and nanojets are addressed in details. As an application of the microscopic hydrodynamics, a heated-nozzle technique to generate and control nanojets is proposed. Both simulations and microscopic hydrodynamic modeling reveal the formation of a "virtual convergent nozzle", which consists of a narrowing convergent liquid core within a growing evaporative sheath, by the nanojet itself inside the real nozzle. The diameter of the resulting ejected nanojet is much smaller than the diameter of the

nozzle. By adjusting the temperature distribution of the real nozzle, the size and shape of the virtual nozzle are changed, which in turn changes the diameter and the direction of the ejected nanojet.

# CHAPTER I

# INTRODUCTION

Fluid mechanics and hydrodynamics are a practical subject with a long history over several thousand years and their applications can be found in every corner of our society from households to hi-tech industries. A good example for this is Archimedes' principle on buoyancy, discovered by Archimedes (ca. 287 BC – ca. 212 BC) over two thousand years ago, and even now we still make use of this principle to cook as well as to build ships. Traditionally, fluid mechanics and hydrodynamics are associated with macroscopic concepts. A fluid is considered as a continuous medium. Every infinitesimal volume element of it comprises a great number of particles [48]. The basic equations of motion for fluids are macroscopic conservation laws of momentum (Navier-Stokes equations) and mass (continuity equation) supplemented with an energy equation and the equation of state of the fluid materials in question.

Compared with fluid mechanics and hydrodynamics, molecular dynamics simulation is a brand new phenomenon. It emerged with the development of modern electronic computers. The first article on molecular dynamics simulation appeared in 1957 [5]. Molecular dynamics simulation is essentially a microscopic method. In this method, material is considered comprising microscopic particles (molecules or atoms). From a given initial configuration of all the particles, the molecular dynamics simulation method calculates the subsequent trajectories of the entire material. Macroscopic properties of the material are extracted from the particles' trajectories through statistical mechanics [74]. When the microscopic physical properties (such as the mass and the geometrical shape) of the particles and the interactions between them are specified, the trajectory of each particle is the solution of the equation of

motion (usually Newtonian), which is solved by a digital computer.

The combination of hydrodynamics (fluid mechanics) and molecular dynamics simulation has occurred only in the last few decades in the studies of mesoscopic (nanoscale) motion of fluids. The molecular dynamics simulation acts as a computational experiment which aims to find new phenomena and provide verification to hydrodynamical theory; while hydrodynamics (fluid mechanics), with corrections from fluctuations and other microscopic processes, provides theoretical explanations to the observed phenomena and also provides new predictions for further verification. The advance of the molecular dynamics simulation method is closely correlated with the development of computational techniques. Early molecular dynamics simulations [34, 42] could only provide qualitative results to the dynamical process of liquid structures composed of several thousand particles, while recent studies [55, 40, 39] are able to provide detailed quantitative hydrodynamical information for liquid structures composed of over a million particles. A theoretical breakthrough occurred in the year 2000, when a set of stochastic lubrication equations (SLE) were proposed by Moseler and Landman [55] based on the detailed information provided by their large-scale molecular dynamics simulations of nanojets. The stochastic lubrication equations revealed one of the important aspects of microscopic hydrodynamics, i.e., thermal fluctuations change the dynamical process of a liquid structure at the nanoscale.

In this thesis, we study several aspects of the microscopic hydrodynamics of nanoscale liquid structures using both molecular dynamics simulations and stochastic lubrication equations. In the study of the pinching dynamics of a liquid nanobridge in vacuum, the break-up process of a liquid propane nanobridge is investigated using molecular dynamics simulations and scaling analysis based on the stochastic lubrication equations. A double-cone self-similar break-up profile originating from thermal fluctuations is observed in the simulations. Scaling analysis reveals that the liquid nano-bridge breaks up according to a power law with an exponent of 0.375, which is

in accordance with the simulation result of $0.40 \pm 0.02$.

In the study of the pinching process of nanobridges of a large size in vacuum, we focus on the size-dependent influence of thermal fluctuations in a nanobridge, and on the validity of the lubrication approximation in nano-liquid structures. Using molecular dynamics simulations, we show how thermal fluctuations eliminate the influence of the initial configuration of a large nanobridge. Without thermal fluctuations, the influence is observed in the entire pinching process and the self-similar pinching profile is difficult to capture. The validity of the lubrication approximation in an axisymmetrical flow is verified, and furthermore, we observe that the approximation can be applied without the validity of the slenderness assumption, which is normally considered a prerequisite condition for the application of the lubrication approximation.

Because of the importance of instabilities of nanoscale liquid structures in the application of microscopic flows, we study the linear instability of a long liquid cylinder with a uniform diameter using both molecular dynamics simulations and theoretical analysis. The growth rate of unstable modes is determined from the simulation data and is compared with theoretical hydrodynamical predictions. It is revealed that the instability emerges first in the interfacial surface layer of the nanobridge with a much smaller growth rate than that predicted by the theory, and that thermal fluctuations generate stable fine structures on the surface of the nanobridge. These results provide an atomic-scaled picture to the origin of the hydrodynamic Rayleigh instability.

In real applications, liquid structures are surrounded by a gaseous environment. As a prototype, we study nanobridges in a nitrogen gaseous environment of various pressures. Molecular dynamics simulations show that under sufficiently high pressure, a long-thread break-up profile develops with an asymmetric shape. The emergence of a long-thread profile, which also occurs in the break-up process of a macroscopic flow, originates from the evaporation-condensation process of the nanobridge in the

surrounding gas. In the theoretical analysis, the evaporation-condensation process is formulated as a term proportional to the local curvature of the liquid structure in our modified stochastic hydrodynamics description based on stochastic lubrication equations.

We also demonstrate in the thesis, through molecular dynamics simulation, a new technique of generating and controlling liquid nanojets. In this technique, liquid is forced through a long cylindrical nozzle at a temperature much higher than the boiling point of the liquid. A virtual convergent nozzle is formed by the liquid itself near the exit of the tube. When the liquid is ejected from the exit, a nanojet with a much smaller diameter is formed, with its outer layer exhausted by strong evaporation. The essence of the technique is well described by a continuous hydrodynamical model. Also, we show that by adjusting the temperature distribution of the nozzle, the direction of the nanojet can be deflected in a controllable way.

# CHAPTER II

# MOLECULAR DYNAMICS SIMULATION

Usually, molecular dynamics (MD) refers to the computational method that calculates statistical properties of an ensemble of particles by tracking the trajectories of each particle in the system. This idea is a combination of the old mechanistic tradition dating back to Pierre Simon de Laplace and the new concept of atoms (as well as molecules) revealed at the beginning of the 20th century. The molecular dynamics method began to thrive with the development of modern digital computers, first in the studies of equilibrium properties of liquid composed of hard spheres [5, 6], while today it is applied in various disciplines from physics [56] to biology. Since the molecular dynamics method is often used as a digital experiment or simulation of real materials and systems, it is often known as the molecular dynamics "simulation".

In a molecular dynamics simulation, the system under study is modeled as an ensemble of interacting particles, including molecules, fractions of molecules, and atoms. The dynamics of the system is well approximated by the classical motion of the molecules' nuclei [10], which are considered as mass points and their motion is governed by the Newtonian equations of motion. The mathematical formula of their interactions depends on the type of particles involved. In most cases it is a potential (or mathematically a functional) of all the nuclei's positions. For a system composed of N particles, the equations of motion are

$$m_i \dot{\mathbf{v}}_i = -\frac{\partial}{\partial \mathbf{r}_i} U(\sum_{j=1}^{N} \mathbf{r}_j), \qquad i = 1, 2, \ldots, N \tag{2.1}$$

$$\dot{\mathbf{r}}_i = \mathbf{v}_i, \qquad i = 1, 2, \ldots, N \tag{2.2}$$

where $m_i$ is the mass of the $i$-th particle, $\mathbf{r}_i$ is its position, $\mathbf{v}_i$ is the velocity, and

$U(\sum_{i=1}^{N} \mathbf{r}_i)$ is the interaction potential of the entire system. Note that both $\mathbf{r}_i$ and $\mathbf{v}_i$ here are three-dimensional vectors. In this way, the dynamics of the system is depicted by the 6N first-order Newtonian ordinary differential equations. However, it is very often that the analytic solutions to the 6N ordinary equations are not available; and only numerical solutions can be obtained to some systems with a modest particle number N, with the help of modern computers.

There are two ingredients to conduct a successful molecular dynamics simulation for real materials: (1) robust and efficient numerical algorithms which solve the 6N Newtonian ordinary differential equations, and (2) sophisticated potentials which depict the interactions between particles accurately. In the rest of this chapter, these two ingredients are discussed in details.

## *2.1 Algorithms for molecular dynamics simulations*

In the section, we concentrate on the numerical algorithms that carries out the molecular dynamics simulations. Two issues pertaining to the algorithms will be addressed here. One is the algorithms that are able to integrate the 6N ordinary differential equations with required accuracy (or in a desired manner); the other is techniques that accelerate the algorithms.

### 2.1.1 Verlet algorithm and its variants

In the molecular dynamics, the Newtonian equations of motion are integrated using finite difference methods. However, since the system comprises a large number of particles, the choice for the appropriate algorithms is very limited. There are several criteria applied to the choice [56]. Among them, most importantly, is that the algorithm is fast and conserves the total energy well. The Verlet algorithm [86] is one of those desirable algorithms. It was first employed by Verlet for a Lennard-Jones

system in 1967. The original form of the Verlet algorithm is [56]

$$\mathbf{r}_i(t+\delta t) = 2\mathbf{r}_i(t) - \mathbf{r}_i(t-\delta t) + \delta t^2 \frac{\mathbf{f}_i(t)}{m_i}, \qquad i = 1, 2, \ldots, N \tag{2.3}$$

where

$$\mathbf{f}_i(t) = -\frac{\partial}{\partial \mathbf{r}_i} U(\sum_{j=1}^{N} \mathbf{r}_j) \tag{2.4}$$

is the total force on the $i$-th particle and $\delta t$ is the time step for each integration. Note that, in this form the Verlet algorithm directly integrates the 3N second order Newtonian equations of motion with no velocity appearing in the formula, and the velocity of each particle is obtained by an extra finite difference formula along the trajectories. For example [56],

$$\mathbf{v}_i(t) = \frac{\mathbf{r}_i(t+\delta t) - \mathbf{r}_i(t-\delta t)}{2\delta t}. \tag{2.5}$$

In practice, a variant of the Verlet algorithm is more convenient for implementation. It is called "velocity Verlet" [87, 56] and was proposed by Swope, Andersen, Berens, and Wilson in 1982. With the velocity explicitly expressed, the formula for the "velocity Verlet" is [56],

$$\mathbf{r}_i(t+\delta t) = \mathbf{r}_i(t) + \delta t \mathbf{v}_i(t) + \frac{\delta t^2}{2m_i}\mathbf{f}_i(t), \tag{2.6}$$

$$\mathbf{v}_i(t+\delta t) = \mathbf{v}_i(t) + \frac{\delta t}{2m_i}\left[\mathbf{f}_i(t) + \mathbf{f}_i(t+\delta t)\right]. \tag{2.7}$$

It is easy to verify that the "velocity Verlet" algorithm is equivalent to the original form by replacing the velocity in Eq. (2.6) with

$$\mathbf{v}_i(t) = \frac{\mathbf{r}_i(t) - \mathbf{r}_i(t-\delta t)}{\delta t}. \tag{2.8}$$

The entire "velocity Verlet" algorithm is divided into three steps in programming. In each iteration $\mathbf{r}_i(t+\delta t)$ is first calculated through Eq. (2.6) and part of the velocity $\mathbf{v}_i(t+\delta t)$ is calculated as,

$$\mathbf{v}_i^{part}(t+\delta t) = \mathbf{v}_i(t) + \frac{\delta t}{2m_i}\mathbf{f}_i(t), \tag{2.9}$$

where, $\mathbf{f}_i(t)$ has been assessed in the previous iteration; then the force $\mathbf{f}_i(t+\delta t)$ of each particle in the new position $\mathbf{r}_i(t+\delta t)$ is calculated; finally, with the newly calculated force, the other part of the velocity $\mathbf{v}_i(t+\delta t)$ is calculated and added to Eq. (2.9) to get the entire $\mathbf{v}_i(t+\delta t)$ through

$$\mathbf{v}_i(t+\delta t) = \mathbf{v}_i^{part}(t+\delta t) + \frac{\delta t}{2m_i}\mathbf{f}_i(t+\delta t). \tag{2.10}$$

One of the advantages of the "velocity Verlet" algorithm is that it improves the accuracy of the velocity calculation. However, it is desirable for us mainly because this form is easily generalized to include Brownian dynamics.

### 2.1.2 Verlet-like algorithm for Brownian dynamics

On many occasions, Brownian dynamics is a simple and efficient way to thermalize a system or part of the system to a desired temperature. It is also used to carry out the first several picoseconds of integrations in a simulation to prevent numerical overflow when the initial configuration of the system is set up artificially . Very similar to the velocity Verlet algorithm, the formula for Brownian dynamics is [56],

$$\begin{aligned}
\mathbf{r}_i(t+\delta t) &= \mathbf{r}_i(t) + c_1\delta t\mathbf{v}_i(t) + c_2\frac{\delta t^2}{m_i}\mathbf{f}_i(t) + \delta\mathbf{r}_i^G, \\
\mathbf{v}_i(t+\delta t) &= c_0\mathbf{v}_i(t) + \frac{\delta t}{m_i}\left[(c_1-c_2)\mathbf{f}_i(t) + c_2\mathbf{f}_i(t+\delta t)\right] + \delta\mathbf{v}_i^G,
\end{aligned} \tag{2.11}$$

where $\delta\mathbf{r}_i^G$, $\delta\mathbf{v}_i^G$ are Gaussian random components, and

$$\begin{aligned}
c_0 &= e^{-\xi\delta t}, \\
c_1 &= (\xi\delta t)^{-1}(1-c_0), \\
c_2 &= (\xi\delta t)^{-1}(1-c_1).
\end{aligned} \tag{2.12}$$

In Eq. (2.12), $\xi$ is the friction constant of the system. The non-zero variances of $\delta\mathbf{r}^G$ and $\delta\mathbf{v}^G$ in Eq. (2.11) are

$$\begin{aligned}
\left\langle (\delta\mathbf{r}_{i,\alpha}^G)^2 \right\rangle &= \delta t^2 \frac{k_B T}{m_i} (\xi\delta t)^{-1} [2 - (\xi\delta t)^{-1}(3 - 4e^{-\xi\delta t} + e^{-2\xi\delta t})], \\
\left\langle (\delta\mathbf{v}_{i,\alpha}^G)^2 \right\rangle &= \frac{k_B T}{m_i}(1 - e^{-2\xi\delta t}), \\
\left\langle \delta\mathbf{r}_{i,\alpha}^G \delta\mathbf{v}_{i,\alpha}^G \right\rangle &= \delta t \frac{k_B T}{m_i} (\xi\delta t)^{-1}(1 - e^{-\xi\delta t})^2,
\end{aligned} \tag{2.13}$$

where, $k_B$ is the Boltzmann constant, $T$ is the temperature of the system, and $\alpha$ represents the x, y, and z components of the position or velocity.

### 2.1.3 Force calculation in the molecular dynamics simulation

In a molecular dynamics simulation, the force calculation is the most time consuming part. It often takes over 90% of the entire calculation time. There are many techniques devoted to improving the calculation of forces. These technical efforts can be divided into two categories. Some of the efforts reduce the particles involved in the interaction potential; while the others reduce the time in locating the particles in the interaction range of the force calculation.

Generally, the force on one of the particles comes from all other particles. However, since the interactions caused by particles at a large distance are weak, they can be either neglected or offset using statistical methods for numerical purposes. For the most commonly used short-range pair interaction, i.e., the Lennard-Jones 12-6 interaction,

$$U^{LJ}(r) = 4\epsilon \left[ \left(\frac{\sigma}{r}\right)^{12} - \left(\frac{\sigma}{r}\right)^{6} \right], \tag{2.14}$$

where $\epsilon$ is the depth of the attractive potential well, and $\sigma$ is the radius of the repulsive core; truncating the interaction at a distance $r_c$ is a good practice in many cases. Usually $r_c$ takes the value of $2.5\sigma$, where the potential decreases to about 1/60 of the potential depth $\epsilon$. Sometimes an offset for the cutoff is necessary. For example, in the study of the thermodynamical properties of Lennard-Jones liquids, the material

outside of the cutoff radius $r_c$ is considered as a continuous medium with a uniform number density equaling to the average density $\rho$ of the system. The compensation of the potential due to this part of material is [10],

$$U^{tail} = \frac{8}{3}\pi\rho\epsilon\sigma^3 \left[\frac{1}{3}\left(\frac{\sigma}{r_c}\right)^9 - \left(\frac{\sigma}{r_c}\right)^6\right]. \tag{2.15}$$

When the simulated system is small and periodic boundary conditions are assumed, a so-called "minimum image convention" method is an alternate to truncate the potential. With periodic boundary conditions, every particle in the system has infinite images (including itself) obtained by shifting its position multiple times of the system's length along the periodic boundaries. The "minimum image convention" suggests that the distance between two particles A and B the nearest distance between all the images of A and all the images of B. This can be expressed as,

$$d(\mathbf{r}_A, \mathbf{r}_B) = \min_{\mathbf{m},\mathbf{n}} \left\{|(\mathbf{r}_A + \mathbf{m}) - (\mathbf{r}_B + \mathbf{n})|\right\}, \tag{2.16}$$

where $\mathbf{r}_A$ and $\mathbf{r}_B$ are position vectors of particles $A$ and $B$ respectively; while $\mathbf{m}$ and $\mathbf{n}$ are lattice vectors representing the shifts along periodic boundaries.

In the cases of a large system with periodic boundary conditions, the combination of the cutoff method and the minimum image convention are often used to truncate the potential. For those particles at the vicinity of the boundary, the minimum image convention has to be employed to determine the distance between particle pairs crossing the boundary in order to apply the cutoff method. In the force calculation of other particles, the cutoff method is applied directly.

Ideally, the cutoff method only calculates the force from the particles within the cutoff radius. However, before that happens, we need to determine which particle is within the cutoff radius from the pool of all the particles. When the number of particles is large this selection procedure can be very time-consuming. For example, in the Lennard-Jones potential case, to calculate the force on a particular particle A, we need to locate all the particles within the distance $r_c$ to A. A simple way to

achieve this is (1) calculating the distance of particle A to all the other particles of the system and then (2) comparing them with the cutoff radius $r_c$. For a system of N particles, calculating the force on all the particles in the system requires $\frac{(N-1)N}{2}$ such distance calculations. This is an enormous computational cost when N is very large. There are two different techniques used to reduce the time cost in selecting particles. One is the technique of neighbor list, which was first used by Verlet [86]. The other is the technique of cell structure and linked lists [56].

In the neighbor list method, a list array denoted as "LIST" is built to record all the neighbors of each particle within the distance of $r_c + r_b$, where $r_b$ is the length of the buffer layer on the surface of the cutoff sphere. Meanwhile, an index table array denoted as "POINT" is constructed to point to the first neighbor of each particle. Since the neighbors of each particle are grouped together, their positions are located in the LIST array between the positions pointed by POINT(i) and POINT(i+1)-1, where i is the index of one of the N particles. In the simulation, the LIST array is updated each several steps, depending on the length of the buffer layer $r_b$. In practice, the update interval is usually 10-20 integration steps.

The cell structure and linked lists method is another way to track the neighbors of each particle. In this method, the entire simulation volume is divided into cubic cells of size $\Delta$; and similar to the neighbor list method, particles in each cell are linked into a list data structure and stored in the array denoted as "LIST". An index array called "HEAD" is constructed at the same time to point to the first particle of each cell. In the calculation, the LIST and HEAD arrays are updated each time before the force calculation. After determining which cell a particle lies in, the method searches all the particles in the cell and in the nearby cells to find out all the particles within the cut-off sphere. Note that the determination of which nearby cell may have particles in the cutoff sphere depends on both the cutoff radius $r_c$ and the cell size $\Delta$. This process is usually complicated, but fortunately, since the position of each cell is fixed,

those neighbor cells can be determined and tabulated once and for all at the beginning of the simulation. This method can also save a large fraction of computational time because the determination of the containing cells avoids the calculation of distance, which is much more expensive computationally.

### 2.1.4 Parallelization of the molecular dynamics simulation

Parallel methods allow us conduct molecular dynamics simulations on the latest supercomputers and make molecular dynamics simulations of billions of particles possible [40, 39]. With the development of computational techniques, a variety of parallel algorithms have been developed to carry out molecular dynamics simulations under different circumstances. In our simulations, the number of particles of the system can reach the order of $10^6$, and several types of materials such as metal, liquid and gas may co-exist; therefore, an appropriate parallel algorithm is crucial for the successful simulation.

In our molecular dynamics simulations, a force-decomposition method proposed by Plimpton [70] is adopted. Suppose the system has N particles and the computer has P processors, where P is an even power of 2. In this method, the N particles are partitioned into $\sqrt{P}$ groups and each group has $N/\sqrt{P}$ particles. The P processors are assembled into a matrix with each processor as an element denoted by a pair of numbers $(i, j)$, where $i, j = 1, 2, \ldots, \sqrt{P}$. Each processor has the positions of both the $i$-th and the $j$-th group of particles stored in it.

The sketch of the method is described as follows. First, in each iteration of the simulation the position and velocity of all the particles on each processor are updated using the force calculated in the previous iteration. Then, each processor calculates the force between the two partitions of particles stored in it. In this step, Newton's second law is often employed to further reduce the computational cost in the force calculation. Note that at this moment, the force obtained by each processor is only

a fraction of the total force of the particles. Following the force calculation, the total force of each particle is assembled through communications between processors. Finally (when the velocity Verlet algorithm is used) the third step of the velocity Verlet algorithm is carried out and accordingly, the velocity of the particles on each processor is updated. Detailed information of the communication between processors can be found in Ref. [70, 23]

Though in the timing benchmark test the force-decomposition algorithm is not the fastest parallel method [70], it is still the first choice to us because of the following advantages. (1) The force-decomposition method does not require the system to be uniform in material types or particle distributions and it works well for systems with complicated components and boundary conditions. (2) The algorithm remains efficient both for systems of a large particle number $N$ and on super-computers with a large processor number $P$. (3) Furthermore, the algorithm is relatively easy to implement and is portable for different simulations. However, the only disadvantage of the method is that it requires the processor number $P$ be an even power of 2 (which can be further relaxed to a power of 2), which may cause problems when computational resources are limited.

## *2.2 The interaction potential of various materials*

In the molecular dynamics simulations of nanoscale liquid structures, several materials are involved, including propane, nitrogen, and face centered cubic (FCC) metals. Among them, propane is in its liquid and gas state, used as the components of nanobridges and nanojets; nitrogen is in its gas state and is used as the gaseous environment surrounding the nanobridges or nanojets; and the FCC metals are in the crystal state and are used to make nozzles to generate nanojets. Since they are in different phases and have different types of interactions, the simulation of each material, especially the description of its interaction potential, is quite different from

each other and will be discussed separately in this section.

### 2.2.1 Propane – the component of nanoscale liquid structures

Propane is a common fuel for barbecues and cigarette lighters. It is also the main component of the liquefied petroleum gas (LPG). Normally propane is an odorless and colorless gas under the common conditions and is often stored as liquid under high pressure at room temperature. The melting point of propane is 85 K and the boiling point is 230 K. The density of bulk liquid propane is between 0.58 - 0.7$\times 10^3$ kg/m$^3$ under 1 atm.

Chemically, propane is a three-carbon alkane (see Fig. 1). Its chemical formula is $C_3H_8$ or $CH_3$-$CH_2$-$CH_3$ and its molecular mass is 44.1 amu (atomic mass unit). The shape of a propane molecule is displayed in Fig. 1(a). Basically, it is a non-polar molecule with a small dipole moment of 0.084 D [14]. In its ground state, the length of the carbon-carbon (C-C) bond is 0.154 nm [53] (see Fig. 1(b)). The three carbon atoms in the molecule are not in a straight line but form an angle of 112.4° [55] (see Fig. 1(b)). Near the equilibrium positions, the stretching force constant of the C-C single bond is 450 J/m$^2$ [14].

In our molecular dynamics simulations, the propane molecule is modeled as three units (points) connected with rigid springs, as displayed in Fig. 1(c), with each (unit) point representing a $CH_n$ ($n = 2, 3$) group. This model is called the "united-atom" model and was first used by Ryckaert and Bellemans [35] in the simulation of liquid butane. Now, it has been extended to the simulation of n-alkanes [32, 7, 53, 30]. In this model, each unit is considered as a mass point having the entire mass of the $CH_n$ group. The units interact with each other by means of bonded and non-bonded forces. The forces between the units in different molecules are non-bonded forces, which are described by a Lennard-Jones 12-6 potential as,

$$U_{\alpha\beta}^{LJ}(r) = 4\epsilon_{\alpha\beta}\left[\left(\frac{\sigma_{\alpha\beta}}{r}\right)^{12} - \left(\frac{\sigma_{\alpha\beta}}{r}\right)^{6}\right], \tag{2.17}$$

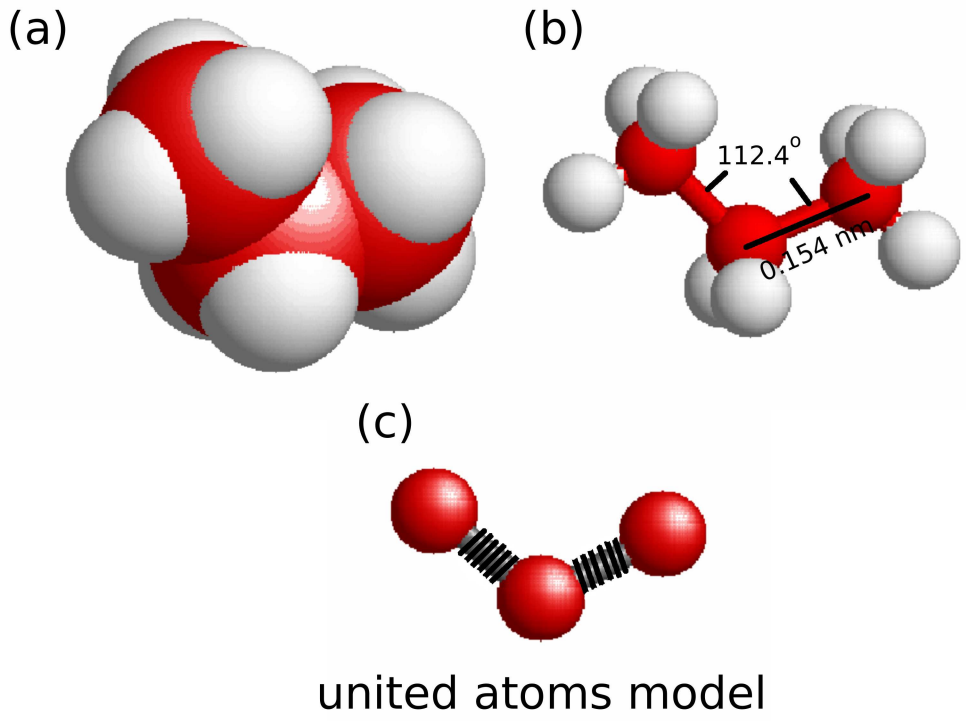


**Figure 1:** Propane molecule and the united-atom model. (a) The geometrical shape of a propane molecule; (b) The bond length of C-C bond and the bond angle formed by the three carbon atoms; (c) The united-atom model of a propane molecule, where units are connected with rigid springs.

where $\alpha$ and $\beta$ represent $CH_2$ or $CH_3$ segments in different molecules, $\epsilon_{\alpha\beta}$ is the potential depth, and $\sigma_{\alpha\beta}$ is the radius of the repulsive core. The parameters of the Lennard-Jones potential adopted in the simulations are listed in Table 1 [89], where the interaction parameters between units $CH_2$ and $CH_3$ are obtained by Lorentz-Berthelot mixing rules [56].

The forces inside a propane molecule are bonded forces, which are modeled as stretching forces and bending forces. The stretching forces are caused by the length changes of the C-C bonds. Since the length change of the C-C bond is small, the stretching of the bond is well approximated using the harmonic potential,

$$U^s(l) = \frac{1}{2} k_s \left(l - l_b\right)^2, \tag{2.18}$$

**Table 1:** Parameters of Lennard-Jones potential between atom units of different propane molecules.

| Units involved | $\epsilon$ (kJ/mol) | $\sigma$ (nm) |
|---|---|---|
| $CH_2$ - $CH_2$ | 0.496 | 0.3905 |
| $CH_3$ - $CH_3$ | 0.735 | 0.3905 |
| $CH_2$ - $CH_3$ | 0.604 | 0.3905 |

where $l$ is the instantaneous length of the C-C bond, $l_b$ is the length of the C-C bond at equilibrium, and $k_s$ is the force constant of the harmonic potential. In our model, $l_b$ takes the experimental value of 0.154 nm; however, the force constant $k_s$ has a value of 100 J/m$^2$, which is much smaller than the experimental value of 450 J/m$^2$ [68, 14]. The reduction of $k_s$ enables us to use a time step as large as 5 fs in the simulations, saving a lot of simulation time. Note that we are not interested in the high frequency oscillations in the propane molecules and reducing the strength of the force constant does not change the main results of our simulations.

The bending force is produced by the variation of the bond angle formed by the three carbon atoms in a propane molecule, and a potential function is used to describe the bending interaction. Near the equilibrium bond angle, the potential function is well approximated by the following harmonic function,

$$U^b(\theta) = \frac{1}{2} k_b \left(\theta - \theta_0\right)^2 , \tag{2.19}$$

where $\theta$ is the instantaneous bond angle, $\theta_0$ is the equilibrium bond angle, and $k_b$ is the bending force constant. In this model, $\theta_0$ takes the experimental value of 112.4°, and $k_b$ takes the value of 520 kJ/(mol·rad) [68].

In the simulations, propane molecules are used as the constituent of nanobridges and nanojets under various conditions. Compared with Lennard-Jones fluids, such as those made of argon or krypton [72, 80], propane has a much broader temperature range for its liquid state. This remarkable property makes propane a convenient

material for molecular dynamics simulations to study and illustrate general hydrodynamical behavior of liquid.

### 2.2.2 Nitrogen gas – the surrounding gas environment

Elemental nitrogen often exists in the form of diatomic molecules. As the main component of the earth's atmosphere, nitrogen is colorless and odorless. Under the pressure of 1 atm, the boiling point of liquid nitrogen is 77 K and the melting point of solid nitrogen is 63 K. A nitrogen molecule, $N_2$, has a molecular mass of 14.0067 amu. Due to the geometrical symmetry, a nitrogen molecule is non-polar without any perceivable dipole moment. Since the two nitrogen atoms in the molecule are connected with a strong triple bond, nitrogen molecules are usually chemically inert. In equilibrium, the N≡N triple bond has a bond length of 0.110 nm [28] (see Fig. 2(a)) and a stretching force constant of 2.26 kJ/m$^2$ [60].

Compared with the modeling of propane molecules, the modeling of nitrogen molecules is relatively simpler. Each atom in the nitrogen molecule is regarded as a point mass and the two nitrogen atoms are connected with a strong spring. Similar to the propane case, the nitrogen atoms interact with each other through bonded and non-bonded forces. The only bonded force in a nitrogen molecule is the stretching force of the N≡N triple bond. It is described by a harmonic potential having the same form as Eq. (2.18), with a force constant of $k_s = 112$ J/m$^2$. The force between nitrogen atoms of different molecules is non-bonded interaction, which is captured by a Lennard-Jones 12-6 potential

$$U(r) = 4\epsilon \left[ \left(\frac{\sigma}{r}\right)^{12} - \left(\frac{\sigma}{r}\right)^{6} \right], \tag{2.20}$$

with $\epsilon = 0.365$ kJ/mol and $\sigma = 0.3341$ nm [28]. Note that in our simulations, we adopt a much smaller stretching force constant for nitrogen molecules. As in the propane cases, this has little influence on our simulation results since the high frequency vibrations of nitrogen molecules do not couple strongly with the much lower frequency

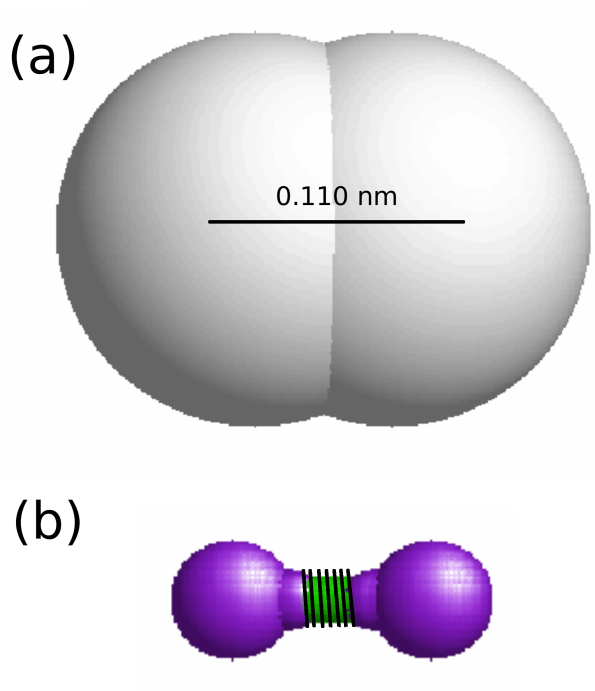


**Figure 2:** A nitrogen molecule and its model. (a) The geometrical shape of a nitrogen molecule; (b) the dumb-bell model of a nitrogen molecule. Note that in (b) two balls are connected by a spring with a force constant of 112 J/m$^2$.

degrees of freedom that are of interest to our study.

In the simulations, nitrogen molecules are used as a surrounding gas environment for liquid structures such as nanobridges and nanojets. Under the simulation conditions (150 K - 200 K), it is almost insoluble to liquid propane, which simplifies the analysis of liquid structures in a gaseous environment significantly.

### 2.2.3 Gold and platinum – constructing a nozzle

Gold (Au, atomic number 79) and platinum (Pt, atomic number 78) are both transition metals and they have many similar properties. In the periodic table, the positions of these two metals are adjacent; they both have high densities, high melting points and a face centered cubic (FCC) crystal lattice (as displayed in Fig. 3). Gold has

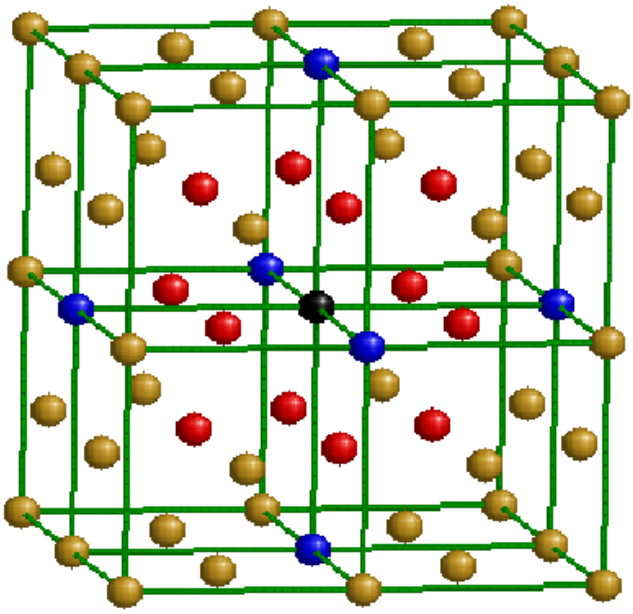

**Figure 3:** Eight conventional cells of face centered cubic lattice. The atom at the center (shown as a black ball) has 12 nearest neighbors (shown as red balls) and 6 next nearest neighbors (shown as blue balls).

an atomic mass of 196.67 amu, a lattice constant of 0.408 nm [65], a density about $19.3\times10^3$ kg/m$^3$ [14], and a melting point of 1337.33 K [14]; while platinum has an atomic mass of 195.08 amu [14], a lattice constant of 0.392 nm [65], a density about $21.45\times10^3$ kg/m$^3$ [14], and a melting point of 2041.4K [14].

Gold and platinum are modeled using a semi-empirical method. According to the density functional theory [67, 88, 71], the force acting on a metal nucleus is determined by the charge density functional surrounding the nucleus [21]. Stott and Zaremba further showed that the potential energy of an impurity in a host metal is a functional of the electron density of the host without the impurity [52], i.e.,

$$E = \mathcal{F}[\rho_{Host}(\mathbf{r}); Z, \mathbf{R}], \tag{2.21}$$

where $\rho_{Host}(\mathbf{r})$ is the charge density of the host metal without the impurity; Z and $\mathbf{R}$ are the charge and the position of the impurity. Based on these observations, Daw

and Baskes developed a semi-empirical method to study metals called the "embedded-atom method" (EAM) [57, 58]. In this method, each atom is regarded as an "impurity" of the rest of the atoms in the metal, and the total energy is the sum of each embedded energy. This idea can be expressed as,

$$E_{tot} = \sum_i F_i(\rho_{host,i}), \tag{2.22}$$

where $F_i$ is the embedding functional (embedded energy), $\rho_{host,i}$ is the charge density of the host metal without the impurity. Note that, as an average effect, Eq. (2.22) neglects the repulsive interaction between nuclei, which is not negligible on many occasions, e.g., in a metallic melt where nuclei can sometimes be very close to each other. This repulsion leads to a short-range pairwise correction to the total energy potential. The revised formula for the total energy is,

$$E_{tot} = \sum_i F_i(\rho_{host,i}) + \frac{1}{2}\sum_{\substack{i,j \\ i\neq j}} \phi_{ij}(R_{ij}), \tag{2.23}$$

where $\phi_{ij}$ is the short-range pair repulsive potential and $R_{ij}$ is the distance between the two atoms (nuclei) labeled as $i$ and $j$.

To apply the EAM potential in Eq. (2.23), the exact form of $\rho_{host,i}$, $F_i$ and $\phi_{ij}$ need to be specified. However, there is no consensus on the exact form of $\rho_{host,i}$, $F_i$ and $\phi_{ij}$. In our simulations, the gold and platinum atoms are used to build nanoscale nozzles. Since all the nozzles work at a temperature well below the melting points of both of the metals, their atoms can only move around the equilibrium positions. Therefore, for simplicity, only the nearest neighbor atoms are considered in the determination of the exact form of the EAM theory. According to the nearest-neighbor version of EAM theory developed by Johnson [37, 38], the pair repulsive interaction has a decreasing exponential form (Born-Mayer form)

$$\phi(r) = \phi_e \exp\left[-\gamma\left(\frac{r}{r_e} - 1\right)\right], \tag{2.24}$$

**Table 2:** Parameters of EAM potential for gold and platinum. $E_c$ and $\phi_e$ are in eV. $f_e$ is in arbitary unit (it only appears in ratios). $\alpha$, $\beta$, and $\gamma$ are dimensionless parameters. $r_e$ is in Å.

| Atom | $E_c$ | $f_e$ | $\phi_e$ | $\alpha$ | $\beta$ | $\gamma$ | $r_e$ |
|---|---|---|---|---|---|---|---|
| Au | 3.93 | 0.23 | 0.65 | 6.37 | 6.67 | 8.20 | 2.87 |
| Pt | 5.77 | 0.38 | 0.95 | 6.44 | 6.69 | 8.57 | 2.77 |

where $r_e$ is the equilibrium distance of an atom to its nearest neighbors, $\phi_e$ is the repulsive energy at the equilibrium distance, and $\gamma$ is a dimensionless parameter depicting the decaying effect. The charge density $\rho_{host,i}$ is the sum of the charge density contributed by the nearest neighbor atoms, which is only a function of the distance $R_{ij}$. i.e.,

$$\rho_{host,i} = \sum_{j \neq i} f_j(R_{ij}), \tag{2.25}$$

where $f_j$ is the the electron density due to atom j. The explicit form of $f$ is

$$f(r) = f_e \exp\left[-\beta\left(\frac{r}{r_e} - 1\right)\right], \tag{2.26}$$

where $f_e$ is the equilibrium value of $f$ and $\beta$ is the decay parameter. The embedding functional is,

$$F(\rho) = -E_c(1 - \ln x)x - 6\phi_e y, \tag{2.27}$$

where $x = (\rho/\rho_e)^{\alpha/\beta}$, $y = (\rho/\rho_e)^{\gamma/\beta}$, $\rho_e$ is the sum of $f_e$ at all the nearest neighbors, $E_c$ is the cohesive energy of the metal, and $\alpha = 3(\Omega B/E_c)^{1/2}$, which is a combination of the atomic volume ($\Omega$), bulk modulus ($B$) and $E_c$. Since each atom in fcc metal has 12 nearest neighbors (see Fig. 3), $\rho_e = 12\phi_e$. EAM potential parameters for gold and platinum can be found in Table 2 [38].

### 2.2.4 Interactions between different materials

The interaction between different materials is a weak interaction as long as there is no chemical reaction involved. It is often modeled through the 12-6 Lennard-Jones

**Table 3:** Parameters of Lennard-Jones potential between propane molecules and nitrogen molecules

| Interaction | $\epsilon$ (kJ/mol) | $\sigma$ (nm) |
|---|---|---|
| N - $CH_3$ | 0.516 | 0.3623 |
| N - $CH_2$ | 0.424 | 0.3623 |

potential in Eq. (2.17). In many cases, experiments (or first principle calculations) can only provide the parameters (the depth of the well $\epsilon$ and the repulsive radius $\sigma$) of the Lennard-Jones potential of the same material, whereas the parameters between different materials are usually not furnished. On this occasion, the interaction parameters can be obtained approximately using the Lorentz-Berthelot mixing rules [56] as follows. Suppose the interaction between molecules of material A and B are described by Lennard-Jones potentials, Eq. (2.17), and the potential parameters $\epsilon$ and $\sigma$ are known for each material. Then, according to the Lorentz-Berthelot mixing rules, the interaction between material A and B is still a 12-6 Lennard-Jones potential. The parameters $\sigma_{AB}$ and $\epsilon_{AB}$ for the potential are given by

$$\sigma_{AB} = \frac{1}{2}(\sigma_{AA} + \sigma_{BB}), \tag{2.28}$$

and

$$\epsilon_{AB} = \sqrt{\epsilon_{AA}\epsilon_{BB}}, \tag{2.29}$$

where, $\sigma_{AA}$ and $\epsilon_{AA}$ are Lennard-Jones potential parameters for material A, and $\sigma_{BB}$ and $\epsilon_{BB}$ are parameters for material B.

With minor corrections, the Lorentz-Berthelot mixing rules are applied to yield the parameters of the interaction between propane molecules and nitrogen molecules. Recall that in the models proposed in Subsection 2.2.1 and Subsection 2.2.2, a propane molecule is composed of three atom units and a nitrogen molecule is composed of two atoms, and the parameters of both the interaction between the units and the interaction between nitrogen atoms are available. Accordingly, the interaction between a

**Table 4:** Parameters of Lennard-Jones potential between different materials

| Interaction | $\epsilon$ (kJ/mol) | $\sigma$ (nm) |
|---|---|---|
| Au $\sim$ Au | 42.58 | 0.2637 |
| Pt $\sim$ Pt | 65.74 | 0.2542 |
| Au $\sim$ $CH_3$ | 1.802 | 0.328 |
| Au $\sim$ $CH_2$ | 1.802 | 0.328 |
| Pt $\sim$ $CH_3$ | 1.300 | 0.3231 |
| Pt $\sim$ $CH_2$ | 1.300 | 0.3231 |

propane molecule and a nitrogen molecule is depicted as interactions between nitrogen atoms and atom units of propane molecules. Their parameters, listed in Table 3, are obtained by the mixing rules.

The interaction between propane molecules and metals can also be described by Lennard-Jones potentials, however the parameters are determined through the combination of experiments and the mixing rules. Note that the interaction between metal atoms is described by the EAM potential in our simulations, the mixing rules can not be applied directly. To employ the mixing rules, first we suppose the interaction between metal atoms has an effective Lennard-Jones potential form and the parameters of the effective potential are obtained by experiments [82] (see Table 4 for the parameters for gold and platinum). Then, the repulsive radius ($\sigma$) of the interaction between a propane molecule and a metal atom is calculated using Eq. (2.28). The other parameter, the depth of the well ($\epsilon$) of the Lennard-Jones potential, is obtained through direct molecular dynamics simulations to yield the experimentally measured value of the adsoption energy of propane on the metal surface. The parameters of the interaction between propane molecules and gold atoms (see Table 4) first appeared in Ref. [83]; and the parameters of the interaction between propane molecules and platinum atoms (see Table 4) were first employed in Ref. [12].

# CHAPTER III

# MICROSCOPIC HYDRODYNAMICS AND RELATED THEORETICAL ISSUES

## *3.1 Lubrication equations (LE) and stochastic lubrication equations (SLE)*

In principle, the dynamics of free-surface flows is governed by the general Navier-Stokes equations [48]; however, quite different from the dynamics of bulk flows, to predict the dynamics of free-surface flows [17, 62] is not a trivial task because the motion of the free surface plays an active role in the dynamics of the flow. That is, the surface not only confines the volume of the flow but also, in many cases, the geometrical shape of the surface provides a driving force to the motion of the flow through the contracting force of surface tension, which is proportional to the average curvature of the surface. Therefore, to predict the dynamics of free-surface flows, the motion of the surface should also be included in the dynamical equations along with the general equations of motion.

For flows with axial symmetry, the form of dynamical equations convenient for further theoretical analysis appeared in the 1990s [78, 29, 19], based on the "lubrication approximation" idea. Starting from the general Navier-Stokes equations, a set of one-dimensional dynamical equations were obtained by several groups independently [78, 29, 19]. Since the equations originated from the "lubrication approximations", they were called "lubrication equations" (LE) by some authors [55], while in other work, they were also known as "Cosserat equations" [17]. The lubrication equations capture many interesting physics of free-surface flows with axial symmetry, such as the instability of the flow [90], the distribution of the drop size after the flow breaks

up [62, 50], and even the finite-time singular property near the breakup. It also shows that near the breakup the solution of the equations for a liquid filament is self-similar [29] and independent of the circumstance, i.e., initial conditions and boundary conditions. Remarkably, most of the theoretical predictions based on lubrication equations were confirmed by a series of experiments [45]. The success of lubrication equations shows that the dynamics of free-surface flows with axial symmetry is essentially one-dimensional with strong non-linearity.

The dynamical equations which include the influence of thermal fluctuations for a flow with axial symmetry were first obtained by Moseler and Landman in the year 2000 [55] to account for the difference between the pinching dynamics of nanojets and that of deterministic macroscopic liquid jets. They started from the general theory of fluctuations in fluid dynamics [48] and employed a "lubrication" method similar to that used in the derivation of the lubrication equations to deal with the fluctuations of the stress tensor in the general theory of hydrodynamics with thermal fluctuations [48]. The equations thus obtained were called "stochastic lubrication equations" (SLE). Similar to the lubrication equations, the stochastic lubrication equations are one-dimensional and they are convenient for further theoretical and numerical analysis. Equipped with the newly devised stochastic lubrication equations, they illustrated that at the nanoscale, the influence of thermal fluctuations emerged because of the confinement of the free surface of the flow at the nanoscale. The combination of thermal fluctuations and the confinement of the surface altered the pinching dynamics of nanojets fundamentally. These results have been confirmed and generalized by further theoretical analysis (see [18, 92] and discussions in the present thesis for details). Nevertheless, the study of the motion of nanoscale free-surface flows based on the stochastic lubrication equations is still in its primitive stage. With the stochastic term, which represents the influence of thermal fluctuations, in the stochastic lubrication equations, the solution to the equations is no longer

of a deterministic nature. Instead, probability concepts have to be adopted and consequently, new methods and tools have to be developed to extract meaningful results from the equations.

### 3.1.1 The derivation of lubrication equations

There are several parallel approaches which can lead to the lubrication equations [17]. Here, we adopt the averaging approach [17] first devised by Dupont because it is easy to be generalized to include the thermal fluctuations. In this approach, the Navier-Stokes equations are projected onto a set of basis functions, and the equations of the projecting coefficients with respect to the basis functions are obtained as the approximate equations of motion.

Suppose the flow is axisymmetric and incompressible, its velocity field can be expressed as a unique sum of some basis functions as,

$$\mathbf{v}(r,z,t) = v_r\mathbf{e_r} + v_z\mathbf{e_z} = \sum_{i=0}^{\infty}\int_{-\infty}^{\infty} d\bar{z}v^{(2i)}(\bar{z},t)\mathbf{w}^{(2i,\bar{z})}(r,z), \tag{3.1}$$

with divergence-free bases

$$\mathbf{w}^{(2i,\bar{z})}(r,z) = -\frac{r^{2i+1}}{2i+2}\delta'(z-\bar{z})\mathbf{e_r} + r^{2i}\delta(z-\bar{z})\mathbf{e_z}, \tag{3.2}$$

where $v^{(2i)}(\bar{z},t)$ are the coefficients of the basis functions and can be projected out by the following inverse transform,

$$v^{(2i)}(\bar{z},t) = \int_{\Omega} dV\,\mathbf{v}(r,z,t)\cdot\mathbf{w}^{(2i,\bar{z})}(r,z). \tag{3.3}$$

Here, $dV$ is the volume element and $\Omega$ is the entire volume of the flow. Note that the "$'$" in Eq. (3.2) refers to the derivative with respect to the variable $z$. Including the pressure as part of a stress tensor (in component form),

$$\sigma_{ij} = -p\delta_{ij} + 2\eta D_{ij}(\mathbf{v}), \tag{3.4}$$

the Navier-Stokes equations can be expressed as,

$$\rho\left(\frac{\partial\mathbf{v}}{\partial t} + \mathbf{v}\cdot\nabla\mathbf{v}\right) = \nabla\cdot\sigma, \tag{3.5}$$

where, for incompressible fluids, $D_{ij}$ is defined as (in component form)

$$D_{ij} = \frac{1}{2}\left(\frac{\partial v_j}{\partial x_i} + \frac{\partial v_i}{\partial x_j}\right). \tag{3.6}$$

Symbolically, the projection of the Navier-Stokes equations on the bases $\mathbf{w}^{(2i,\bar{z})}(r,z)$ can be written as,

$$\rho I_\rho^{(2i,\bar{z})} = I_\sigma^{(2i,\bar{z})}, \tag{3.7}$$

with

$$I_\rho^{(2i,\bar{z})} = \int_\Omega dV \left(\frac{\partial \mathbf{v}}{\partial t} + \mathbf{v}\cdot\nabla\mathbf{v}\right)\cdot\mathbf{w}^{(2i,\bar{z})}, \tag{3.8}$$

and

$$I_\sigma^{(2i,\bar{z})} = \int_\Omega dV(\nabla\cdot\sigma)\cdot\mathbf{w}^{(2i,\bar{z})}. \tag{3.9}$$

The integral $I_\sigma^{(2i,\bar{z})}$ can be further expressed as two terms through integrating by parts as,

$$I_\sigma^{(2i,\bar{z})} = \int_\Omega dV(\nabla\cdot\sigma)\cdot\mathbf{w}^{(2i,\bar{z})} = -\gamma I_\gamma^{(2i,\bar{z})} - 2\eta I_\eta^{(2i,\bar{z})}, \tag{3.10}$$

where, $\gamma$ is the surface tension of the liquid, $\eta$ is the viscosity of the flow,

$$\begin{aligned} -\gamma I_\gamma^{(2i,\bar{z})} &= \int_\Omega dV \nabla\cdot\left[\sigma\cdot\mathbf{w}^{(2i,\bar{z})}\right] \\ &= \int_{\partial\Omega} dS\mathbf{n}\cdot\sigma\cdot\mathbf{w}^{(2i,\bar{z})} \\ &= -\gamma\int_{\partial\Omega} dS\kappa\mathbf{n}\cdot\mathbf{w}^{(2i,\bar{z})}, \end{aligned} \tag{3.11}$$

and

$$\begin{aligned} 2\eta I_\eta^{(2i,\bar{z})} &= \int_\Omega dV\sigma_{jk}\frac{\partial w_k^{(2i,\bar{z})}}{\partial x_j} \\ &= \int_\Omega dV(-p\delta_{jk} + 2\eta D_{jk})\frac{\partial w_k^{(2i,\bar{z})}}{\partial x_j} \\ &= 2\eta\int_\Omega dV D_{jk}\frac{\partial w_k^{(2i,\bar{z})}}{\partial x_j}. \end{aligned} \tag{3.12}$$

In the above equations $\partial\Omega$ is the surface of the flow, $dS$ is the surface element, $\mathbf{n}$ is the unit normal vector on the surface, and $\kappa$ is the average curvature on the flow

surface. Note that in the derivation of Eq. (3.11), we use the Young-Laplace equation (in the component form) [48, 62],

$$\sigma_{ij} n_j = -\gamma \kappa n_i, \tag{3.13}$$

to calculate the internal pressure of the flow balanced by the surface tension of the liquid surface. Also in the derivation of Eq. (3.12), the divergence-free property of $\mathbf{w}^{(2i,\bar{z})}$ is employed. Since $D_{ij}$ defined in Eq. (3.6) is symmetric, i.e. $D_{ij} = D_{ji}$, the integral $I_\eta^{(2i,\bar{z})}$ can be written in a symmetric form as follows.

$$\begin{aligned} I_\eta^{(2i,\bar{z})} &= \int_\Omega dV D_{jk} \frac{\partial w_k^{(2i,\bar{z})}}{\partial x_j} \\ &= \int_\Omega dV \frac{1}{2} \left( D_{jk} \frac{\partial w_j^{(2i,\bar{z})}}{\partial x_k} + D_{kj} \frac{\partial w_k^{(2i,\bar{z})}}{\partial x_j} \right) \\ &= \int_\Omega dV D_{jk} \frac{1}{2} \left( \frac{\partial w_j^{(2i,\bar{z})}}{\partial x_k} + \frac{\partial w_k^{(2i,\bar{z})}}{\partial x_j} \right) \\ &= \int_\Omega dV D_{jk}(\mathbf{v}) D_{jk}(\mathbf{w}^{(2i,\bar{z})}). \end{aligned} \tag{3.14}$$

In order to obtain the lubrication equations, we explicitly calculate the above projections onto the lowest order basis $\mathbf{w}^{(0,\bar{z})}$. In cylindrical coordinates,

$$\mathbf{w}^{(0,\bar{z})} = -\frac{r}{2} \delta'(z - \bar{z}) \mathbf{e_r} + \delta(z - \bar{z}) \mathbf{e_z}; \tag{3.15}$$

$$\begin{aligned} D_{rr}(\mathbf{v}) &= \frac{\partial v_r}{\partial r}, \\ D_{\phi\phi}(\mathbf{v}) &= \frac{v_r}{r}, \\ D_{zz}(\mathbf{v}) &= \frac{\partial v_z}{\partial z}, \\ D_{zr}(\mathbf{v}) &= D_{rz}(\mathbf{v}) = \frac{1}{2} \left( \frac{\partial v_z}{\partial r} + \frac{\partial v_r}{\partial z} \right); \end{aligned} \tag{3.16}$$

and

$$\mathbf{v} \cdot \nabla \mathbf{v} = (v_r \frac{\partial v_r}{\partial r} + v_z \frac{\partial v_r}{\partial z}) \mathbf{e_r} + (v_r \frac{\partial v_z}{\partial r} + v_z \frac{\partial v_z}{\partial z}) \mathbf{e_z}; \tag{3.17}$$

where, axial symmetry of the velocity field is assumed. To the lowest order, $\mathbf{v}$ itself can be approximated using the basis $\mathbf{w}^{(0,\bar{z})}$ and its corresponding coefficient $v_0(\bar{z}, t)$

as,

$$\begin{aligned}
\mathbf{v}(r,z,t) &\approx \int_{-\infty}^{\infty} d\bar{z} v_0(\bar{z},t)\mathbf{w}^{(0,\bar{z})} \\
&\approx \int_{-\infty}^{\infty} d\bar{z} v_0(\bar{z},t)\left[-\frac{r}{2}\delta'(z-\bar{z})\mathbf{e_r}+\delta(z-\bar{z})\mathbf{e_z}\right] \\
&\approx -\frac{r}{2}v_0'(z,t)\mathbf{e_r}+v_0(z,t)\mathbf{e_z} \qquad (3.18)
\end{aligned}$$

and the corresponding $I_\rho^{(0,\bar{z})}$, $I_\gamma^{(0,\bar{z})}$, and $I_\eta^{(0,\bar{z})}$ can be calculated as follows:

$$\begin{aligned}
I_\rho^{(0,\bar{z})} &= \int_\Omega dV\left(\frac{\partial \mathbf{v}}{\partial t}+\mathbf{v}\cdot\nabla\mathbf{v}\right)\cdot\mathbf{w}^{(0,\bar{z})} \\
&= \int_\Omega dV\left[\left(\frac{\partial v_r}{\partial t}+v_r\frac{\partial v_r}{\partial r}+v_z\frac{\partial v_r}{\partial z}\right)w_r^{(0,\bar{z})}+\left(\frac{\partial v_z}{\partial t}+v_r\frac{\partial v_z}{\partial r}+v_z\frac{\partial v_z}{\partial z}\right)w_z^{(0,\bar{z})}\right] \\
&= \int_\Omega dV\left[-\frac{r}{2}\frac{\partial v_0'}{\partial t}-\frac{rv_0'}{2}\frac{\partial}{\partial r}\left(-\frac{rv_0'}{2}\right)+v_0\frac{\partial}{\partial z}\left(-\frac{rv_0'}{2}\right)\right]\left(-\frac{r}{2}\right)\delta'(z-\bar{z}) \\
&\quad +\int_\Omega dV\left[\frac{\partial v_0}{\partial t}-\frac{rv_0'}{2}\frac{\partial v_0}{\partial r}+v_0\frac{\partial v_0}{\partial z}\right]\delta(z-\bar{z}) \\
&= \int_0^{2\pi}d\theta\int_{-\infty}^{\infty}dz\int_0^{h(\bar{z})}rdr\left[\frac{r^2\dot{v}_0'}{4}-\frac{r^2(v_0')^2}{8}+\frac{r^2v_0v_0''}{4}\right]\delta'(z-\bar{z}) \\
&\quad +\int_0^{2\pi}d\theta\int_{-\infty}^{\infty}dz\int_0^{h(\bar{z})}rdr\left[\dot{v}_0+v_0v_0'\right]\delta(z-\bar{z}) \\
&= 2\pi\int_{-\infty}^{\infty}dz\left\{\left[\dot{v}_0'-\frac{(v_0')^2}{2}+v_0v_0''\right]\frac{h^4\delta'(z-\bar{z})}{16}+(\dot{v}_0+v_0v_0')\frac{h^2\delta(z-\bar{z})}{2}\right\} \\
&= \pi h^2(\dot{v}_0+v_0v_0')-\frac{\pi h^4}{8}\left[\dot{v}_0'+v_0v_0''-\frac{(v_0')^2}{2}\right]', \qquad (3.19)
\end{aligned}$$

where $h(\bar{z})$ is the height of the surface at $\bar{z}$ and " $\dot{}$ " refers to the partial derivative with respect to the time $t$. Note that in the last step of the above equation, the meaning of " $'$ " is changed from the partial derivative with respect to the variable $z$ to the partial derivative with respect to the variable $\bar{z}$ according to the integration

rules of delta function.

$$
\begin{aligned}
I_{\eta}^{(0,\bar{z})} &= \int_{\Omega} dV D_{ij}(\mathbf{v}) D_{ij}(\mathbf{w}^{(0,\bar{z})}) \\
&= \int_{\Omega} dV \left[ D_{rr}(\mathbf{v}) D_{rr}(\mathbf{w}^{(0,\bar{z})}) + D_{\phi\phi}(\mathbf{v}) D_{\phi\phi}(\mathbf{w}^{(0,\bar{z})}) + D_{zz}(\mathbf{v}) D_{zz}(\mathbf{w}^{(0,\bar{z})}) \right] \\
&\quad + \int_{\Omega} dV \left[ 2 D_{rz}(\mathbf{v}) D_{rz}(\mathbf{w}^{(0,\bar{z})}) \right] \\
&= \int_{\Omega} dV \left[ \frac{\partial v_r}{\partial r} \frac{\partial w_r^{(0,\bar{z})}}{\partial r} + \frac{v_r w_r^{(0,\bar{z})}}{r^2} + \frac{\partial v_z}{\partial z} \frac{\partial w_z^{(0,\bar{z})}}{\partial z} \right] \\
&\quad + \int_{\Omega} dV \left[ \frac{1}{2} \left( \frac{\partial v_z}{\partial r} + \frac{\partial v_r}{\partial z} \right) \left( \frac{\partial w_z^{(0,\bar{z})}}{\partial r} + \frac{\partial w_r^{(0,\bar{z})}}{\partial z} \right) \right] \\
&= 2\pi \int_{-\infty}^{\infty} dz \int_0^{h(\bar{z})} r dr \left[ \left( \frac{v_0'}{4} + \frac{v_0'}{4} + v_0' \right) \delta'(z - \bar{z}) + \frac{r^2}{8} v_0'' \delta''(z - \bar{z}) \right] \\
&= -\frac{3\pi}{2} \left( h^2 v_0' \right)' + \frac{\pi}{16} \left( h^4 v_0'' \right)'' . \qquad (3.20)
\end{aligned}
$$

$$
\begin{aligned}
I_{\gamma}^{(0,\bar{z})} &= \int_{\partial\Omega} dS \kappa \mathbf{n} \cdot \mathbf{w}^{(0,\bar{z})} = \int_{\Omega} dV \nabla \cdot \left( \kappa \mathbf{w}^{(0,\bar{z})} \right) \\
&= \int_{\Omega} dV \left[ \nabla \kappa \cdot \mathbf{w}^{(0,\bar{z})} + \kappa \nabla \cdot \mathbf{w}^{(0,\bar{z})} \right] = \int_{\Omega} dV \nabla \kappa \cdot \mathbf{w}^{(0,\bar{z})} \\
&= 2\pi \int_{\infty}^{\infty} dz \int_0^{h(\bar{z})} r dr \frac{\partial \kappa}{\partial z} w_z^{(0,\bar{z})} \\
&= 2\pi \int_{\infty}^{\infty} dz \int_0^{h(\bar{z})} r dr \kappa' \delta(z - \bar{z}) \\
&= \pi h^2 \kappa', \qquad (3.21)
\end{aligned}
$$

where the mean curvature

$$
\kappa = \frac{1}{h(1 + h'^2)^{1/2}} - \frac{h''}{(1 + h'^2)^{3/2}}, \qquad (3.22)
$$

is just a function of $h(\bar{z})$ and its derivatives. Now, the projection of Navier-Stokes equations yields

$$
\begin{aligned}
\rho\pi h^2 (\dot{v}_0 + v_0 v_0') &- \rho \frac{\pi}{8} \left\{ h^4 \left[ \dot{v}_0' + v_0 v_0'' - \frac{(v_0')^2}{2} \right] \right\}' = \\
&-\gamma \pi h^2 \kappa' - 2\eta \left[ -\frac{3\pi}{2} \left( h^2 v_0' \right)' + \frac{\pi}{16} \left( h^4 v_0'' \right)'' \right] . \qquad (3.23)
\end{aligned}
$$

To keep in line with the common meaning of variables, we replace the variable $\bar{z}$ in Eq. (3.23) with variable $z$ and keep the form of the equation intact. When both sides of Eq. (3.23) are expanded to the second power of $h$, we obtain that

$$\rho\left(\dot{v}_0 + v_0 v_0'\right) = -\gamma\kappa' + \frac{3\eta(h^2 v_0')'}{h^2}, \tag{3.24}$$

which is the velocity equation of the lubrication equations.

Plugging Eq. (3.18) into the kinematic boundary condition

$$\frac{\partial h}{\partial t} + v_z \frac{\partial h}{\partial z} = v_r|_{r=h}, \tag{3.25}$$

we obtain the other equation of the lubrication equations, i.e.,

$$\frac{\partial h}{\partial t} + v_0 \frac{\partial h}{\partial z} = -\frac{h v_0'}{2}, \tag{3.26}$$

where, the kinematic boundary condition implies that no fluid can cross the free surface. Note that to account for the strong non-linearity near the breakup of the flow, the full form of the mean curvature $\kappa$, as displayed in Eq. (3.22), is used without further approximation.

### 3.1.2 The derivation of stochastic lubrication equations

The stochastic lubrication equations were first obtained by Moseler and Landman in the year 2000 [54, 55]. Here, we derive the equations following their approach.

Without heat transfer, the general hydrodynamic formula with thermal fluctuations for an incompressible flow [48] is

$$\rho\left(\frac{\partial \mathbf{v}}{\partial t} + \mathbf{v}\cdot\nabla\mathbf{v}\right) = \nabla\cdot\sigma, \tag{3.27}$$

where $\sigma$ has a slightly different definition as that in the Navier-Stokes equations as,

$$\sigma_{ij} = -p\delta_{ij} + 2\eta D_{ij}(\mathbf{v}) + s_{ij}. \tag{3.28}$$

The $\mathbb{S}$ here is the fluctuations of the stress tensor $\sigma$. Its distribution is often assumed to be Gaussian and the correlations of $\mathbb{S}$ [48] are

$$\langle s_{jk}(\mathbf{r}_1, t_1), s_{lm}(\mathbf{r}_2, t_2)\rangle = \\ 2k_B T\eta \left(\delta_{jl}\delta_{km} + \delta_{jm}\delta_{kl} - \frac{2}{3}\delta_{jk}\delta_{lm}\right)\delta(\mathbf{r_1} - \mathbf{r_2})\delta(t_1 - t_2). \tag{3.29}$$

where, $k_B$ is the Boltzmann constant, $T$ is the temperature of the flow. For convenience, in the rest of this subsection, the abbreviated form $s_{ij}$ for $s_{ij}(\mathbf{r}_1, t_1)$ and $s'_{ij}$ for $s_{ij}(\mathbf{r}_2, t_2)$ will be used. In Cartesian coordinates, it is easy to verify that the correlations between components of $\mathbb{S}$ have the following symmetries.

$$\langle s_{ij}, s'_{kl}\rangle = \left\langle s'_{ij}, s_{kl}\right\rangle, \tag{3.30}$$

$$\langle s_{11}, s'_{11}\rangle = \langle s_{22}, s'_{22}\rangle = \langle s_{33}, s'_{33}\rangle, \tag{3.31}$$

$$\langle s_{11}, s'_{22}\rangle = \langle s_{11}, s'_{33}\rangle = \langle s_{22}, s'_{33}\rangle, \tag{3.32}$$

and

$$\langle s_{31}, s'_{31}\rangle = \langle s_{32}, s'_{32}\rangle. \tag{3.33}$$

Now, project Eq. (3.29) onto the basis $\mathbf{w}^{(2i,\bar{z})}$ introduced in Eq. (3.2). The projected equation can be symbolically written as,

$$\rho I_\rho^{(2i,\bar{z})} = -\gamma I_\gamma^{(2i,\bar{z})} - 2\eta I_\eta^{(2i,\bar{z})} - I_s^{(2i,\bar{z})}, \tag{3.34}$$

where, $I_\rho^{(2i,\bar{z})}$, $I_\gamma^{(2i,\bar{z})}$, and $I_\eta^{(2i,\bar{z})}$ have the same definitions as in the derivation of lubrication equations. $I_s^{(2i,\bar{z})}$ is defined in the component form as

$$I_s^{(2i,\bar{z})} = \int_\Omega dV \left(s_{jk}\frac{\partial w_k^{(2i,\bar{z})}}{\partial x_j}\right). \tag{3.35}$$

It is the result of the integral transformation of

$$\int_\Omega dV \frac{\partial s_{jk}}{\partial x_j} w_k^{(2i,\bar{z})} = \int_\Omega dV \frac{\partial}{\partial x_j}\left(s_{jk} w_k^{(2i,\bar{z})}\right) - I_s^{(2i,\bar{z})}, \tag{3.36}$$

where the first term on the right hand side of the equation has been absorbed into $I_\gamma^{(2i,\bar{z})}$. Unlike the calculation of $I_\rho^{(2i,\bar{z})}$, $I_\gamma^{(2i,\bar{z})}$, and $I_\eta^{(2i,\bar{z})}$ which are performed in cylindrical coordinates, it is more convenient to calculate $I_s^{(2i,\bar{z})}$ in Cartesian coordinates. Since $I_\rho^{(2i,\bar{z})}$, $I_\gamma^{(2i,\bar{z})}$, and $I_\eta^{(2i,\bar{z})}$ have been computed in the previous subsection, now, in order to obtain the stochastic lubrication equations, only $I_s^{(0,\bar{z})}$ still need to be calculated.

In Cartesian coordinates, $\mathbf{w}^{(0,\bar{z})}$ is written as

$$\begin{aligned}\mathbf{w}^{(0,\bar{z})} &= -\frac{r}{2}\delta'(z-\bar{z})\mathbf{e_r} + \delta(z-\bar{z})\mathbf{e_z} \\ &= -\frac{x}{2}\delta'(z-\bar{z})\hat{\mathbf{x}} - \frac{y}{2}\delta'(z-\bar{z})\hat{\mathbf{y}} + \delta(z-\bar{z})\hat{\mathbf{z}}. \end{aligned} \tag{3.37}$$

Equipped with the above expression of $\mathbf{w}^{(0,\bar{z})}$, $I_s^{(0,\bar{z})}$ is calculated as,

$$\begin{aligned} I_s^{(0,\bar{z})} &= \int_\Omega dV \left( s_{jk}\frac{\partial w_k^{(0,\bar{z})}}{\partial x_j} \right) \\ &= \int_\Omega dV \left( s_{11}\frac{\partial w_x^{(0,\bar{z})}}{\partial x} + s_{12}\frac{\partial w_y^{(0,\bar{z})}}{\partial x} + s_{13}\frac{\partial w_z^{(0,\bar{z})}}{\partial x} + s_{21}\frac{\partial w_x^{(0,\bar{z})}}{\partial y} + s_{22}\frac{\partial w_y^{(0,\bar{z})}}{\partial y} \right. \\ &\left. + s_{23}\frac{\partial w_z^{(0,\bar{z})}}{\partial y} + s_{31}\frac{\partial w_x^{(0,\bar{z})}}{\partial z} + s_{32}\frac{\partial w_y^{(0,\bar{z})}}{\partial z} + s_{33}\frac{\partial w_z^{(0,\bar{z})}}{\partial z} \right) \\ &= \int_\Omega dV \left( s_{11}\frac{\partial w_x^{(0,\bar{z})}}{\partial x} + s_{31}\frac{\partial w_x^{(0,\bar{z})}}{\partial z} + s_{22}\frac{\partial w_y^{(0,\bar{z})}}{\partial y} + s_{32}\frac{\partial w_y^{(0,\bar{z})}}{\partial z} + s_{33}\frac{\partial w_z^{(0,\bar{z})}}{\partial z} \right) \\ &= \int_\Omega dV \left[ \left( \frac{-s_{11}-s_{22}}{2} + s_{33} \right) \delta'(z-\bar{z}) - \left( \frac{s_{31}}{2}x + \frac{s_{32}}{2}y \right) \delta''(z-\bar{z}) \right] \\ &= \int dx \int dy \int_{-\infty}^{\infty} dz \left[ \left( \frac{s_{11}}{2} + s_{33} \right) \delta'(z-\bar{z}) - \left( \frac{s_{31}}{2}x + \frac{s_{32}}{2}y \right) \delta''(z-\bar{z}) \right] \\ &= \frac{\partial}{\partial \bar{z}} \int dx \int dy \left( \frac{s_{11}+s_{22}}{2} - s_{33} \right) - \frac{\partial^2}{\partial \bar{z}^2} \int dx \int dy \left( \frac{s_{31}x + s_{32}y}{2} \right), \end{aligned} \tag{3.38}$$

or in an abbreviated form,

$$I_s^{(0,\bar{z})} = \frac{\partial N}{\partial \bar{z}} + \frac{\partial^2 M}{\partial \bar{z}^2}, \tag{3.39}$$

with

$$N(\bar{z},t) = \int dx \int dy \left( \frac{s_{11}+s_{22}}{2} - s_{33} \right), \tag{3.40}$$

and

$$M(\bar{z},t) = -\int dx \int dy \left(\frac{s_{31}x + s_{32}y}{2}\right). \tag{3.41}$$

Note that $M$ and $N$ are still fluctuations of Gaussian distribution in one dimension.

Since the correlation $\left\langle \frac{s_{11}+s_{22}}{2} - s_{33}, \frac{s'_{11}+s'_{22}}{2} - s'_{33} \right\rangle$ can be simplified using the symmetries indicated in Eq. (3.30), Eq. (3.31), and Eq. (3.32) as,

$$\begin{aligned}
&\left\langle \frac{s_{11}+s_{22}}{2} - s_{33}, \frac{s'_{11}+s'_{22}}{2} - s'_{33} \right\rangle \\
&\quad = \frac{1}{4}\left(\langle s_{11}, s'_{11}\rangle + \langle s_{22}, s'_{11}\rangle + \langle s_{11}, s'_{22}\rangle + \langle s_{22}, s'_{22}\rangle\right) \\
&\quad - \frac{1}{2}\left(\langle s_{11}, s'_{33}\rangle + \langle s_{22}, s'_{33}\rangle + \langle s_{33}, s'_{11}\rangle + \langle s_{33}, s'_{22}\rangle\right) + \langle s_{33}, s'_{33}\rangle \\
&\quad = \frac{3}{2}\left(\langle s_{11}, s'_{11}\rangle - \langle s_{11}, s'_{22}\rangle\right) \\
&\quad = \frac{3}{2}\left[\frac{8}{3}k_B T\eta\delta(x_1-x_2)\delta(y_1-y_2)\delta(z_1-z_2)\delta(t_1-t_2)\right. \\
&\quad \left. + \frac{4}{3}k_B T\eta\delta(x_1-x_2)\delta(y_1-y_2)\delta(z_1-z_2)\delta(t_1-t_2)\right] \\
&\quad = 6k_B T\eta\delta(x_1-x_2)\delta(y_1-y_2)\delta(z_1-z_2)\delta(t_1-t_2),
\end{aligned} \tag{3.42}$$

the correlation of $\langle N(z_1,t_1), N(z_2,t_2)\rangle$ is calculated as

$$\begin{aligned}
&\langle N(z_1,t_1), N(z_2,t_2)\rangle \\
&\quad = \iint dx_1 dy_1 \iint dx_2 dy_2 \left\langle \frac{s_{11}+s_{22}}{2} - s_{33}, \frac{s'_{11}+s'_{22}}{2} - s'_{33} \right\rangle \\
&\quad = \iint dx_1 dy_1 \iint dx_2 dy_2 6k_B T\eta\delta(x_1-x_2)\delta(y_1-y_2)\delta(z_1-z_2)\delta(t_1-t_2) \\
&\quad = 6k_B T\eta\delta(z_1-z_2)\delta(t_1-t_2) \iint dx_1 dy_1 \iint dx_2 dy_2 \delta(x_1-x_2)\delta(y_1-y_2) \\
&\quad = 6k_B T\eta\delta(z_1-z_2)\delta(t_1-t_2) \iint dx_1 dy_1 \\
&\quad = 6k_B T\eta\delta(z_1-z_2)\delta(t_1-t_2) \int_0^{h(z_1)} 2\pi r dr \\
&\quad = 6k_B T\eta\pi h^2(z_1)\delta(z_1-z_2)\delta(t_1-t_2).
\end{aligned} \tag{3.43}$$

Similarly, since the correlation $\left\langle \frac{1}{2}(s_{31}x_1 + s_{32}y_1), \frac{1}{2}(s'_{31}x_2 + s'_{32}y_2) \right\rangle$ can be simplified using Eq. (3.33) as

$$\begin{aligned}
&\left\langle \frac{1}{2}(s_{31}x_1 + s_{32}y_1), \frac{1}{2}(s'_{31}x_2 + s'_{32}y_2) \right\rangle \\
&\quad = \frac{x_1x_2}{4}\langle s_{31}s'_{31}\rangle + \frac{x_1y_2}{4}\langle s_{31}s'_{32}\rangle + \frac{y_1x_2}{4}\langle s_{32}s'_{31}\rangle + \frac{y_1y_2}{4}\langle s_{32}s'_{32}\rangle \\
&\quad = \frac{x_1x_2}{4}\langle s_{31}s'_{31}\rangle + \frac{y_1y_2}{4}\langle s_{32}s'_{32}\rangle \\
&\quad = \frac{1}{4}(x_1x_2 + y_1y_2)\langle s_{31}s'_{31}\rangle \\
&\quad = \frac{1}{2}(x_1x_2 + y_1y_2)\, k_BT\eta\delta(x_1 - x_2)\delta(y_1 - y_2)\delta(z_1 - z_2)\delta(t_1 - t_2), \qquad (3.44)
\end{aligned}$$

the correlation $\langle M(z_1, t_1), M(z_2, t_2)\rangle$ is calculated as,

$$\begin{aligned}
&\langle M(z_1, t_1), M(z_2, t_2)\rangle \\
&\quad = \iint dx_1dy_1 \iint dx_2dy_2 \left\langle \frac{1}{2}(s_{31}x_1 + s_{32}y_1), \frac{1}{2}(s'_{31}x_2 + s'_{32}y_2) \right\rangle \\
&\quad = \iint dx_1dy_1 \iint dx_2dy_2 \frac{k_BT\eta}{2}(x_1x_2 + y_1y_2) \\
&\quad \times \delta(x_1 - x_2)\delta(y_1 - y_2)\delta(z_1 - z_2)\delta(t_1 - t_2) \\
&\quad = \frac{k_BT\eta}{2}\delta(z_1 - z_2)\delta(t_1 - t_2) \iint dx_1dy_1(x^2 + y^2) \\
&\quad = \frac{k_BT\eta}{2}\delta(z_1 - z_2)\delta(t_1 - t_2) \int_0^{h(z_1)} rdr2\pi r^2 \\
&\quad = \frac{\pi k_BT\eta h^4(z_1)}{4}\delta(z_1 - z_2)\delta(t_1 - t_2). \qquad (3.45)
\end{aligned}$$

Note that as $h \to 0$ the contribution of the fluctuations $M(z, t)$ is much smaller than the contribution of $N(z, t)$. This can be seen from the fact that the correlation of $M(z, t)$ is proportional to $h^4$ while the correlation of $N(z, t)$ is proportional to $h^2$. In the nanometer scale, it is appropriate to neglect $M(z, t)$ and consequently $I_s^{(0,z)}$ turns to be

$$I_s^{(0,z)} = [N(z, t)]' = [\sqrt{3\pi k_BT}\, h(z)\Gamma(z, t)]', \qquad (3.46)$$

where $\Gamma(z, t)$ is a Gaussian white noise with a correlation of

$$\langle \Gamma(z_1, t_1)\Gamma(z_2, t_2)\rangle = 2\delta(z_1 - z_2)\delta(t_1 - t_2). \qquad (3.47)$$

Plug $I_\rho^{(0,\bar{z})}$, $I_\gamma^{(0,\bar{z})}$, $I_\eta^{(0,\bar{z})}$, and $I_s^{(0,\bar{z})}$ into Eq. (3.34), and change the variable of the equation from $\bar{z}$ back to z; we obtain that

$$\rho\left(\dot{v}_0 + v_0 v_0'\right) = -\gamma\kappa' + \frac{3\eta(h^2 v_0')'}{h^2} - \sqrt{\frac{3k_B T}{\pi}}\frac{(h\Gamma)'}{h^2}. \tag{3.48}$$

Together with Eq. (3.26) obtained from kinematic boundary condition, Eq. (3.48) forms the stochastic lubrication equations.

## *3.2 The concepts of scaling, self-similarity and universality*

The concepts of scaling, self-similarity and universality are often discussed in the studies of breakup of liquid structures. Essentially, they are ubiquitous mathematical concepts and are also important topics of a variety of branches of physics, such as the critical phenomena in phase transition [59, 41], fractal surface growth [1] and chaos in dynamical systems [66]. Because of the ubiquity of these ideas, it is convenient to introduce them in a mathematical way and put off associating them with specific physical contexts.

### 3.2.1 Scale transform and scale invariance

For a function (or a curve) f(x), there are several basic scale transforms, including stretch, compress, and reflection, that can change the ratio of the function (or curve) on different directions.

The horizontal stretch or compress can be expressed as,

$$f(x) \to f(cx), \tag{3.49}$$

where, $c$ is an arbitrary positive constant. When $c > 1$, Transform (3.49) is called compress, while when $c < 1$, Transform (3.49) is called stretch. Similarly, vertical stretch and compress are defined as,

$$f(x) \to cf(x), \tag{3.50}$$

where $c$ is a positive number. When $c > 1$, Eq. (3.50) defines a stretch; and when $c < 1$ Eq. (3.50) defines a compress. Reflections with respect to horizontal and vertical axes can also be defined in similar ways when the constant $c$ in Transforms (3.49) and (3.50) can be negative numbers.

Suppose a function or curve $f(x)$ has the property,

$$f(x) = c^{\lambda} f(cx), \tag{3.51}$$

under scale transforms for an arbitrary scale constant $c$ and for a fixed exponent $\lambda$, the function $f(x)$ is considered scale invariant and $\lambda$ is called the scaling exponent. The scale invariance implies that any deformation of the function's shape caused by a horizontal scale transform, characterized by the scale constant $c$, is recovered by a vertical scale transform with a scale constant $c^{\lambda}$.

Usually, in a physical system, there are several quantities having the scale invariant properties. The values of the corresponding scaling exponents and the relationship between them are often called the "scaling law" of the system. For example, in the theory of critical phenomena, the scaling law refers to the determination of the value and the relation of the critical exponents; while in the studies of axisymmetric liquid flows, the scaling law in their breakup processes amounts to the determination of the exponents describing the variation of the free surface and the change of the axial velocity.

Power functions $f(x) = x^a$ with $a \in \mathbb{R}$ are simple but important examples of scale-invariant functions. According to the definition of the scale invariance in Eq. (3.51), the order, $a$, of the power function is equal to its scaling exponent $\lambda$. Remarkablely, in physical applications, the asymptotic behavior of a scale-invariant quantity often has the form of a power function.

### 3.2.2 The concept of self-similarity

A concept related to scale invariance is the idea of self-similarity. In different contexts, "self-similarity" refers to things with minor differences. In the study of fractals and surface growths [1, 61], the self-similarity is a pure geometric idea. It suggests that part of a geometric structure is similar to the structure itself. A simple example of geometric self-similarity is a Cantor set [66]. However, when a physical quantity is time-dependent, the self-similarity often refers to the fact that the values of the physical quantity at various moments can be collapsed to a common spatial function by scale transforms [8, 27]. This concept can be expressed as,

$$f(\mathbf{r}(t), t) = f_0\, t^{\gamma} \phi(\mathbf{q}), \tag{3.52}$$

where, $f(\mathbf{r}(t), t)$ is the time-dependent physical quantity, $\mathbf{r}$ is its position vector, $f_0$ is a constant that takes care of the dimension of the equation, $\gamma$ is the scaling exponent, and $\phi(\mathbf{q})$ is the dimensionless model function with respect to the dimensionless spatial variables $\mathbf{q}$. Generally, $\mathbf{q}$ are obtained from the position vector $\mathbf{r}$ by a transform,

$$q_\alpha = q_{0,\alpha}\, t^{\gamma_\alpha} r_\alpha, \tag{3.53}$$

where $\alpha$ denotes different spatial components of $\mathbf{r}$ and $\mathbf{q}$; $q_{0,\alpha}$ is an arbitary constant that makes $q_\alpha$ dimensionless; and $\gamma_\alpha$ is the scaling exponent of different components of $\mathbf{r}$. Note that the scaling exponents of different directions are not necessarily equal.

Physically, all the phenomena that show self-similarity share a common property, i.e., they do not possess a fixed characteristic length scale. For example, in critical phenomena, the correlation length of the system is divergent as the system approaches the critical point; and in the pinching process of axisymmetric flows, the minimum radius of the liquid structure decreases to zero as the flow approaches its breaking point. This common property offers a practical criterion for the appearance of self-similarity phenomena.

## *3.3 Fokker-Plank description for stochastic differential equations and the most probable trajectory*

Though the stochastic lubrication equations [55] provide a description to all the "trajectories" of nanoscale liquid structures; however, for a specific set of noise, only one of the trajectories can be obtained by solving the equations directly. They are not convenient for the theoretical analysis of the statistical properties of the entire system. In order to obtain the statistical properties, the distribution of the "trajectories" should be calculated in some way.

Since the stochastic lubrication equations [55] are essentially a set of stochastic partial differential equations, the general concepts and methods used in the study of stochastic differential equations can also be applied to the stochastic lubrication equations. Fokker-Plank equation method is one of the powerful tools to deal with stochastic differential equations. It is the time evolution equation of the probability distribution of all the "trajectories" and can be derived from the stochastic differential equations by truncating the Kramers-Moyal expansion [77, 46, 63] to the second order spatial derivatives of all the stochastic variables [77, 26].

### 3.3.1 Fokker-Planck equation

Generally, a one-dimensional stochastic differential equation with only one stochastic variable is written as,

$$\dot{x} = f(x,t) + g(x,t)\Gamma(t), \tag{3.54}$$

where $\Gamma(t)$ is a Gaussian white noise with a correlation of $\langle \Gamma(t)\Gamma(t')\rangle = 2D\delta(t-t')$, and $g(x,t)$ is the variable-related noise strength. $D$ is the strength of the white noise $\Gamma(t)$. The corresponding Fokker-Plank equation for Eq. (3.54) is [26]

$$\frac{\partial \rho(x,t)}{\partial t} = -\frac{\partial}{\partial x}\left\{\left[f(x,t) + Dg'(x,t)g(x,t)\right]\rho(x,t)\right\} + D\frac{\partial^2}{\partial x^2}\left[g(x,t)^2\rho(x,t)\right], \tag{3.55}$$

where $\rho(x,t)$ is the probability distribution. Note that, here the stochastic force $g(x,t)\Gamma(t)$ is interpreted following the Stratonovich's way [81] and this interpretation

will be adopted for the entire thesis.

For a system with multiple discrete stochastic variables,

$$\dot{x}_i = f_i(x,t) + \sum_{j=1}^{m} g_{ij}\Gamma_j(t) \qquad i = 1,2,3,\ldots \tag{3.56}$$

with Gaussian white noise $\langle \Gamma_i(t)\Gamma_j(t')\rangle = 2D\delta_{ij}\delta(t-t')$, the corresponding Fokker-Plank equation is a simple generalization of the one-variable case. It can be written as [26],

$$\frac{\partial \rho(\mathbf{x},t)}{\partial t} = -\sum_i \frac{\partial}{\partial x_i}\left[D_i(\mathbf{x},t)\rho(\mathbf{x},t)\right] + \sum_i \sum_j \frac{\partial^2}{\partial x_i \partial x_j}\left[D_{ij}(\mathbf{x},t)\rho(\mathbf{x},t)\right], \tag{3.57}$$

where

$$D_i(\mathbf{x},t) = f_i(\mathbf{x},t) + D\sum_k \sum_j g_{kj}\frac{\partial g_{ij}}{\partial x_k}, \tag{3.58}$$

and

$$D_{ij}(\mathbf{x},t) = D\sum_k g_{ik}g_{jk}. \tag{3.59}$$

This result can be further generalized to systems with continuous stochastic variables (the so-called spatially extended systems) [31] through finite-difference method. For the following general stochastic partial differential equations (in the discrete form)

$$\frac{\partial \phi_i}{\partial t} = f_i(\{\phi\}) + \sum_j g_{ij}(\{\phi\})\eta_j(t), \tag{3.60}$$

the corresponding Fokker-Plank equation is [31]

$$\frac{\partial \rho}{\partial t} = -\sum_i \frac{\partial}{\partial \phi_i}(f_i\rho) + \sum_{ijkl}\frac{\partial}{\partial \phi_i}\left[g_{ij}\frac{\partial}{\partial \phi_l}(C_{jk}g_{lk}\rho)\right]. \tag{3.61}$$

where $\phi_i$ is the stochastic variable, and $\eta_i(t)$ is a color noise with the following correlation relation,

$$\langle \eta_i(t)\eta_j(t')\rangle = C_{ij}2\delta(t-t'). \tag{3.62}$$

Note that the forms of Eq. (3.57) and Eq. (3.61) are similar; however, Eq. (3.61) emphases the difference between stochastic variables (field) and spatial variables (coordinates).

Usually, the expression of $g_{ij}(\{\phi\}, t)$ is complicated if the system has spatial couplings. It keeps us from writing Eq. (3.61) in a simple general continuous form. For some simple couplings, such as $g_{ij} = g_i \delta_{ij}$, the continuous Fokker-Plank equation can be written in a functional form as

$$\frac{\partial \rho}{\partial t} = \int dx' \frac{\delta}{\delta \phi(x')} \left[ f(\phi(x', t)) \rho \right] + \int dx' \int dx" \frac{\delta}{\delta \phi(x')} \left\{ g(\phi(x', t)) \frac{\delta}{\delta \phi(x")} \left[ C(x' - x") g(\phi(x", t) \rho) \right] \right\}, \quad (3.63)$$

where $\phi(x')$ is the field variable denoted by its coordinate $x'$; $\delta$ is the functional variation operator. Note that the probability density $\rho$ itself is also a functional of the field $\phi(x)$.

### 3.3.2 The most probable trajectory

Accurate solution to the Fokker-Plank equation (3.63) is often not easy to obtained. However, for many physical systems, the probability density $\rho$ concentrates around some "trajectories" when the noise term in the stochastic differential equations can be regarded as perturbations. i.e., $C_{ij}$ in Eq. (3.62) is much smaller than 1. This idea leads to the so-called "small noise" expansion, and the leading terms of the small noise expansion form the equations of motion for the most probable trajectory of the system.

The general formula for the expansion is tedious. For simplicity, we only illustrate the concept with the Fokker-Plank equation for just one stochastic variable. Though the formula is for a one-stochastic-variable system, it is easy to generalized to multiple-stochastic-variable and spatially extended systems. Suppose the time-dependent stochastic process is Markovian, the probability density $\rho$ is formally expressed as

$$\rho(x, t) = \int dx' K(x, t; x', 0) \rho(x'), \quad (3.64)$$

where, $\rho(x')$ is the initial probability density; and $K$ is the response functional (or

the propagator). Assume $K$ has the form

$$K\left(x,t;x',0\right)=\exp\left[-\frac{1}{D}R\left(x,t;x',0\right)\right]; \tag{3.65}$$

and insert the expression of $\rho$ into both sides of the Fokker-Plank equation. We obtain that,

$$\frac{\partial\rho}{\partial t}=\int dx'\left(-\frac{1}{D}\frac{\partial R}{\partial t}\right)K\rho(x'), \tag{3.66}$$

which is just the following complicated equation,

$$\begin{aligned}
&-\frac{\partial}{\partial x}\left\{\left[f(x,t)+Dg'(x,t)g(x,t)\right]\rho(x,t)\right\}+D\frac{\partial^2}{\partial x^2}\left[g(x,t)^2\rho(x,t)\right]\\
&\quad=\int dx'\left\{-\frac{\partial}{\partial x}\left[\left(f+Dg'g\right)K(x,t;x',0)\right]+D\frac{\partial^2}{\partial x^2}\left(g^2K(x,t;x',0)\right)\right\}\rho(x')\\
&\quad=\int dx'\left[-(f+Dg'g)'K+(f+Dg'g)\frac{K}{D}\frac{\partial R}{\partial x}\right]\rho(x')\\
&\quad+\int dx'\left[D(g^2)''K-2(g^2)'K\frac{\partial R}{\partial x}-g^2K\frac{\partial^2R}{\partial x^2}+\frac{g^2K}{D}\left(\frac{\partial R}{\partial x}\right)^2\right]\rho(x'),
\end{aligned} \tag{3.67}$$

and accordingly,

$$\begin{aligned}
\frac{\partial R}{\partial t} &= D(f+Dg'g)'-(f+Dg'g)\frac{\partial R}{\partial x}-D^2(g^2)''+2D(g^2)'\frac{\partial R}{\partial x}\\
&\quad+Dg^2\frac{\partial^2R}{\partial x^2}-g^2\left(\frac{\partial R}{\partial x}\right)^2.
\end{aligned} \tag{3.68}$$

Keeping all the terms in Eq. (3.68) to the lowest order of $D$, Eq. (3.68) is simplified to

$$\frac{\partial R}{\partial t}+\left[f\frac{\partial R}{\partial x}+g^2\left(\frac{\partial R}{\partial x}\right)^2\right]=0, \tag{3.69}$$

which has the exact form of the Hamilton-Jacobi equation [24],

$$\frac{\partial R}{\partial t}+H(\frac{\partial R}{\partial x},x;t)=0. \tag{3.70}$$

This result suggests that the most probable trajectory of the system can be obtained by solving the following Hamilton equations,

$$\dot{p} = -\frac{\partial H}{\partial x}=-f'p-2gg'p^2, \tag{3.71}$$

$$\dot{x} = \frac{\partial H}{\partial p}=f+2g^2p, \tag{3.72}$$

where $p=\dfrac{\partial R}{\partial x}$, and the Hamiltonian is $H=fp+g^2p^2$.

## 3.4 Statistical moment description for stochastic partial differential equations

In some cases, such as in the linear instability analysis of axisymmetric nano liquid flows, it is more convenient to use the statistical moment description. For spatially extended systems described in Eq. (3.60), its n-th order statistical moment is defined as,

$$M_n(i_1, i_2, \ldots, i_n, t) = \langle \phi_{i_1}, \phi_{i_2}, \ldots, \phi_{i_n} \rangle . \tag{3.73}$$

The first two moments have particular meaning to us. When $n = 1$ , $\langle \phi_i \rangle$ is the average of the stochastic variable $\phi_i$; when $n = 2$, $\langle \phi_i \phi_j \rangle$ is the correlation of the two stochastic variables $\phi_i$ and $\phi_j$. From the corresponding Fokker-Planck equation [Eq. (3.63)], the evolution equation of the average $\langle \phi_i \rangle$ is obtained as [31],

$$\frac{\partial}{\partial t} \langle \phi_i(t) \rangle = \langle f_i(\{\phi\}) \rangle + \sum_{jkl} \left\langle \left( \frac{\partial g_{ij}}{\partial \phi_l} \right) C_{jk} g_{lk} \right\rangle . \tag{3.74}$$

Similarly, the evolution equation for the correlation function is obtained as [31],

$$\begin{aligned} \frac{\partial}{\partial t} \langle \phi_i(t) \phi_j(t) \rangle = & \langle f_i \phi_j \rangle + \langle \phi_i f_j \rangle + \sum_{lm} [\langle g_{il} C_{lm} g_{jm} \rangle] \\ & + \sum_{lmn} \left[ \left\langle \phi_j \left( \frac{\partial g_{il}}{\partial \phi_n} \right) C_{lm} g_{nm} \right\rangle + \left\langle \phi_i \left( \frac{\partial g_{jl}}{\partial \phi_n} \right) C_{lm} g_{nm} \right\rangle \right] . \end{aligned} \tag{3.75}$$

In practice, the Fourier transform of the correlation $\langle \phi_i \phi_j \rangle$ is often used. Since it provides quantitative spatial structure information of the system, it is also called the "structure function". The definition of the structure function is,

$$S(k, t) = \mathcal{F} \left( \sum_i \langle \phi_i, \phi_{i+j} \rangle \right) , \tag{3.76}$$

where $\mathcal{F}$ is the Fourier transform operation. This is equivalent to the following definition,

$$S(k, t) = \langle \phi(k) \phi(-k) \rangle = \langle \phi(k) \phi^*(k) \rangle , \tag{3.77}$$

where $\phi(k)$ is the Fourier transform of $\phi_i$, and "$*$" refers to the complex conjugate of $\phi$.

# CHAPTER IV

# PINCHING DYNAMICS OF LIQUID NANOBRIDGES IN VACUUM

The pinching dynamics of liquid nanojets or nanobridges is an important aspect of microscopic hydrodynamics because of the prospective application of nanoscale liquid devices in many areas, such as printing [93], spraying [97], and biomaterial delivery [3, 85]. Another attraction of pinching dynamics is the new phenomena caused by thermal fluctuations in the break-up process of a nanoscale liquid flow, where self-similar break-up profiles, scaling laws and finite-time singularities appear as the result of the interaction between thermal fluctuations and the confinement provided by the free surface of nanoscale liquid structures.

Previous Molecular Dynamics simulations [55] showed that for a propane nanojet of 6 nm in diameter, the final break-up profile is two cones joined at their apexes, which is qualitatively different from the long-thread break-up profile of a macroscopic viscous liquid jet [15]. Moreover, the simulations also showed that the break-up speed of a nanojet is much faster than the prediction provided by macroscopic hydrodynamical equations. To account for the difference, Moseler and Landman [55] incorporated the effect of thermal fluctuations into hydrodynamical equations in a stochastic way [48]. To avoid the tremendous difficulty in solving the 3-dimensional Navier-Stokes equations, they devised, through the "lubrication approximation" [62], a set of 1-dimensional stochastic lubrication equations (SLE),

$$\begin{aligned} \partial_t v + v\partial_z v &= -\frac{\gamma}{\rho}\partial_z \kappa + 3\frac{\eta}{\rho}\partial_z(h^2\partial_z v)/h^2 \\ &\quad -\frac{1}{\rho}\sqrt{\frac{3k_B T\eta}{\pi}}\partial_z(hN)/h^2, \end{aligned} \tag{4.1}$$

$$\partial_t h + v\partial_z h = -(\partial_z v)h/2, \tag{4.2}$$

which we have discussed in Chapter 3 thoroughly. In the above equations, $v(z,t)$ is the axial velocity of the nanojet, $h(z,t)$ is the radius of the nanojet, $\rho$ is the density of the liquid, $\gamma$ is the surface tension, and $\eta$ is the viscosity. In the last term of Eq. (4.1), $N$ is a Gaussian white noise with a correlation relation of $\langle N(z,t)N(z',t')\rangle = 2\delta(z - z')\delta(t - t')$, where $k_B$ is the Boltzmann constant and $T$ is the temperature of the nanojet. Numerical integration of the stochastic lubrication equations for a nanojet, which had the same size as in the molecular dynamics simulations, also showed that the breakup is changed fundamentally, i.e., with the stochastic term, the stochastic lubrication equations yielded a similar symmetric break-up profile with two cones joined at their apexes.

Theoretical analysis [18] of the stochastic lubrication equations also showed that it were thermal fluctuations, not surface tension, which was the driving force of the break-up process in a nanojet system. Near the breaking point, the break-up profile was self-similar and it could be collapsed onto a universal similar profile. When the breakup is approached, the pinch-off of a nanojet was described by a power law with an exponent of 0.418. This was quite different from the macroscopic pinching case, where $h(z,t)$ decreases linearly and the break-up profile is asymmetric.

In this chapter, we show that the double-cone break-up profile is universal and self-similar through direct theoretical assessment of the influence of thermal fluctuations confined by the free surface of nanoscale liquid structures. A power-law pinching is yielded with an exponent of 0.375. These results are confirmed by the molecular dynamics simulations of a propane nanobridge of 6 nm in diameter. In the simulations, the universal self-similar break-up profiles are shown explicitly and the power-law pinching exponent is measured as $0.40\pm0.02$, which is very close to our theoretical analysis and in agreement with the previous theoretical prediction from Eggers [18].

## *4.1 Technical remarks on molecular dynamics simulations*

In the simulations, the liquid nanobridge is composed of propane molecules ($C_3H_8$) which are modeled in the same way as in the previous studies [55]. Detailed information of the model can be found in Section 2.2. Since propane molecules are non-polar short-chain alkanes and the interaction between molecules is treated using a short range 6-12 Lennard-Jones potential, liquid propane is a good example of simple Newtonian fluid. Accordingly, the hydrodynamic properties demonstrated by liquid propane are expected to be typical for other simple Newtonian fluids.

The initial shape of the nanobridge is a cylindrical column of 30 nm length (L) and 3 nm radius (h), attached to two short cylindrical end caps (see Fig. 4(a)). For each of the cap, the diameter is 8 nm and the thickness is 2 nm. The positions of the molecules in the caps are held fixed during simulations. The cylinder is cut out from propanes equilibrated at 185 K and 0 Pa, in a right box of 30 nm $\times$ 4 nm $\times$ 4 nm and with periodic boundary conditions. For convenience, the symmetrical axis of the initial liquid cylinder is called the $z$ axis. Note that the ratio of length to diameter for the nanobridge is assigned greater than $\pi$ according to the Rayleigh instability theory [17, 73, 44] to trigger the break-up process. All the simulations are performed in a cubic calculation cell with a length of 30 nm, and the nanobridge is placed at the center of the cube, as displayed in Fig. 4. The boundary of the calculation cell is displayed by the blue cubic frame surrounding the nanobridge. Propane molecules crossing the boundary of the calculation cell are removed from the simulation. To ensure that the nanobridge is actually in the liquid state, every time at the beginning of the simulation, the entire nanobridge is thermalized to 185 K (within the temperature range of liquid propane) through the Brownian dynamics method [56] with a independent set of thermal noise.

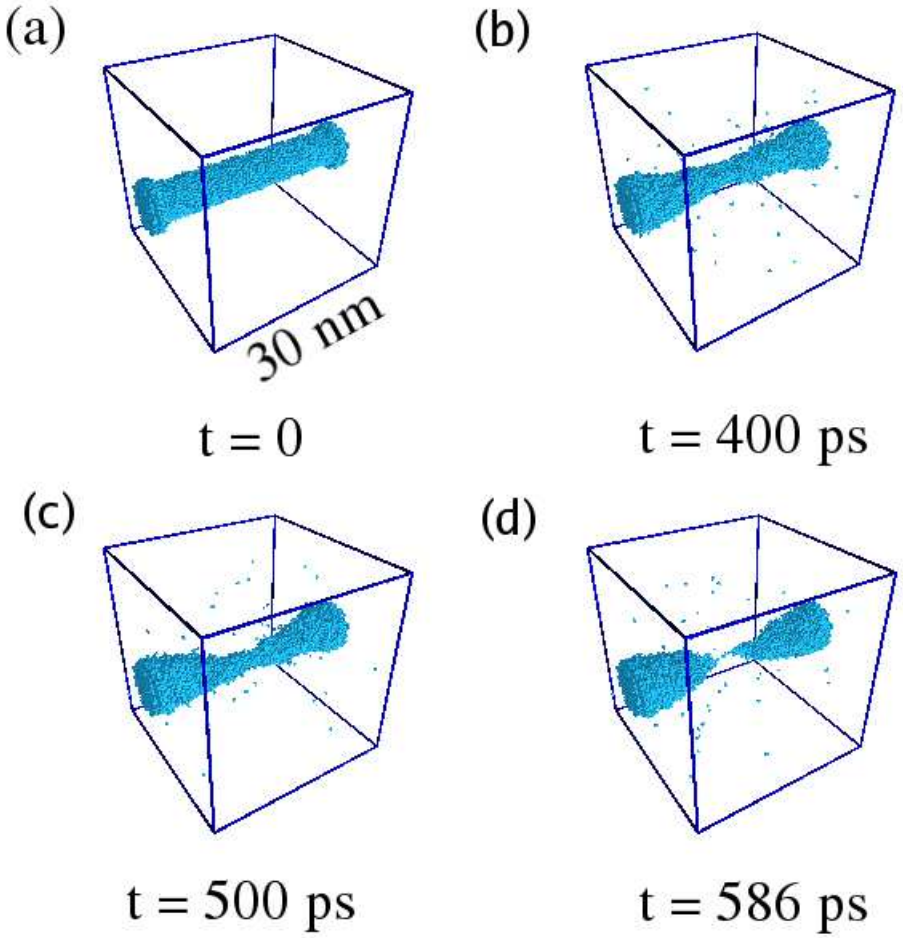


**Figure 4:** Selected configurations from a typical break-up process of a propane nanobridge at (a) t = 0, (b) 400 ps, (c) 500 ps and (d) 586 ps. The cubic frames with a length L = 30 nm in the figures are the boundaries of the calculation cells; and the break-up profile with two cones at their apexes, displayed in (d), is the snapshot just before the breakup.

## *4.2 The break-up profile of a nanobridge*

The stochastic feature of a nanoscale liquid structure revealed in the studies of nanojets [55, 18] implies a fundamental change in the description of the dynamics of a liquid structure at the nanoscale. In the traditional description of a macroscopic liquid structure, the entire system evolves along a deterministic "trajectory". However, in the stochastic description, such a deterministic "trajectory" does not exist; the dynamical property of the system is determined by a distribution function of all the

possible trajectories. For a nanobridge, a complete description of its break-up process includes (1) finding out all the possible break-up processes, and (2) determining the occurring probability of each of them.

Fortunately, as pointed out in Ref. [18], in the break-up process of a nanoscale liquid structure with axial symmetry, the probability distribution of the "trajectories" is concentrated around a particular "trajectory", whose dynamical behavior is typical for most of the "trajectories". This significantly simplifies the description of the break-up process of a nanobridge and the main task is reduced to understanding the typical break-up process. Here, we should point out that the appearance of a typical "trajectory" in a stochastic system does not imply the vanishing of the stochastic features; and that the typical "trajectory" usually differs from the "trajectory" obtained from a deterministic equation.

A typical break-up process of the nanobridge is displayed in Fig. 4 (a-d). Fig. 4(d) clearly shows that the typical break-up profile is double cones joined at their apexes. Recall that the same double-cone break-up profile also occurs in a nanojet system [55]. The reappearance of this break-up profile in a nanobridge system provides further support to the universality of the break-up profile in nanoscale liquid structures. To ensure that the break-up process displayed in Fig. 4 (a-d) is the typical break-up process of the system, the simulation of the same nanobridge system is conducted 15 times with independent thermal noise in the initial conditions; only one of the break-up processes, with a long-thread break-up profile, is different from Fig. 4 (a-d).

## *4.3 Power-law pinching of a nanobridge*

The radius $h(z,t)$ of a nanobridge (as a function of its z coordinate) of every snapshot (such as those displayed in Fig. 4) is extracted from the positions of propane molecules as follows. First, the calculation cell is divided into 60 bins along the z axis, each bin having a thickness of 0.5 nm. Following that, the center of mass of the propane

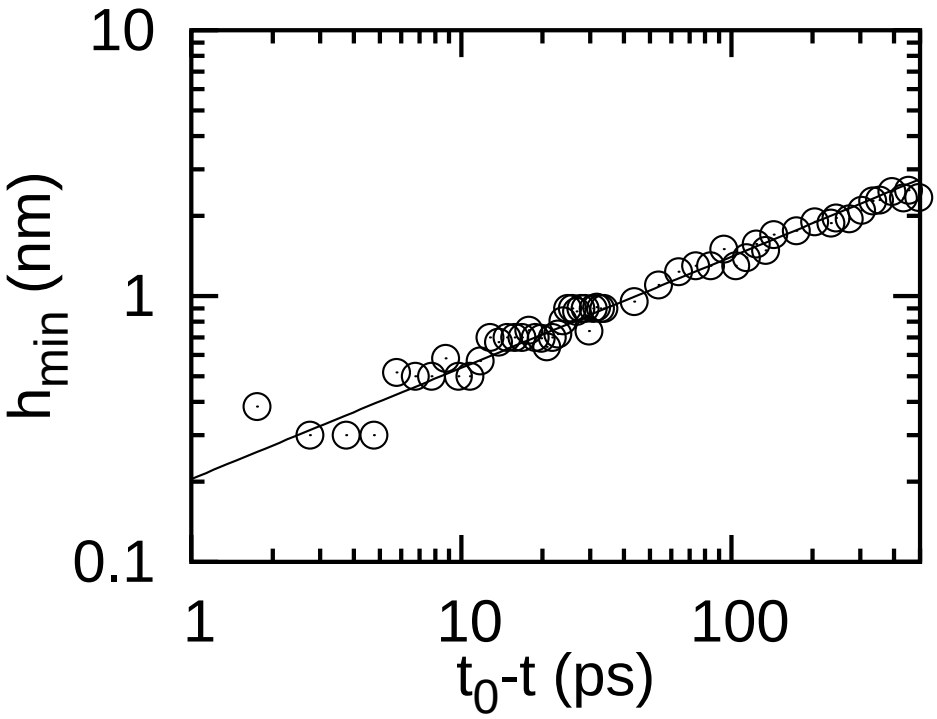


**Figure 5:** The time dependence of the minimum neck, $h_{min}(t)$, of the nanobridge plotted on log-log scale coordinates. The abscissa is $t_0 - t$ with $t_0$ the break-up time. The open circles in the figure are measured values obtained from the molecular dynamics simulations and the solid line is the theoretical prediction [18], i.e., $h_{min}(t) \sim (t_0 - t)^{0.418}$.

molecules in each bin is assessed, and it is used as the center of the disk-like liquid slice in that bin. Note that using the center of mass as the center of the liquid slice is a crucial step of the measurement of the radius profile. Without this step, the measured radius is larger than its real value because the nanobridge oscillates arround the z axis during the break-up process. Then, for each bin, the density histogram, denoted as $\rho_b(r, t)$, of propane molecules is calculated in annular rings with a radial increment of 0.2 nm. The surface of the liquid slice is located at the ring where the density of propane molecules drops to $0.09 \times 10^3$ kg/m$^3$ (about 1/6 of the density at the center of the initial cylinder). The radius of the liquid slice is assigned as the average radius of the annual ring where the surface is located. Since the density of propane molecules decreases rapidly on the liquid surface, the position of the surface is insensitive to

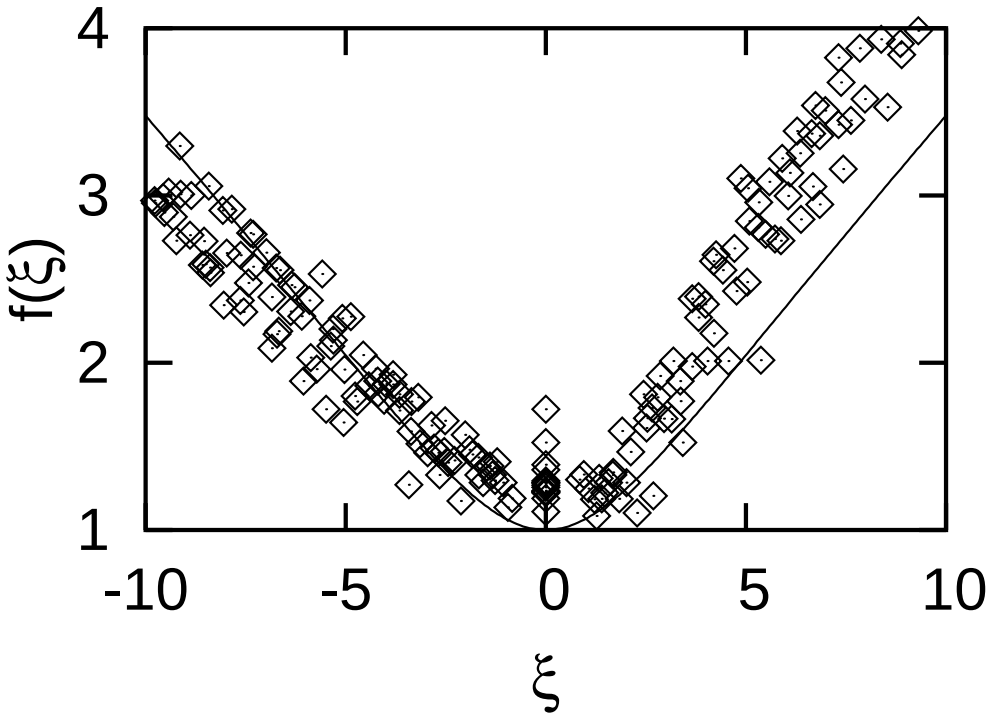


**Figure 6:** The universal similar profile function $f(\xi)$. The diamond points in the figure are obtained by rescaling $h(z,t)$ at $t_0 - t$ = 8 ps, 13 ps, 18 ps, 23 ps, 28 ps, 33 ps, 38 ps, 43 ps, 48 ps, 53 ps, 58 ps, 63 ps, 83 ps, 103 ps, and 133 ps, according to Eq. (4.3) with the indices $\alpha = 0.40$ and $\beta = 0.50$. The solid line in the figure is the similarity function predicted by the theory [18], which has a functional form of $f(\xi) = \sqrt{F(-2\alpha,\ \beta,\ -\xi^2/12)}$. Here, $F$ is the confluent hypergeometric function, $\alpha$ = 0.418 and $\beta = 0.5$.

the choice of the cutoff density. The particular value of the cutoff density adopted here is a compromise of capturing the radius profile around the break-up point and depressing the uncertainty in the radius measurement caused by thermal fluctuations. The former requires the cutoff density as small as possible and the latter requires that there are enough molecules within the liquid surface. Finally, the uncertainty of the radius profile is further reduced by averaging the $h(z,t)$ for 1 ps (200 time steps) about the time of each snapshot.

As the breakup is approached, as displayed in Fig. 4(d), the radius profile $h(z,t)$ of a nanobridge decreases to zero at the vicinity of the break-up point. Since the break-up process does not have a fixed characteristic length scale, we can suppose

$h(z,t)$ is self-similar [8] as $t$ approaches the break-up time $t_0$. The self-similar $h(z,t)$ can be depicted by a universal ansatz,

$$h(z,t) = \frac{\ell_c}{t_c^\alpha}(t_0 - t)^\alpha f\left(\frac{t_c^\beta}{\ell_c}\frac{z}{(t_0-t)^\beta}\right), \tag{4.3}$$

where the break-up point is the origin of the coordinate $z$, $\alpha$ and $\beta$ are scaling indices along the vertical and horizontal directions respectively, $\ell_c$ is a fixed length scale and $t_c$ is a fixed time scale. Both $\ell_c$ and $t_c$ are used to balance the dimension of both sides of the ansatz (Eq. (4.3)). Here we choose $\ell_c = l_\eta = \eta^2/(\rho\gamma)$ and $t_c = t_\eta = \eta^3/(\rho\gamma^2)$ for the nanobridge. The function $f$ is the "model" function of the radius profile $h(z,t)$ at various moment, i.e., all the $h(z,t)$ is obtained by stretching or compressing $f$, in both the horizontal and perpendicular directions. Note that the function $f$ is also a function with respect to the dimensionless spatial variable $\xi$, with $\xi = (t_c^\beta/\ell_c)(z-z_0)/(t_0-t)^\beta$.

The expression of the minimum neck $h_{min}(t)$ of a nanobridge is obtained by putting $z = 0$ in Eq. (4.3). As $t$ approaches the break-up time $t_0$, $h_{min}(t)$ has a simple power law relation,

$$h_{min}(t) \sim (t_0 - t)^\alpha. \tag{4.4}$$

In Fig. 5, the time dependence of the minimum neck $h_{min}(t)$ is plotted on log-log scale coordinates, where the power exponent $\alpha$ is the slope of $\log(h_{min}(t))$ with respect to the variable $\log(t_0 - t)$. The average value of $\alpha$ obtained from the molecular dynamics simulations is $0.40 \pm 0.02$. Recall that the theoretical analysis [18] of the stochastic lubrication equations [55] yielded a power exponent of 0.418. Our measurement is within 5% of the theoretical prediction.

The shape of the function $f(\xi)$ and the corresponding scaling exponent $\beta$ can also be measured from the molecular dynamics simulations. As aforementioned, the radius profile $h(z,t)$ of a nanobridge is obtained by rescaling $f(\xi)$ in both vertical and horizontal directions. Now that $h(z,t)$ at various moments have been measured in the simulation, the shape of $f(\xi)$ can be obtained by the reverse scaling procedure,

provided that the scaling (dilation) factors are determined. For a nanobridge, the scaling factor in the vertical direction is $(t_0 - t)^\alpha \ell_c / t_c^\alpha$, and in the horizontal direction it is $(t_0 - t)^\beta \ell_c / t_c^\beta$. Note that here $\beta$ still remains undetermined.

Unlike the scaling exponent $\alpha$, there is no way to measure the scaling exponent $\beta$ directly. However, in the simulation we find that to collapse the radius profile $h(z,t)$ onto a universal function, which is just the function $f(\xi)$, $\beta$ can only take a certain value. It turns out that the best value of $\beta$ in the simulation is 0.5, and the corresponding universal function $f(\xi)$ is displayed as diamond symbols in Fig. 6. To confirm that the curve thus obtained is the function $f(\xi)$, the universal function $f_t(\xi) = \sqrt{F(-2\alpha, \beta, -\xi^2/12)}$ obtained from the theoretical analysis [18] is plotted in the same figure as the solid curve. Here, $F$ is the confluent hypergeometric function, $\alpha$ takes the value of 0.418, and $\beta$ takes the value of 0.5. It is easy to see that the shapes of the two curves are very close.

## *4.4 Scaling analysis*

When the size of a liquid structure decreases to the nanometer scale [2], the continuum Navier-Stokes equations alone can become inadequate because of the dominance of thermal fluctuations. Usually, the effect of thermal fluctuations are described by the relative fluctuations of a system, which is inversely proportional to the square root of the number of particles in the system. For a liquid nanobridge with a typical size of several nanometers, the number of molecules is on the order of $10^3$; while for macroscopic liquid structures, the number of molecules is on the order of Avogadro's number, which is $6.02 \times 10^{23}$. This implies that the effect of thermal fluctuations in a nanobridge are $10^{10}$ times larger than that in a macroscopic liquid bridge. The effect of thermal fluctuations are also characterized by a typical thermal length scale [55] $l_T = (k_B T/\gamma)^{1/2}$, which is usually on the order of several nanometers. When the typical length of the nanobridge is comparable with $l_T$, the effect of thermal fluctuations

becomes important [55].

Since the correlation of the fluctuations N is $\langle N(z,t)N(z',t')\rangle = 2\delta(z-z')\delta(t-t')$, and the dimension of $\delta(z-z')\delta(t-t')$ is $[L]^{-1}[T]^{-1}$, the average effect of thermal fluctuations can be estimated as $1/(l_N\ t_N)^{1/2}$. Here, $l_N$ and $t_N$ are respectively the characteristic length and the characteristic time of the thermal fluctuations in the break-up process of the nanobridge. This method of estimation of the effect of thermal fluctuations is inspired by the method proposed by Hentschel and Family [25] and it is also a new development of Kolmogorov's method [43] used in the study of turbulence.

Though the the entire break-up process of a nanobridge does not have a "global" length scale and time scale, the nanobridge has, nevertheless, two characteristic physical quantities at each moment. One is the minimum neck $h_{min}(t)$ of the nanobridge and the other is the nanobridge's maximum axial speed $v_{max}(t)$ along the $z$ axis. Since they are the only two characteristic quantities pertaining to the breakup of the nanobridge at a particular moment, $l_N$ and $t_N$ can be expressed using these two quantities as $l_N \sim h_{min}(t)$ and $t_N \sim h_{min}(t)/v_{max}(t)$. Also, since the break-up process is supposed to be self-similar, $h_{min}(t)$ has the same scaling as $h(t)$ and $v_{max}(t)$ has the same scaling as $v(t)$. This leads to the following scaling expression of $l_N$ and $t_N$ used in our scaling argument:

$$l_N \sim h(t), \tag{4.5}$$

$$t_N \sim h(t)/v(t). \tag{4.6}$$

Now, assume the scaling of $v(t)$ is $v(t) \sim (t_0-t)^\gamma$ as $t$ aproaches $t_0$ and insert it into Eqs. (4.1) and (4.2). Recall that $h(t) \sim (t_0-t)^\alpha$ and $z \sim (t_0-t)^\beta$, we arrive at the following two scaling index equations:

$$\bar{t}^{\gamma-1} + \bar{t}^{2\gamma-\beta} = -\bar{t}^{-\beta-\alpha} + \bar{t}^{\gamma-2\beta} - \bar{t}^{\frac{\gamma}{2}-\beta-2\alpha}, \tag{4.7}$$

$$\bar{t}^{\alpha-1} + \bar{t}^{\alpha-\beta+\gamma} = -\bar{t}^{\alpha-\beta+\gamma}, \tag{4.8}$$

where, $\bar{t} = (t_0 - t)$. Keep the leading terms in both equations, we obtain $\alpha = 0.375$, $\beta = \frac{1}{2}$ and $\gamma = -\frac{1}{2}$ by solving the equations. These results are also in good agreement with the previous measurements.

From the index Eqs. (4.7) and (4.8), the dominant influence of thermal fluctuations in the break-up process of a nanobridge can be seen clearly. As $t$ approaches the break-up time $t_0$, the surface tension term in Eq. (4.1), which is also the first term at the right hand side of Eq. (4.7), has a scaling of $\bar{t}^{-0.92}$ according to the molecular dynamics simulations. Other terms, including the thermal fluctuation term, have a scaling of $\bar{t}^{-1.5}$ calculated from Eq.(4.7). It is clear that the contribution of the surface tension is much smaller than the other terms and therefore drops out from the equation. This makes thermal fluctuations the only active driving force of the break-up process since the other terms in the equations are all passive (induced by the motion itself). This conclusion is also confirmed by the previous observations [55, 18].

Note that since the last term of Eq. (4.1) is just a one-dimensional expression of the fluctuations of the stress tensor in the three-dimensional Navier-Stokes equation, a direct physical picture of how a nanobridge breaks under the driving force of thermal fluctuations can be obtained as an analogue of the macroscopic breakup. For a macroscopic liquid bridge, the picture is as follows. The surface tension provides an extra effective pressure, which is roughly proportional to the reciprocal of the local radius. Then, the liquid is squeezed away from the regions of high pressure, which might be caused by small thermal fluctuations, and flows to the regions of lower pressure. This movement of the liquid in turn reduces the local radius and increases the pressure caused by surface tension. This is a positive feedback process; it does not stop until the breakup is reached.

In the nanobridge case, where thermal fluctuations are the driving force, a similar scenario for the break-up process is expected. As aforementioned, the relative thermal fluctuations are inversely proportional to the square root of the number of molecules

[49]. The number of molecules is in turn proportional to the volume that the molecules occupy (or in another word, the cube of the characteristic length), supposing the density of the liquid is a constant. Then, the break-up process driven by thermal fluctuations can be described as follows. The average effect of thermal fluctuations provides an extra local pressure, which is inversely proportional to the 3/2th power of the local radius $h$. When $h$ decreases to a length scale comparable with $l_T$, the pressure provided by thermal fluctuations outweighs the pressure caused by surface tension, which is inversely proportional to $h$. Liquid molecules are squeezed out of the places of higher pressure, caused by thermal fluctuations, and flow to the places of lower pressure. This process further increases the local thermal fluctuations and sustains the break-up process.

## *4.5 Discussion*

In summary, in this chapter, we reproduce the double-cone break-up profile in a nanobridge of 6 nm diameter; and reveal the self-similarity behind the break-up process using molecular dynamics simulation method. In particular, we measure the power-law decrease of the minimum neck of the nanobridge and determine the power exponents and the universal similarity function. These results agree well with the previous observations [55, 18]. By scaling analysis, we provide a clear physical picture for the break-up process of a nanobridge; and propose a new simple way to calculate the power exponents. The results of the calculation are close to the simulation results.

Note that the break-up process studied in this chapter is independent of the initial conditions and the boundary conditions far from the break-up point. The results obtained in this chapter are actually applicable to the break-up process of other nanoscale liquid structures; and therefore is useful to the design and applications of future nanoscale liquid devices.

# CHAPTER V

# THE SIZE-DEPENDENT INFLUENCE OF THERMAL FLUCTUATIONS AND THE VALIDITY OF THE LUBRICATION APPROXIMATION

The observation of a cascade of long-thread break-up structures in a viscous drop falling from a faucet [95] revealed a typical scenario of the break-up dynamics of axisymmetric liquid filaments [29, 45, 48, 11]. Numerical simulations [95, 29] based on the Navier-Stokes equations [48] showed that the repetition of forming self-similar long-thread structures would continue until it was interrupted by noise introduced *ad hoc* in the simulations [95]. These results are in accordance with the theoretical analysis [15, 16] based on the one-dimensional lubrication approximation of the Navier-Stokes equations. The analysis also indicated that the the minimum neck radius $h_{min}$ decreases linearly as long as liquid can be regarded as a continuous medium. However, the approximation of continuous medium ceases to work when the diameter of the long-thread structure is comparable with the size of a molecule, implying a change in the break-up process.

Recent molecular dynamics [56] simulations showed that in vacuum nanojets [55] and nanobridges [92, 91] with a diameter of 6 nm had different break-up dynamics and geometric shapes from those of macroscopic liquid structures. Instead of the unsymmetrical long-thread break-up geometric profiles [95, 29, 45, 15, 16] in macroscopic liquid structures, nanojets and nanobridges had symmetrical double-cone break-up profiles [55, 92, 91, 18, 96]. These changes were described very well by thermal fluctuations through a set of newly devised stochastic lubrication equations [55]. Further analysis of the stochastic lubrication equations revealed that the dynamics of

the break-up process of nanojets also changed [18]. The pinching of a nanojet or a nanobridge was accelerated according to a power law as $h_{min}(t) \sim (t_0 - t)^{0.418}$ [92, 91, 18] in contrast to the linear pinching of $h_{min}(t) \sim (t_0 - t)$ [15, 16] for a macroscopic jet or bridge. Here, $t_0$ was the pinching time and $h_{min}$ was the minimum radius neck of the liquid structure. It was quite a surprise to observe that the power law pinching was valid on a length scale as small as several molecules.

There are still, nevertheless, two unsettled problems. First of all, since the initial diameter of the nanobridge or nanojet is only 6 nm in the previous studies [55, 92, 91] and the corresponding pinching time is in the order of 1 ns, only the double-cone break-up profile and the dynamics of the final stage of the pinching were studied. There is a possibility that for a nanojet or nanobridge in such short pinching time the initial configurations, including the initial shape and the initial velocity distribution of the nanojet or the nanobridge, may have a lasting influence [69], and consequently, the double-cone break-up profile would not be a universal result. Secondly, all the theoretical works in the previous studies of nanojets and nanobridges [55, 92, 91, 18] were based on the stochastic lubrication equations, which are one-dimensional approximations [62, 17] to the general Navier-Stokes equations with thermal fluctuations [48]. At the nanoscale, it is necessary to examine how well the lubrication approximation works and to what extent the approximation can give accurate predictions.

To resolve the above problems, we still resort to the molecular dynamics simulation method. In this chapter, we simulate the entire pinching process of a very large liquid propane nanobridge in vacuum with a diameter of 24 nm and a length of 120 nm. Since the diameter of the nanobridge in our simulations is 4 times of that in the previous studies [92, 91], the influence of the initial configurations is safely eliminated and the transition from the long-thread break-up profile to the double-cone break-up profile is clearly displayed. Our simulation data also reproduce the power-law pinching of the nanobridge revealed in the previous studies [55, 92, 91, 18, 96], which confirms the

universality of the pinching dynamics with a double-cone break-up profile. The large size of the nanobridge also enables us to measure the velocity field of the nanobridge. By measuring the velocity field and comparing it with the result from the lubrication approximation, the validity of the lubrication approximation in the nanoscale liquid structures and the accuracy of the prediction provided by the approximation are examined.

## *5.1 Molecular dynamics simulation of a large nanobridge*

To compare the simulation results with the previous results [55, 92, 91], we still use propane molecules to construct the large nanobridge. The modeling of a propane molecule and the interaction potential are the same as in Ref. [55, 92, 91] and have been discussed in details in section 2.2. The geometric shape of the nanobridge is similar to that in chapter 4 and Ref. [91] except that the size is 4 times the previous one, i.e., the diameter of the nanobridge in this chapter is 24 nm, the length is 120 nm, and the length of the cubic calculation cell is 120 nm, as shown in Fig. 7. Note that the length-to-diameter ratio is kept unchanged in our simulations.

Since the molecular dynamics simulation deals with over $1.3\times10^6$ particles, it requires a specially designed program to carry out the simulation efficiently. Two methods are used to reduce the total computational time of each molcular dynamics integration step. First, propane molecules are grouped into cubic bins with a length of 1 nm according to their positions [56]. Since the size of the cubes is slightly larger than the cut-off radius in the Lennard-Jones force calculation, it saves a lot of time in the search of molecule pairs within the cutoff radius. Second, a force decomposition parallel algorithm [70] is used, which decreases communications between processors significantly. The entire pinching process of the large nanobridge is about 5.8 ns, (see Fig. 7(f)). It amounts to about 1.16 million integration iterations with a time step of 5 fs, and takes 31.1 thousand CPU hours on an Intel Xeon cluster (972×32 CPU

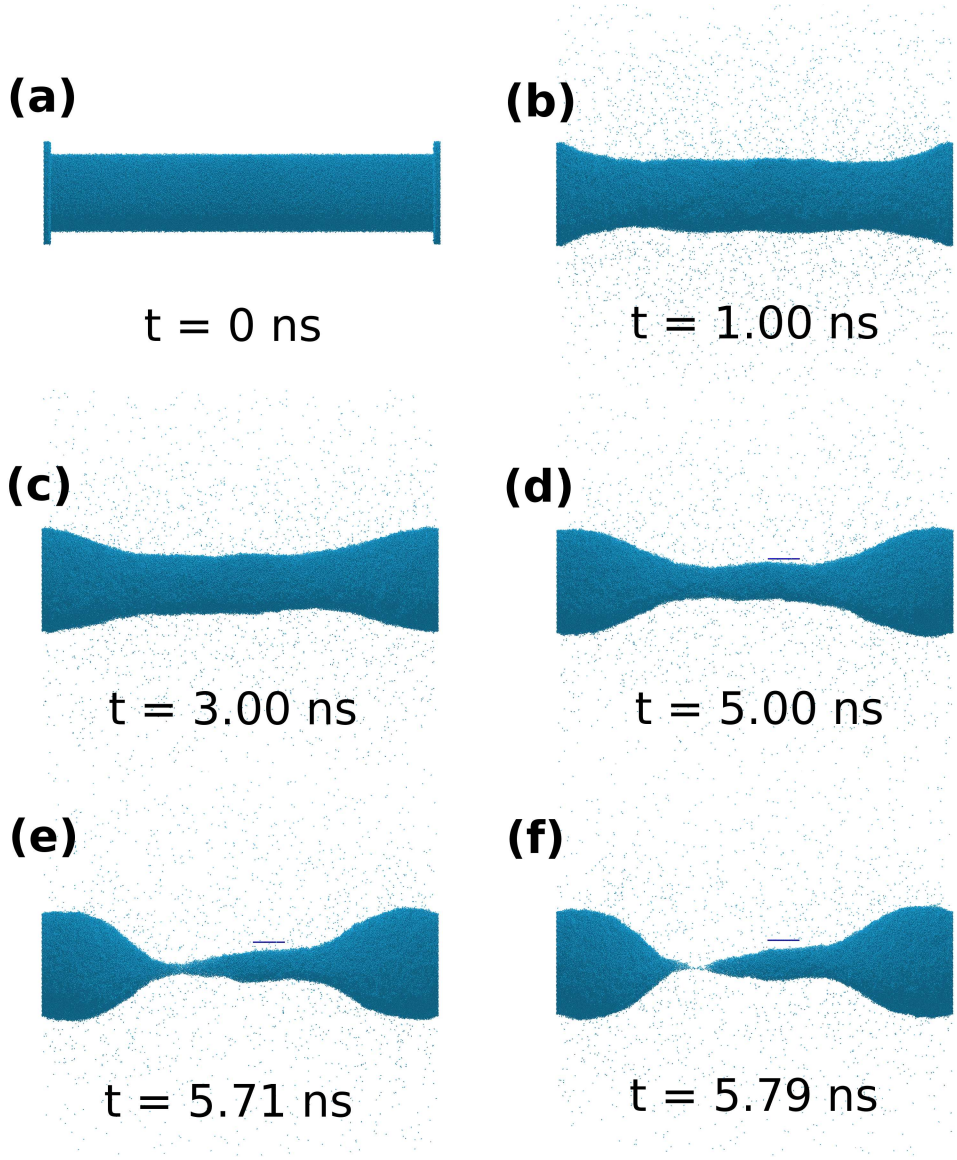


**Figure 7:** Snapshots taken from the molecular dynamics simulation of a large liquid propane nanobridge in vacuum. The length of the bridge is 120 nm and the initial diameter is 24 nm. The simulation starts at 185 K. (a) The initial configuration of the nanobridge; (b-d) development of the long-thread break-up profile; (e-f) development of the double-cone break-up profile. As a length reference, the horizontal line represents a length of 10 nm.

hours).

To obtain the shape profile (the boundary envelope) of the large nanobridge, we employ the method used in the previous studies (see chapter 4 and Ref. [91] for detailed information) with a minor modification. The method is composed of three steps. First, the nanobridge is divided uniformly into 240 bins along its longitudinal axis. Each bin has a dimension of 0.5 nm×120 nm×120 nm. Then, the center of the liquid structure in each bin is calculated as the origin of the radial distribution of the density. In the previous studies [92, 91], we just calculated the center of mass of the propane molecules in each bin as the center of the liquid structure in that bin. However, since the volume of each bin is increased to 16 times, the number of propane molecules in the vapor phase is approximately 16 times of that in the previous studies [55, 92, 91]. This causes a large drift in determining the center of the liquid structure when the diameter of the liquid part in the bin is several nanometers or smaller. This problem is solved by excluding most of the propane molecules in the vapor phase. When the diameter of the nanobridge in a bin is smaller than 10 nm, we use the formula $h_{min}(t) \sim (t_0 - t)^{0.418}$ [55, 92, 91, 18, 96] to estimate its minimum radius and calculate the center of mass in a cylinder with a radius of $h_{min} + 3$ nm at the center of the bin as the origin of the radial distribution of the density. With the determined center, we translate the positions of propane molecules, obtained directly from the molecular dynamics simulation at a particular time, into the radial distribution of density with a radial increment of 0.2 nm and place the surface of the liquid structure at the radius where the density of propane molecules drops to about 1/6 of the density at the center of the nanobridge ($0.09\times10^3$ kg/m$^3$ [91]) . Note that the radial increment and the cut-off criterion of the density are the same as those used in the previous studies [55, 92, 91].

The transition from a long-thread break-up profile to a double-cone break-up profile is displayed clearly in Fig. 7, where (b-d) show the formation of a long-thread

breakup profile and (e-f) show the formation of a double-cone profile at one side of the long thread. It provides the picture for the break-up process of a viscous flow within the length scale of 20 nm, and reveals the fate of the cascade of long-thread break-up structures in a viscous flow. With this information, the entire picture of the break-up process can be described as following. First, when the characteristic size of the flow is much larger than the thermal length scale [55, 92, 91], the break-up process is dominated by deterministic factors and the break-up profile is a cascade of long threads [95, 29]. However, when the size of the flow is comparable to the thermal length scale, the cascade ends with a double-cone breakup profile under the influence of thermal fluctuations.

## *5.2 The size-dependent influence of thermal fluctuations*

Without thermal fluctuations, the memory of the initial configuration persists for a long time before the pinching dynamics of a liquid bridge reaches its linear stage, which is described by the formula $h_{min}(t) \sim (t_0 - t)$ [15, 16]. As displayed in Fig. 8, the best fit (solid line) of the simulation data (hollow square curves) gives a power law index of 1.1, which is in reasonable accordance with the theoretical prediction. Numerical simulations of the lubrication equations (LE), in which thermal fluctuations are absent, for axisymmetric liquid structures show that the memory of initial configurations emerges regardless of the boundary conditions of the liquid structure. In the simulation of the pinching process of a nanoscale liquid structure by means of the lubrication equations, the transition stage occupies most of the pinching time. For example, numerical LE simulations of a liquid bridge with an initial diameter of 24 nm and a length of 120 nm show that its entire pinching time is 12.732 ns and the linear stage begins at about 100 ps before the breakup occurs, with a minimum diameter of about 0.2 nm (see the square curves and the fitted linear curve in Fig. 8). Note that 0.2 nm is slightly longer than the length of a carbon-carbon single bond (0.154

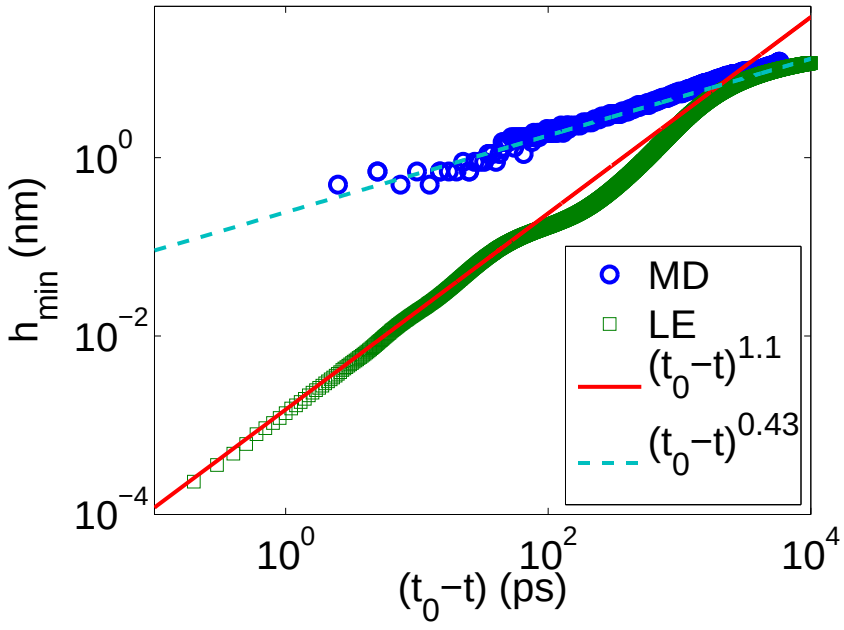


**Figure 8:** Time dependence of the minimum radius $h_{min}$ of a nanobridge with a diameter of 24 nm and a length of 120 nm. The hollow-circle curve is obtained from molecular dynamics simulations, and the dashed line is the best-fitting curve of $h_{min}$ as the nanobridge approaches its pinching point, which yields a power exponent of 0.43 and agrees well with the theoretical prediction based on the stochastic lubrication equations. The hollow-square curve, which is obtained from the numerical integration of the lubrication equations (no thermal noise), is nearly linear. Its best-fitting curve (solid line) gives a power index of 1.1, following well with the prediction of a linear deterministic pinching.

nm) in propane molecules. It implies that, practically, we are not able to observe the scaling behavior in a liquid nanobridge if the memory of initial configurations can last so long according to the prediction of lubrication equations.

Molecular dynamics simulations of a nanobridge with the same size show that thermal fluctuations have a prevailing influence on the pinching dynamics. It not only accelerates the pinching process, but also shortens the time that the liquid nanobridge spends in the transition stage. As presented by the hollow-circle curve in Fig. 8, the minimum neck $h_{min}(t)$ of the nanobridge decreases according to a power law when it approaches the break-up point. Fitting the data of $h_{min}(t)$ in the last 660 ps of the pinching process, during which $h_{min}$ decreases from about 4 nm to 0, gives a

power law index of 0.43. This result agrees well with both the theoretical prediction [55, 18] and our previous measurement for a smaller nanobridge [92, 91]. It shows that the power law pinching of a nanobridge is not the result of initial conditions, and the influence of the initial configurations has disappeared long before the minimum diameter reaches the size of a propane molecule.

To illustrate the effect of thermal fluctuations in erasing the memory of the initial configuration, we put together (by shifting the LE curve) the time dependence curves of the minimum neck $h_{min}(t)$ obtained from the molecular dynamics simulation and from the numerical simulation of the lubrication equations, in such a way that regions just preceding the final pinchoff have as much overlap as possible (see Fig. 9). The pinching process of the liquid propane nanobridge (the result of the molecular dynamics simulation) is divided into three stages, as displayed in Fig. 9. In the first stage, the nanobridge recovers from the artificial effects of the liquid propane cylinder newly cut from a bulk of liquid propane. In the second stage, the pinching process of the nanobridge overlaps with the pinching curve provided by the lubrication equations, i.e., they have similar $h_{min}$ and $\dot{h}_{min}$. This suggests that at each moment of this second stage, the nanobridge described by the lubrication equations has approximately the same dynamics and configurations as in the molecular dynamics simulations at the vicinity of where the instantaneous minimum radius of the nanobridge emerges. In the third stage, the neck of the nanobridge pinches off according to the power law (see the dashed curve in Fig. 8), while the numerical simulation of the lubrication equations shows that the neck pinches with a much slower speed.

To see how thermal fluctuations alter the pinching process clearly, let us start with the second stage. Suppose the nanobridge is released at some moment in the second stage. As aforementioned, the pinching process described by the lubrication equations of the same initial configurations follows the break-up process of the real nanobridge (simulated by the molecular dynamics method) for a while. In this stage,

deterministic factors have a dominant effect. However, in the third stage, the thermal fluctuations speed up the pinching process. As displayed in Fig. 9, the diameter of the nanobridge decreases from about 20 nm to nearly 14 nm in 3 ns in the second stage, while in the third stage, it takes only half of that time for the nanobridge's diameter to decease form 14 nm to 0. We can also see from the figure that the pinching process of the nanobridge, which is simulated by molecular dynamics method, apparently departs from the process predicted by lubrication equations. This suggests that at the beginning of the third stage, the memory of the initial conditions has almost been erased by thermal fluctuations.

## *5.3 Lubrication approximation in a nanobridge*

Lubrication approximation [62, 17, 75, 76] is one of the important methods used in the theoretical study of liquid nanojets and nanobridges [55, 92, 91, 18]. It reduces the three-dimensional Navier-Stokes equations to a set of one-dimensional equations of motion along the longitudinal direction (the z direction) of the liquid structure. Generally, the lubrication approximation implies that the velocity fields ($vr(z,r,t)$ and $vz(z,r,t)$) are expanded as series of the radial positions (r) to the lowest-order terms and the expansion coefficients are used to form the simplified one-dimensional equations of motion (in this case, the stochastic lubrication equations). For a liquid jet or bridge, it has been shown that the lowest-order expansions of the velocity fields are [17]

$$\begin{cases} v_z = v_0(z,t), \\ v_r = -\frac{r}{2}v_0'(z,t), \end{cases} \tag{5.1}$$

where $v_0(z,t)$ and its derivative $v_0'(z,t)$ with respect to z are used to form the one dimensional stochastic lubrication equations or lubrication equations. Eq. (5.1) provides two approaches to measure the value of $v_0'(z,t)$. In the first approach, $v_0'(z,t)$ is obtained by measuring the derivative of $v_z$ using the second order finite-difference

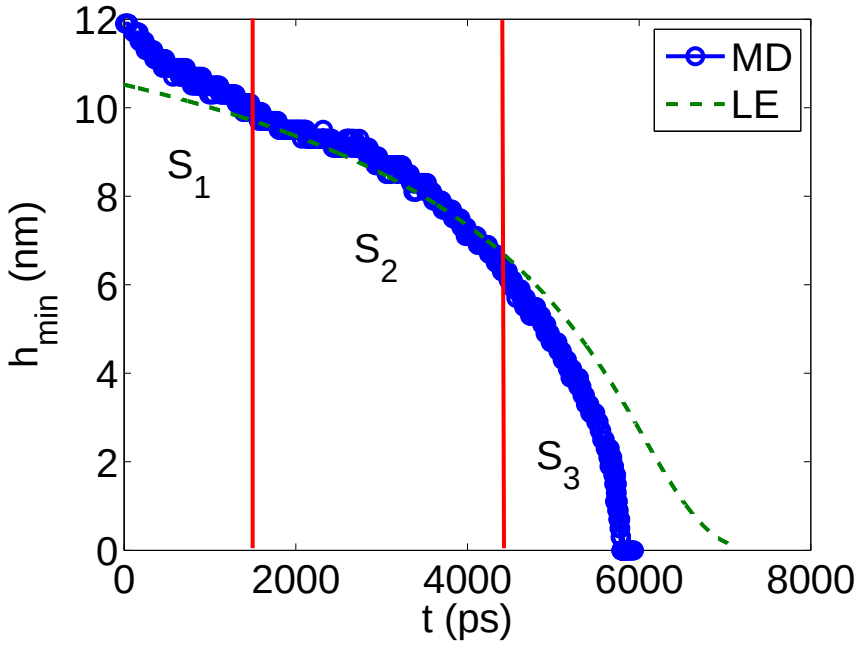


**Figure 9:** The comparison of the pinching process of a deterministic liquid bridge and a liquid nanobridge. The pinching curve of the nanobridge (solid curve with open symbols) is obtained from the molecular dynamics (MD) simulation of a propane nanobridge of diameter 24 nm and of length 120 nm; and the deterministic pinching curve (dashed curve) is taken from the numerical integration of the lubrication equations (LE) of a liquid bridge with the same size. In both cases the temperature is 185 K. For the integration of LE, we adopt the same surface tension and viscosity value as used in Ref. [92, 91]. The entire pinching process is divided into three stages, denoted as S1, S2 and S3. The two pinching curves are put together with maximum overlap in the second stage (S2). In the third stage, the pinching process speeds up and the memory of the initial configurations is lost.

method, where $v_z$ is the average longitudinal velocity on the entire cross-sections perpendicular to the $z$ axis. In the second approach, $v_0(z,t)$ is obtained by fitting $v_r(z,r,t)$ as a function of $r$. By comparing $v_0'$ obtained by both methods, we can see how well the lubrication approximation works for a liquid nanobridge.

In our previous studies [92, 91], the diameter of the liquid nanobridge was only 6 nm. It was too small to extract the velocity field from the trajectories of the propane molecules in a molecular dynamics simulation because of the large thermal fluctuations. Now, with a liquid nanobridge 4 times of the size, we can determine the velocity field of the nanobridge more accurately, and in turn verify the validity

of the lubrication approximation used in the stochastic lubrication equations (or in the lubrication equations). In Fig. 10, we show the velocity field of the nanobridge on a 30×9 cylindrically symmetrical grid at t = 4.5 ns. The entire computational volume is divided along the longitudinal direction of the nanobridge into 30 bins of 4 nm thickness, and each bin is in turn divided into 9 annular rings of width 0.8 nm. The velocity field at each grid point is the average velocity of the propane molecules in the annular ring. The figure shows that the velocity field of the nanobridge is longitudinally oriented as a whole with the maximum velocity occurring near z = ±30 nm. To compare the $v_0'$ obtained through both $v_z$ and $v_r$ in Eq. (5.1), we look up four cross-sections A, B, C, and D of the nanobridge, as indicated in Fig. 10, having representative velocity fields. A and B are adjacent with a modest velocity field; the velocity field on C is very small; and on the cross-section D, the velocity field is near the maximum value. In Table 5, we list the measurement of $v_0'$ of these four cross-sections obtained by fitting both $v_z$ and $v_r$ via Eq. (5.1). The $v_0'$'s obtained using both methods agree very well. This suggests that the lubrication approximation works well at the nanoscale. Note that on the cross-section D, the difference between the $v_0'$'s obtained by the two methods are slightly larger than the errors. This deviation is due to the fact that the cross-section lies near the maximum, where the finite difference method would not be expected to give a good estimate to the derivative of $v(z)$.

The expansion of $v_z$ and $v_r$ in Eq. (5.1) can be derived in several ways [62, 17]. Some of the derivations assume that $v_z$ is much larger than $v_r$ [62, 17]. In that case, the entire velocity fields are along the longitudinal direction. This assumption is often called the slenderness assumption [17]. However, as shown in the upper panel of Fig. 10, the velocity fields at the surface of the nanobridge are parallel to the surface. In the places where the surface has a large slope, the magnitudes of $v_r$ and $v_z$ are comparable. This implies that the application of the lubrication approximation does not require the slenderness assumption valid everywhere in the liquid structure.

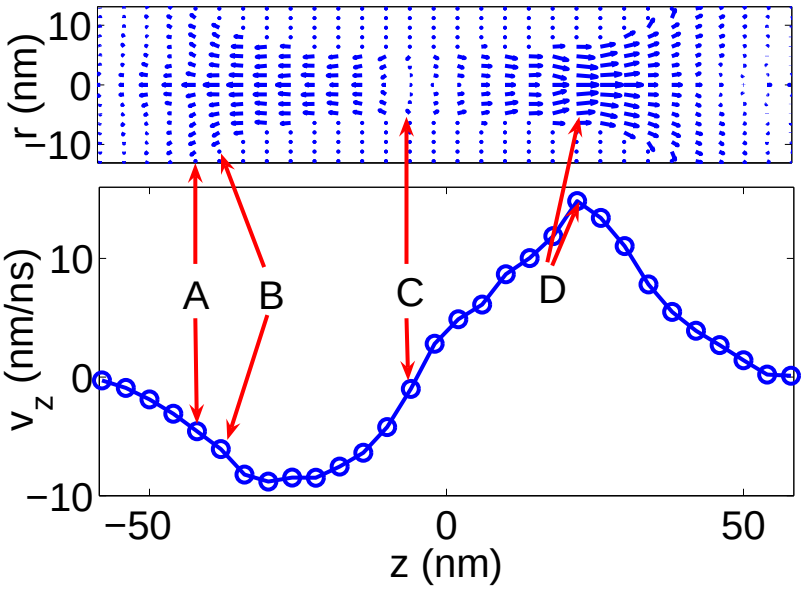


**Figure 10:** The velocity field of the nanobridge on a 30×9 cylindrically symmetrical grid. The distance between two horizontal grid points is 4 nm. The upper panel shows the velocity vector field at t = 4.5 ns and the lower panel shows the averaged longitudinal velocity field ($v_z$). A, B, C, and D indicated in the figure are where we evaluate the derivatives of $v_0$ (see Eq. (5.1) for detailed information). The measurements are shown in Table 5.

Indeed, we can apply Eq. (5.1) to a liquid structure whose motion is basically along the longitudinal axis.

## *5.4 Discussion*

In this chapter, we discuss the dynamical behavior during the final stage of the break-up process of a liquid nanobridge; and in particular, focus on the influence of thermal fluctuations. We find that thermal fluctuations quickly erase the influence of initial configurations, which ensure the universality of the double-cone break-up profile caused by thermal fluctuations during the final stage. The transition from the long-thread break-up profile to the double-cone break-up profile is also observed, which provides complete information for the fate of the cascade of long-thread break-up profile in a viscous flow.

**Table 5:** The measurement of the derivative of $v_0$ in Eq. (5.1). The cross-sections are indicated in Fig. 10 and the distance between two adjacent cross-sections is 4 nm. In the table, $v_0^{'1}$ is obtained by measuring the derivative of the average $v_z$ on the cross-sections using a finite difference method and $v_0^{'2}$ is measured by fitting $v_r$ on each cross-section as a linear function of $r$. The results show that the lubrication approximation works well at the nanoscale. Note that the deviation in the measurement on cross-section D is due to the inaccuracy of the finite difference method near maximum points.

| Intersection | $v_z$ (nm/ns) | $v_0^{'1}$ ($\text{ns}^{-1}$) | $v_0^{'2}$ ($\text{ns}^{-1}$) |
|---|---|---|---|
| (A-1) | -3.6±0.3 | - | - |
| A | -5.3±0.4 | -0.46±0.07 | -0.52±0.06 |
| B | -7.3±0.5 | -0.59±0.07 | -0.57±0.04 |
| (B+1) | -10.0±0.4 | - | - |
| (C-1) | -3.3±0.3 | - | - |
| C | -0.2±0.4 | 0.63±0.08 | 0.74±0.09 |
| (C+1) | 1.7±0.5 | - | - |
| (D-1) | 11.6±0.6 | - | - |
| D | 15.9±0.4 | 0.45±0.09 | 0.63±0.11 |
| (D+1) | 15.1±0.6 | - | - |

We also discuss the validity of the lubrication approximation used in the stochastic lubrication equations. The molecular dynamics simulation of a nanobridge shows that the lubrication approximation works well at the nanoscale. It also shows that while the lubrication approximation can be derived from the so-called slenderness assumption, it can go beyond the assumption. For a liquid structure with a undulating free surface (for example, a liquid jet or bridge) the lubrication approximation still works well as long as the motion of the liquid structure is primarily longitudinal.

# CHAPTER VI

# THE INSTABILITY OF A NANOBRIDGE

The instability of a liquid structure with a free surface is one of the important problems of hydrodynamics. It is common in life and has fundamental impacts on the modern industrial society [50, 17]. A simple vesion of this problem is the well-known Rayleigh instability [73, 62] of a cylindrical liquid column with a uniform diameter; which, though simple, catches most of the essential features of the instability problem. Nowadays, as the dimension of the liquid structure in applications is shrinking fast, microscopic hydrodynamics has attracted more and more attention; however, our knowledge of nanoscale instabilities is still very limited. One possible reason of this is that traditional experimental methods are not able to provide enough spatial and temporal resolution simultaneously. Recent progress [40, 39, 33, 55] has been achieved mainly through large scale computational methods, and it seems this trend will last for a while.

Here we concentrate our attention to the problem of the linear instability of a nanobridge, which is the nanoscale analogue of the macroscopic Rayleigh instability [73] problem. For a macroscopic liquid bridge, the Rayleigh instability triggers the break-up process, and the wavelength of the fastest growing perturbation mode determines the size of the major droplets after the breakup. A lot of applications of free-surface flow, such as inkjet printing, spraying, and fuel injecting [93, 3, 85], are based on this mechanism. Similarly, if we want to design and use nanofludic devices [2] from which a nanoscale free-surface flow is produced, the nanoscale instability should be understood first. However, recent studies [55, 18, 92] showed that the nanoscale instability may not be a simple extrapolation of the macroscopic Rayleigh instability

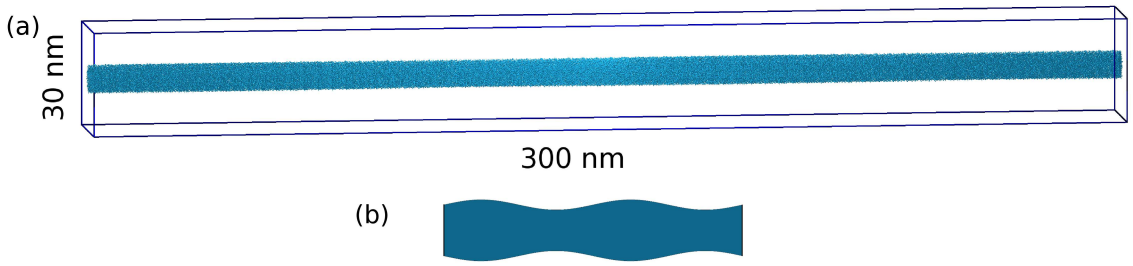


**Figure 11:** (a) The initial configuration with a radial perturbation of the form $r_0 = D/2 + h_0 sin(kz)$ on the surface of a long nanobridge, which is used in the molecular dynamics simulations to measure the growth rates and structure functions of the perturbation. As a example, we show here the case of $k = 2$. The average diameter D of the long nanobridge is 6 nm $\sim$ 8 nm and the amplitude $h_0$ of the perturbation is 0.1 nm in the simulations. The outer prism is the calculation cell which has a dimension of 30 nm $\times$ 30 nm $\times$ 0.3 $\mu$m. (b) The enlarged shape of the perturbation which is not perceivable in (a). Note that to measure the structure function, the radius profile of the surface is $r_0 = D/2$, and the perturbations are the result of thermal fluctuations.

because of the dominant influence of thermal fluctuations at the nanoscale.

Recently, this problem was addressed using molecular dynamics simulation methods [44, 42, 33, 55] for both nanobridges and nanojets. Though they have shown that a nanoscale free-surface flow is unstable when its length is much larger than its diameter, quantitative measurements, such as the growth rate dispersion curve and the criterion for the occurrence of the instability, have not be done yet due to strong fluctuations encountered in the simulations. Now, with the development of computational techniques, the strong thermal fluctuations can be dealt with by large ensemble average, which makes quantitative measurements possible.

In this chapter, the instability of sinusoidal perturbation modes on the surface of a long liquid propane nanobridge at a temperature of 185 K is studied using large scale molecular dynamics simulation methods. The growth rate dispersion relation is measured by analyzing the time evolution of the sinusoidal perturbations of various wavelengths, and the unstable criterion is measured by determining the shortest wavelength of the unstable sinusoidal perturbation. Comparison of the measurements

of the growth rate dispersion relation with the results from instability theories (both Rayleigh's instability theory for inviscid flow and Chandrasekhar's theory for viscous flow) [73, 9, 17] shows that viscosity plays an important role at the nanoscale instability and that the instability of a nanobridge emerges first in the interfacial surface layer. Also, to describe the effect of thermal fluctuations, the time evolution of the structure function of the nanobridge is analyzed. The result shows that thermal fluctuations triggers and sustains structure pattern of large wavenumber. This explains why the surface of a nanobridge always looks rough.

## *6.1 The simulation of a very long nanobridge*

In the molecular dynamics simulations, a velocity Verlet algorithm [56] with modification to implement Brownian dynamics [56] is employed. The long liquid nanobridge is composed of propane molecules ($C_3H_8$) as in our earlier studies. Detailed information of the method and the modeling of propane molecules can be found in chapter 2 and in Ref. [55]. Note that to accelerate the simulation process, the C-C bond between $CH_2$'s and $CH_3$'s is modeled as a soft spring with a force constant 112 J/m$^2$, so that a time step as large as 5 fs can be used.

The length (L) of the propane nanobridge is 0.3 $\mu$m and its average diameter (D) varies from 6 to 8 nm. The long length of the nanobridge results in a large particle number up to about 340, 000. The entire nanobridge is placed at the center of a right prism with a dimension of 30 nm $\times$ 30 nm $\times$ 0.3 $\mu$m, as displayed in Fig. 11. In the direction parallel to the long side of the right prism, which is called the z direction hereafter, periodic boundary conditions are used to eliminate artifacts caused by boundaries. In the other two directions, propane molecules are removed from the system when they escape from the prism. The initial surface profile of a nanobridge with an azimuthal symmetrical sinusoidal perturbation can be depicted

completely by its initial radius ($r_0$), which has a form of

$$r_0 = \frac{D}{2} + h_0 \sin(kz), \tag{6.1}$$

where $h_0$ is the amplitude of the perturbation, and $k$ is its wavenumber. In the simulation, $h_0$ is always 0.1 nm and $k$ is integral multiples of $\frac{2\pi}{L}$ as the result of periodic boundary conditions. Especially, the uniform initial radius profile (the corresponding wavenumber $k$ is zero) is used to measure the structure function of perturbations on the surface of a nanobridge, while other profiles with $k \neq 0$ are used to measure the growth rate dispersion relation.

With perturbations on the surface, the initial configuration of the nanobridge has to be prepared very carefully. To make sure that the liquid propane in the nanobridge is in the local statistical equilibrium at 185 K, the following procedure is employed. First, 500 propane molecules are thermalized to 185 K for sufficiently long time (over 10 ns) in a cubic box of edge length 4.0524 nm, and periodic boundary conditions are applied in all directions. The edge length of the box is incommensurate to the length of the nanobridge, which is 0.3 $\mu$m, and it is smaller than any of the wavelength we are interested in. This prevents any possible interference of the periodicity of the box with the instability of the nanobridge. Then, a right prism, in which the entire nanobridge can be enveloped, is constructed by repeating the box of propane molecules in the space periodically. From the right prism a nanobridge can be cut out according to Eq. (6.1). Also, at the beginning of each simulation, the entire nanobridge is thermalized at 185 K using the Brownian dynamics method [56] for the first 20 ps. This thermalization period is long enough to allow the nanobridge to form an interfacial surface layer, which was discussed in the previous simulations [42, 33], but short enough that no significant morphological change occurs.

## 6.2 Measuring the growth rate and the structure function

Suppose a perturbation $\delta(z,t)$ on the surface of a nanobridge grows or decays exponentially as

$$\delta(z,t) = \delta(z,0)\exp(\sigma t), \tag{6.2}$$

then $\sigma$ is called the growth rate of the perturbation [51]. In the molecular dynamics simulations, the perturbation $\delta(z,0) = h_0 \sin(kz)$ is part of the initial surface profile (see Eq. (6.1)).

The procedure measuring the growth rate of a perturbation on the surface of a nanobridge is composed of two steps. In the first step, the radius profiles $r(z,t)$ of the nanobridge at successive moments are extracted from the trajectories of the propane molecules obtained from the molecular dynamics simulation. In the second step, $r(z,t)$ are decomposed into amplitudes of sinusoidal perturbation modes of various wavenumbers and the results are called the spatial spectrum of $r(z,t)$, denoted as $h(k,t)$. For each wavenumber $k$, the growth rate of the amplitude $h(k,t)$ is measured and it is usually called the growth rate dispersion relation.

To extract the radius profile $r(z,t)$, the nanobridge is divided into N bins along the z axis. Each bin is labeled by an index $n = 0, 1, \ldots, N-1$, and its coordinate is $z_n = nL/N + L/(2N)$. To obtain enough resolution of the radius profile, we take $N = 600$ and the thickness ($\Delta$) of each bin is 0.5 nm. Then, the radial density histogram of propane molecules in each bin is calculated with radial increments of 0.2 nm. Note that the origin point of the histogram is the center of mass of that bin. Since there is an interfacial surface layer between the bulk of the liquid propane nanobridge and the vacuum [42, 33], we define the local radius of the nanobridge, $r(z_n,t)$, in each bin as where the density of propane molecules decreases to about $0.166 \times 10^3$ kg/m$^3$. To further reduce the fluctuation of a single measurement, the average value of $r(z_n,t)$ over 1 ps is taken as the final result. The deformation of $r(z_n,t)$ due to the above procedure only affects the large wavenumber (short wavelength) part of

the spatial spectrum of $r(z_n, t)$, which is far away from the small wavenumber (long wavelength) part we are interested in. Then, $r(z_n, t)$ is decomposed into the spatial spectrum, designated as $h(k_l, t)$, using a one-dimensional discrete Fourier transform,

$$h(k_l, t) = \frac{1}{N} \sum_{n=0}^{N-1} r(z_n, t) \exp\left(-i \frac{2\pi n l}{N}\right), \tag{6.3}$$

where $l = 0, 1, \ldots, N-1$ denotes discrete wave numbers, $k_l = \frac{2\pi l}{L}$, and $i$ is the imaginary unit.

For a macroscopic liquid bridge of diameter D, linear instability analysis [17] shows that the unstable perturbations on its surface concentrate in the small wavenumber (long wavelength) part, and the largest wavenumber of an unstable sinusoidal mode is around $2/D$. If these results are also applied to a nanobridge, a modest resolution in the unstable wavenumber region, say 15 wavenumber points in that region, requires a ratio of length (L) to diameter (D) as large as $15\pi$. To achieve this resolution, for a nanobridge with diameters in the range of 6 - 8 nm, the length of the nanobridge has to be 0.28 $\mu$m - 0.38 $\mu$m at least. In the molecular dynamics simulation, for simplicity, we fix the length of the nanobridge to be 0.3 $\mu$m. The very long length of the nanobridge results in a large particle number about 340, 000.

In order to smooth out fluctuations in the spatial spectrum $h(k_l, t)$, for each initial surface profile given by Eq. (6.1) with a particular $k_l$, a large ensemble consisting of 400 independent simulations of the nanobridge is used. (The large ensemble and large particle number in the system together make the MD simulation very costly. It takes about $7.2 \times 10^3$ CPU hours, or 400×18 CPU hours, on an AMD Opteron cluster to calculate the growth rate value of each $k_l$.) Then, according to the linear instability theory (Eq. (6.1)), the amplitude of the perturbation of wave number $k_l$ is fitted with the exponential function $h(k_l, t) = h_{l,0} \exp(\sigma t)$, where $h_{l,0}$ is the initial amplitude of the perturbation, which is a fixed real number in the ensemble average.

The structure function $S(k, t)$ of the perturbation is defined using the spatial

spectrum $h(k,t)$ as

$$S(k,t) = \langle h(k,t)h(-k,t)\rangle = \langle h(k,t)h^*(k,t)\rangle\,, \tag{6.4}$$

where, $h^*(k,t)$ is the complex conjugate of $h(k,t)$ and the last equality in Eq. (6.4) is the result of $r(z,t) = r^*(z,t)$. The structure function is also the Fourier transform of the spatial correlation function $G(z,t)$, which is defined as,

$$G(z,t) = \frac{1}{L^2}\int_L \langle r(z+z',t)r(z',t)\rangle\, dz'. \tag{6.5}$$

The structure function $S(k,t)$ provides quantitative spatial structure information during the break-up process of a nanobridge.

The procedure of measuring the structure function also has two steps. The first step is the same as the first step of measuring the growth rate of a nanobridge. However, in the measurement of the structure function, there is no perturbation set manually in the initial surface profile, i.e., in Eq. (6.1) the amplitude of a perturbation $h_0$ is equal to zero. All the perturbations come from thermal fluctuations of the nanobridge. In the second step, the spatial spectrum $h(k_l,t)$ is obtained using the same method as used in measuring the growth rate dispersion relation. Then, $\langle h(k_l,t)h^*(k_l,t)\rangle$ is calculated for each wavenumber $k_l$ over an ensemble of 400 independent nanobridges.

## *6.3 Theoretical analysis of the growth rate dispersion*

Theoretically, we can obtain the growth rate dispersion curve from the linear instability analysis based on the stochastic lubrication equations [55], which is very successful in describing the pinching process of a nanoscale axisymmetric flow. Unlike the linear instability analysis of a deterministic system, the linear instability analysis of a nanobridge (based on the stochastic lubrication equations) is performed in a statistical average manner. The result of it is a set of linearized averaged stochastic lubrication equations, which have the same form as the linearized lubrication equations. Plugging

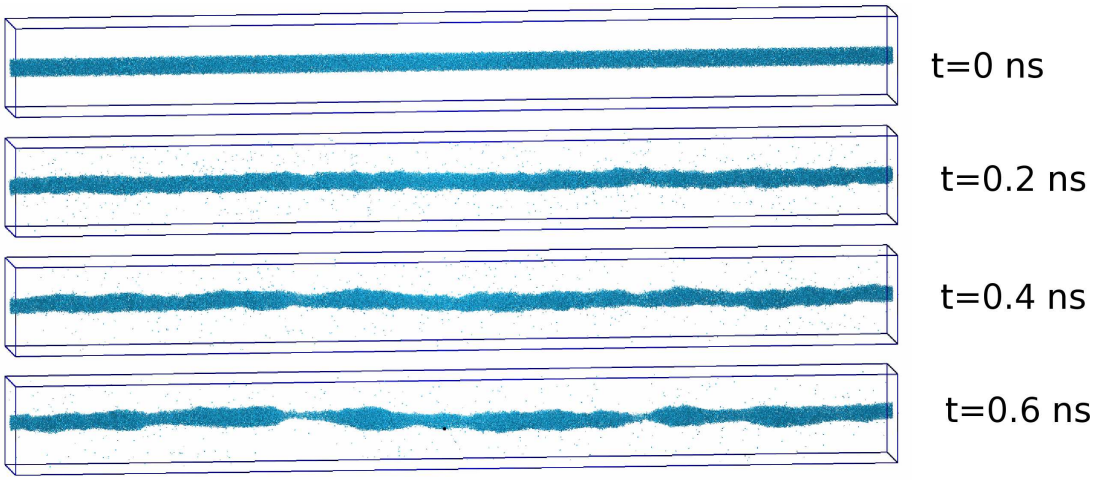


**Figure 12:** Selected configurations from a typical break-up process of a propane nanobridge of diameter 6 nm and length 0.3 $\mu$m at 185 K. The snapshots are taken at t = 0, 200 ps, 400 ps and 600 ps. The prism frames with a dimension of 30 nm $\times$ 30 nm $\times$ 300 nm in the figures are the calculation cells. The break-up profile of a long nanobridge consists of irregular bumps, which is different from the macroscopic profile which has uniform-sized bumps connected by long threads.

the perturbation ansatz (Eq. (6.2)) into the linearized averaged stochastic lubrication equations, we can obtain the growth rate dispersion relation.

Here, we follow the standard procedure [31] of the linear analysis of stochastic partial differential equations to obtain the linearized form of the averaged stochastic lubrication equations. Generally, for a stochastic partial differential equation (in a spatial discrete form) with multiplicative noise [31],

$$\frac{d\phi_i(t)}{dt} = f_i(\{\phi\}) + \sum_j g_{ij}(\{\phi\})\eta_j(t), \tag{6.6}$$

the averaged stochastic partial differential equation is [31],

$$\frac{d}{dt}\langle\phi_m(t)\rangle = \langle f_m(\phi)\rangle + \sum_{jkl}\left\langle (\frac{\partial g_{mj}}{\partial\phi_l})C_{jk}g_{lk}\right\rangle, \tag{6.7}$$

where,"$\langle\rangle$" refers to the ensemble average, $\phi$ is the field variable, $f$'s are the deterministic part of the stochastic partial differential equation, $\eta$'s are Gaussian noises with relations $\langle\eta_i(t)\eta_j(t')\rangle = 2C_{ij}\delta(t-t')$, and $C_{ij}$'s are their spatial correlations.

For the stochastic lubrication equations proposed in Ref. [55] (see chapter 3 for detailed information),

$$\partial_t v + vv' = -\frac{\gamma}{\rho}\kappa' + \frac{3\eta}{\rho h^2}(h^2 v')' - \frac{\sqrt{3k_B T\eta}}{\rho\sqrt{\pi}h^2}(h\Gamma)', \tag{6.8}$$

$$\partial_t h + vh' = -\frac{h^2 v'}{2}, \tag{6.9}$$

with all the symbols having the same meanings as in chapter 3, the $g$'s (the strength of the noise) are calculated as,

$$g_{v(z)v(z_1)} = -\frac{\sqrt{3k_B T\eta}}{\rho\sqrt{\pi}h(z)^2}\partial_z(h(z)\delta(z-z_1)) \tag{6.10}$$

$$g_{vh} = g_{hv} = g_{hh} = 0. \tag{6.11}$$

Considering $g_{v(z)v(z_1)}$ is the only nonzero term, the entire contribution of the noise to the averaged equations is

$$\int dz_1 dz_2 dz_3 \left\langle \left(\frac{\partial g_{v(z)v(z_1)}}{\partial h(z_2)}\right) C_{v(z_1)v(z_3)} g_{h(z_2)v(z_3)} \right\rangle, \tag{6.12}$$

which is zero because $g_{v(z)v(z_1)}$ is not a function of $h(z_2)$. This result suggests that in the average meaning, the noise does not have any contribution to the averaged stochastic lubrication equations.

Usually, the average of the the deterministic terms $\langle f_m(\{\phi\})\rangle$ in Eq. (6.6) are not equal to $f_m(\langle\{\phi\}\rangle)$ [31]; however, if we just consider the linear approximation of the stochastic partial differential equation around $\{\phi\} = \{\phi_0\}$, the approximations of the two functions $\langle f_m(\{\phi\})\rangle$ and $f_m(\langle\{\phi\}\rangle)$ are equal to each other (to the first order of $\{\phi\}$). Suppose $h = D/2 + \epsilon h_1$ and $v = \epsilon v_1$, and employ the above argument, the linearized form of the averaged stochastic lubrication equations are obtained as,

$$\partial_t v_1 = \frac{4\gamma}{\rho}\frac{h_1'}{D^2} + \frac{\gamma}{\rho}h_1''' + 3\frac{\eta}{\rho}v_1'', \tag{6.13}$$

$$\partial_t h_1 = -\frac{D}{4}v_1', \tag{6.14}$$

where, all the "$\langle\ \rangle$" symbols are dropped. They have the same form as the linearized lubrication equations. Now, suppose

$$\begin{cases} v_1 = \bar{v}e^{-\sigma t+ikz} \\ h_1 = \bar{h}e^{-\sigma t+ikz} \end{cases} \tag{6.15}$$

with $i$ the imaginary unit, the linearized averaged stochastic lubrication equations (6.13) and (6.14) are transformed as,

$$\begin{aligned} -\sigma\bar{v} &= i\frac{4\gamma}{\rho}\frac{k\bar{h}}{D^2} - i\frac{\gamma}{\rho}k^3\bar{h} - 3\frac{\eta}{\rho}k^2\bar{v}, \\ -\sigma\bar{h} &= -\bar{v}. \end{aligned} \tag{6.16}$$

The secular equation of Eq. (6.16) is

$$\begin{vmatrix} 3\frac{\eta}{\rho}k^2 - \sigma & -i\frac{4\gamma}{\rho}\frac{k}{D^2} + i\frac{\gamma}{\rho}k^3 \\ i\frac{D}{4}k & -\sigma \end{vmatrix} = 0, \tag{6.17}$$

and the solution of the secular equation is,

$$\sigma = \sigma_0\left\{\sqrt{\frac{1}{2}x^2(1-x^2) + \frac{9}{4}Re^{-2}x^4} - \frac{3}{2}Re^{-1}x^2\right\}, \tag{6.18}$$

with

$$\sigma_0 = \sqrt{8\gamma/(\rho D^3)}, \tag{6.19}$$

and

$$Re = \sqrt{D\gamma\rho/(2\eta^2)}, \tag{6.20}$$

where $x = kD/2$, $\gamma$ is the surface tension, $\rho$ is the density and $\eta$ is the viscosity of the liquid. Eq. (6.18) is just the growth rate dispersion relation obtained from the linear instability analysis. It can also be obtained from the Chandrasekhar's instability theory in a expanded form for small wavenumbers [9, 17].

As an alternate, we also consider the Rayleigh's instability theory [73]. According to this theory, the growth rate of an inviscid long bridge is [17],

$$\sigma = \sigma_0\left[\frac{xI_1(x)}{I_0(x)}(1-x^2)\right]^{\frac{1}{2}}, \tag{6.21}$$

where $I_n(x)$'s are modified Bessel functions of the first kind.

## 6.4 Results and discussions

Before the measurement of the growth rate dispersion curves and the structure functions, several simulations were performed for the entire break-up process of long nanobridges of various initial diameters and without sinusoidal perturbations on the surfaces. In Fig. 12, we show a typical pinching process of a long nanobridge. For a nanobridge of diameters in the range of 6 nm - 8 nm, the pinchoff time varies between 0.5 ns $\sim$ 1.2 ns randomly. As shown in the fourth panel of Fig. 12, the break-up profile of a long nanobridge is composed of irregular bumps, and is also observed by Kawano in Ref. [42]. This break-up profile is essentially different from the macroscopic profiles, in which uniform bumps are connected by long threads [50].

In the simulation, to measure the growth rate dispersion curve, the trajectories of the long propane nanobridge are recorded for the first 100 ps for each break-up process. This time period is short compared with the breakup time of the nanobridge, and the perturbations on the surface of a nanobridge are still small enough in this time period, so that nonlinear effects can be neglected. The second panel of Fig. 12 shows that, even up to 200 ps, the perturbations on the surface are still small compared with the diameter of the nanobridge. To examine the validity of linear instability theory, in Fig. 13 we also show that in the first 100 ps the amplitude of the perturbations of various wavenumbers increases exponentially.

The growth rate dispersion curves of nanobridges of diameters 6 nm and 8nm are displayed in Fig. 14. Qualitatively, the shape of the growth rate curves provide a good explanation to the previous molecular dynamics simulation results of the break-up process of nanoscale flows [42, 55, 44]. For instance, the growth rate curves predict that the unstable perturbations on the surface of a nanobridge have a minimum wavelength [44], and it is reflected in the Fig. 14 as that the perturbations of positive growth rate are concentrated in the region of small wavenumbers. This explains the molecular dynamics simulation performed by Koplik et al [44], where they observed

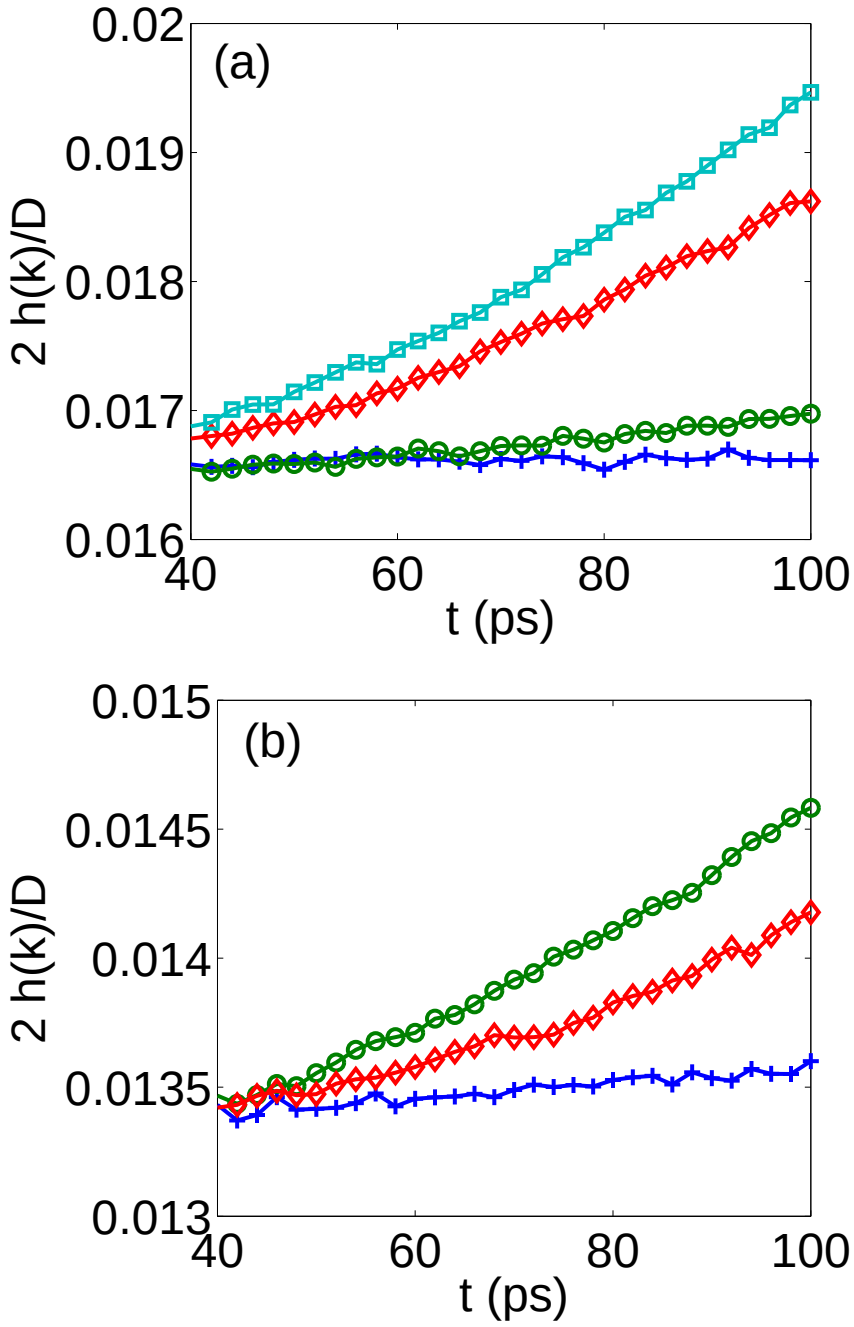


**Figure 13:** Exponential growth of perturbations of different wavelengths in the first 100 ps for nanobridges with diameters 6 nm and 8 nm. Note that the results are averaged over 400 independent nanobridges and that since the first 20 ps is the thermalization process, the start time in the figures is 40 ps. (a) the diameter of the nanobridge is 6 nm. The "+", "○","◇", and "□" lines are the growth curves of wavenumber $k = 2\pi/\mathrm{L}$, $6\pi/\mathrm{L}$, $12\pi/\mathrm{L}$ and $18\pi/\mathrm{L}$ respectively. (b) the diameter of the nanobridge is 8 nm. The "+","○", and "◇" lines are the growth curves of wavenumbers $k = 4\pi/\mathrm{L}$, $12\pi/\mathrm{L}$ and $20\pi/\mathrm{L}$ respectively.

that when the ratio of length to diameter is small enough, the break-up process of a nanobridge could not happen. The growth rate dispersion curves also show that because there is only one fastest growing perturbation mode in a nanobridge, the average size of the main droplets resulted from the break-up process is determined by the wavelength of this mode. This explains the phenomena observed in the molecular dynamics simulation in Ref. [42, 55], where the size of droplets was found fluctuating around some average value.

Quantitatively, the growth rate curves obtained from the molecular dynamics simulations are compared with Chandrasekhar's instability theory (in an expanded form) [9, 17] for a viscous liquid bridge (which can also obtained from the linear analysis [51] based on the stochastic lubrication equations [55] as discussed in the previous section) and Rayleigh's instability theory for an inviscid liquid bridge [73, 17]. We fit the data obtained from the molecular dynamics simulation using the above two growth rate dispersion formulas and the results are displayed in Fig. 14 along with the simulation data. The growth rate dispersion curves obtained from the simulation show that the largest wavenumber of an unstable perturbation is $k_{max} = 2/D$ (the corresponding wavelength is $\lambda_{min} = \pi D$). This quantitative criterion for the occurence of the instability on a nanobridge agrees well with both Chandrasekhar's and Rayleigh's theories. When the shape of the growth rate dispersion curves are considered, the best fit curves of Rayleigh's formula (see Eq. (6.21) and triangles in the Fig. 14) do not match the data obtained from the molecular dynamics simulations (the circles in the Fig. 14) for all the wavenumbers of positive growth rate; while the best fitting curves of the Chandrasekhar's formula (see Eq. (6.18) and the solid curves in Fig. 14) basically catch the shape of the molecular dynamics simulation data. These results suggest that viscosity can not be neglected for the analysis of the instability of a nanoscale flow system and inviscid models are essentially not applicable to a nanoscale hydrodynamical system (also see the discussions in Ref. [55]).

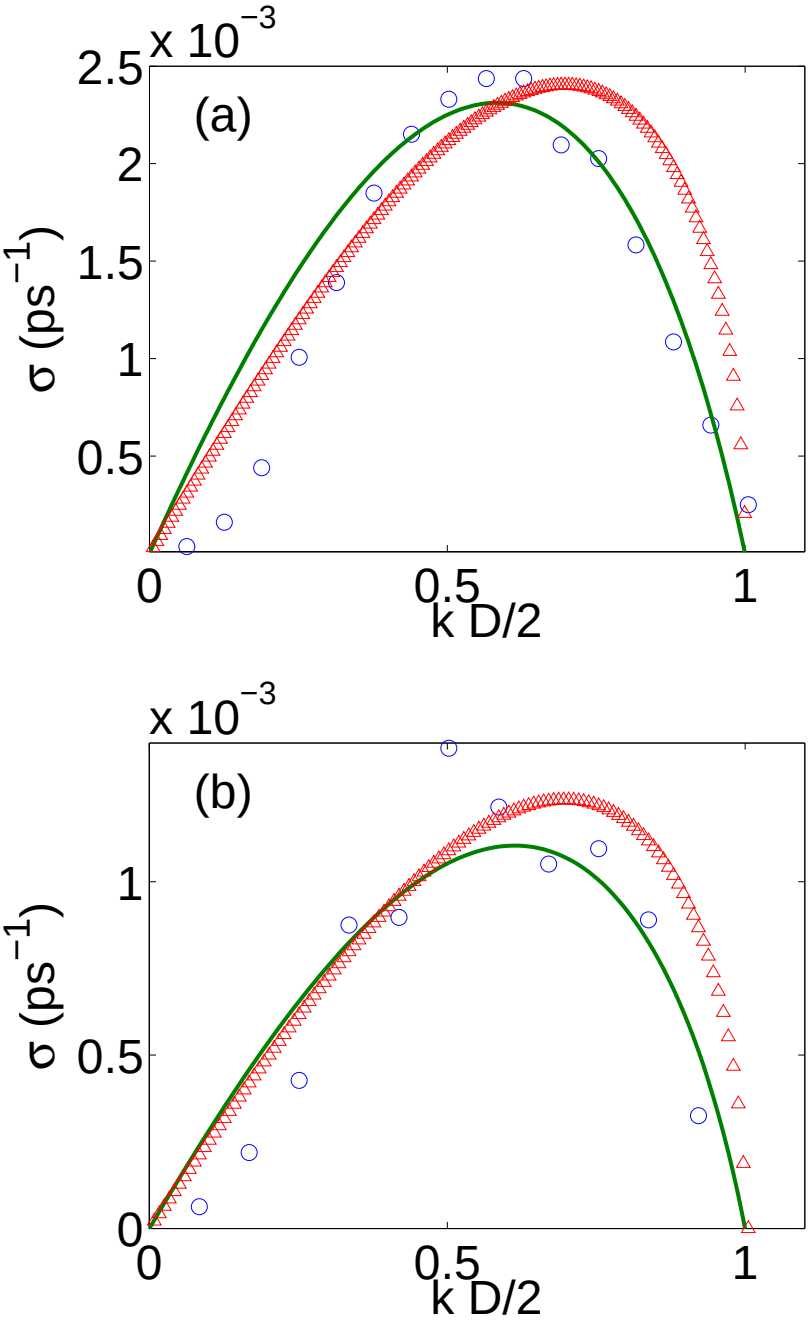


**Figure 14:** The growth rates of perturbations with different wavenumbers. (a) The growth rate of a nanobridge with a diameter of 6 nm. The circles are the averaged results of 400 independent MD simulations. The solid line is the best fit curve of Chandrasekhar's formula (Eq. (6.18)) with $\sigma_0 = 9.1 \times 10^{-3}$ ps$^{-1}$ and Re = 4.3. The triangles are the best fit curve of Rayleigh's formula (Eq. (6.21)) with $\sigma_0 = 0.007$ ps$^{-1}$. (b) The growth rate of a nanobridge with a diameter of 8 nm. The circles are the averaged results of 400 independent MD simulations. The solid line is the best fit curve of Chandrasekhar's formula (Eq. (6.18)) with $\sigma_0 = 4.1 \times 10^{-3}$ ps$^{-1}$ and Re = 7.6. The triangles is the best fit curve of Rayleigh's formula (Eq. (6.21)) with $\sigma_0 = 0.0035$ ps$^{-1}$.

When the parameters $\sigma_0$ [from Eq. (6.19)] and $Re$ [from Eq. (6.20)] in Chandrasekhar's formula [Eq. (6.18)] are calculated with the bulk properties of liquid propane at 185 K, it turns out that the values of the parameters thus calculated are quite different from those obtained from the molecular dynamics simulations. For bulk liquid propane, $\rho = 600$ kg/m$^3$, $\eta = 4.6 \times 10^{-4}$ Ns/m$^2$ and $\gamma$=0.01 N/m [55, 92], calculation shows that for a nanobridge of diameter 6 nm, $\sigma_0 = 0.0248$ ps$^{-1}$ and $Re = 0.292$; and for a nanobridge of diameter 8 nm, $\sigma_0 = 0.0161$ ps$^{-1}$ and $Re = 0.337$. However, the measurement of the simulation data shows that for a nanobridge of diameter 6 nm, $\sigma_0 = 9.1 \times 10^{-3}$ ps$^{-1}$ and $Re = 4.3$; and for a nanobridge of diameter 8 nm, $\sigma_0 = 4.1 \times 10^{-3}$ ps$^{-1}$ and $Re = 7.6$ (see Fig. 14).

The difference between the measured and calculated values of $\sigma_0$ and $Re$ may reflect a fundamental distinction between the instability of a nanobridge and a macroscopic liquid bridge. Note that on the surface of a nanobridge, there is an interfacial surface layer, where the density of liquid propane decreases to zero from the bulk value. This observation naturally leads to an interesting theory of the occurrence of the instability of a nanobridge. i.e., the instability of a nanobridge first emerges in the interfacial surface layer, where the density, viscosity and surface tension are much smaller than the values in the bulk liquid; and hence has a smaller growth rate and a larger Reynolds number. This conclusion is supported by the calculation of $\gamma$ and $\eta$ from the $\sigma_0$ and $Re$ obtained from the molecular dynamics simulation. When the density $\rho$ takes the value 166 kg/m$^3$, which is the cutoff density for the definition of liquid surface in our simulation, for a nanobridge of diameter 6 nm, we obtain that $\gamma = 3.7 \times 10^{-4}$ N/m and $\eta = 3.2 \times 10^{-6}$ Ns/m$^2$; for the diameter 8 nm, $\gamma = 1.8 \times 10^{-4}$ N/m$^2$ and $\eta = 1.4 \times 10^{-6}$ Ns/m$^2$. Both the effective surface tension $\gamma$ and the effective viscosity $\eta$ are two orders smaller than their bulk values.

Note that the growth rate dispersion curves obtained for the molecular dynamics simulation do not perfectly match Chandrasekhar's instability formula (which can also

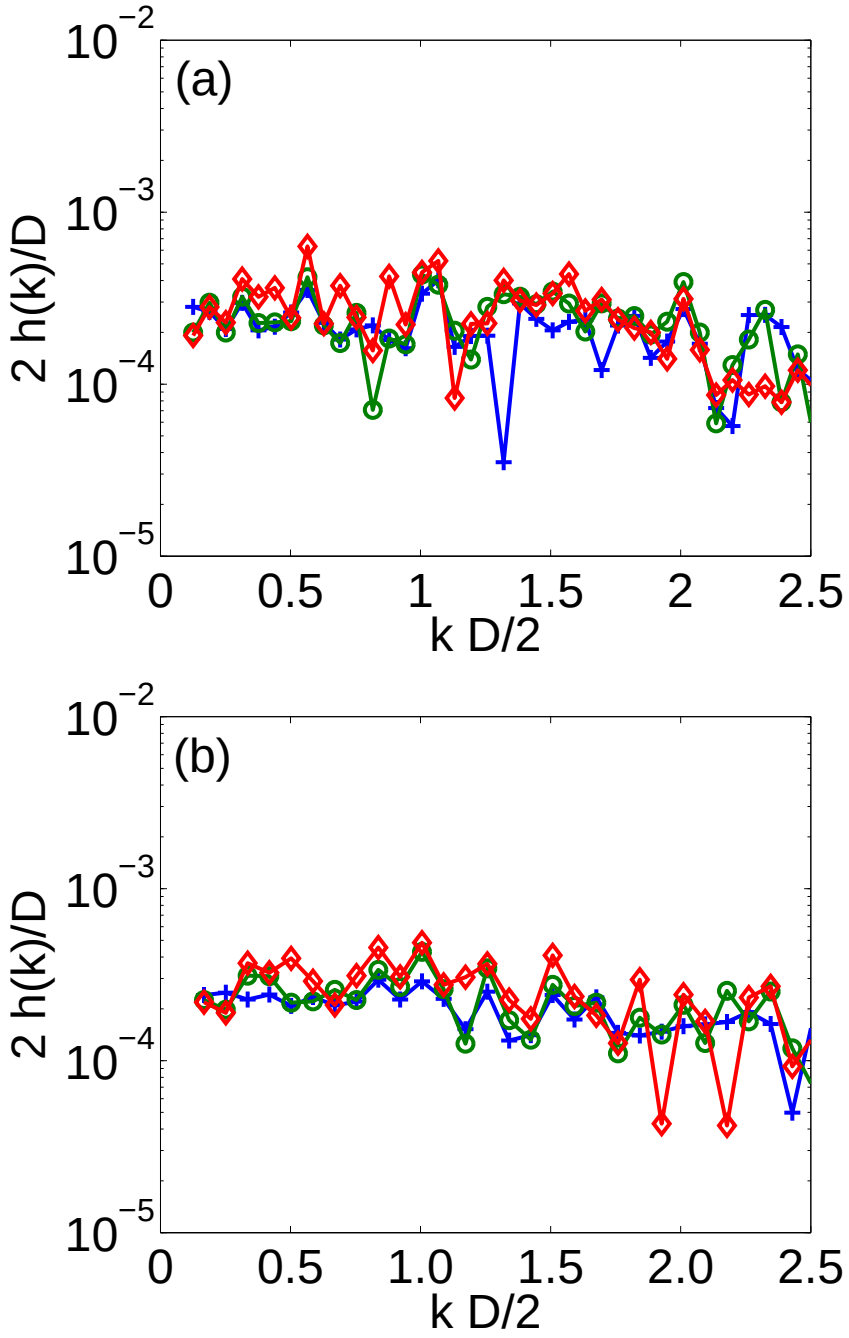


**Figure 15:** The spatial spectrum of nanobridges with perturbations provided by thermal fluctuations. (a) The diameter of the nanobridge is 6 nm. The "+", "$\circ$", and "$\diamond$" lines represent the spatial spectrum at t = 40 ps, 60 ps, and 100 ps respectively. (b) The diameter of the nanobridge is 8 nm. In the figure, the symbols and lines have the same meanings as in (a). Note that as the time elapses, the amplitudes of the spectrum remains constant and in the order of $10^{-4}$.

be obtained from the linear instability analysis based on the stochastic lubrication equations). When $kD/2 < 0.5$, the best fitted curves of Eq. (6.21) are higher than the simulated data, and when $k$ approaches zero, the measured growth rate curves have vanishing slopes. These cannot be explained by any of the instability theories we have considered in this chapter. Further understanding of nanoscale hydrodynamical systems is needed to obtain a complete explanation.

In many cases, perturbations in a nanoscale flow are provided by thermal fluctuations. On this condition, the perturbations have various wavenumbers simultaneously. An illustrative example for this is a nanobridge of uniform initial diameter. It is quite different from the case of measuring the growth rate dispersion curves, where the perturbation on the surface has only a single wavelength. In this case, the growth rate dispersion curves measured using the ensemble average method are essentially vanishing. As shown in Fig. 15, the spatial spectra of a nanobridge are basically not changed for the entire period (100 ps) of our measurement. The apparently vanishing growth rate is due to the uniformly distributed random phases of the perturbations, which mainly result from the spatial "whiteness" of thermal fluctuations [31]. When averaged, the growth of the amplitudes of all the perturbations is hidden by the cancelling effect of the interference between phases. To extract useful instability information from the nanobridge, the structure function (Eq. (6.4)), which is a second order statistical moment of the system [31], is measured.

The structure function (Eq. (6.4)) provides detailed information for the evolution of the perturbations on the surface of a nanobridge. As displayed in Fig. 16, at a very early moment (t = 30 ps) in the evolution of the instability, a small bump structure ( shown as the "+" curves in the structure function curves in Fig. 16) arises from the noisy background with its center at around $k = 5/D$. As the time elapses, the size of the bump increases and the peak of the structure function shifts to the left, along which the wavenumber decreases. At the end of our measurement (t = 100 ps), the

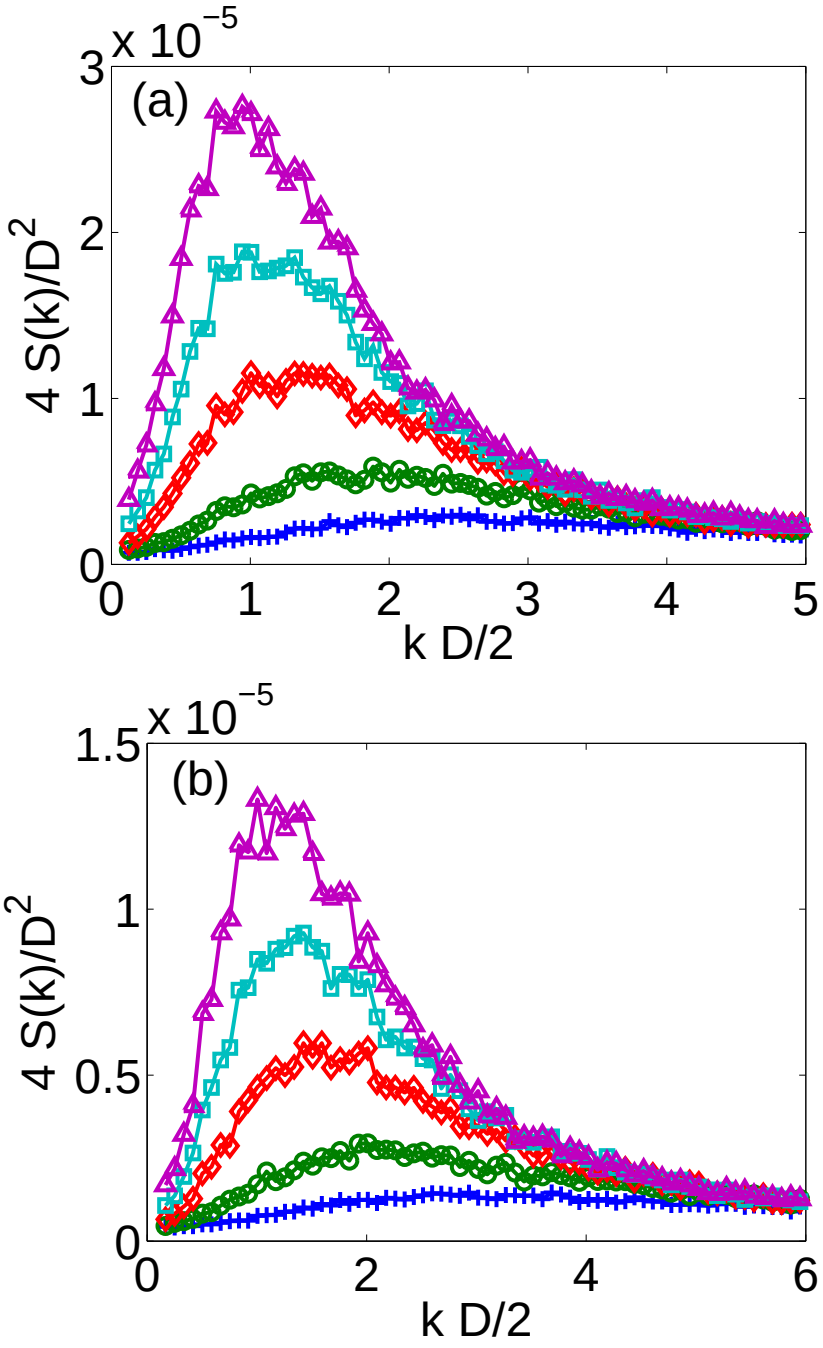


**Figure 16:** The structure functions of the perturbations on the surface of nanobridges. (a) The diameter of the nanobridge is 6 nm. The "+", "○", "◇", "□" and "△" lines represent the structure functions at t = 30 ps, 40 ps, 80 ps, 100 ps. (b) The diameter of the nanobridge is 8 nm. The symbols and lines used in this figure have the same meanings as in (a). Note that the swells of the structure functions have broader widths compared with the wavenumber range with positive growth rates. As the time elapses, the peaks of the structure functions move to the small wavenumber part.

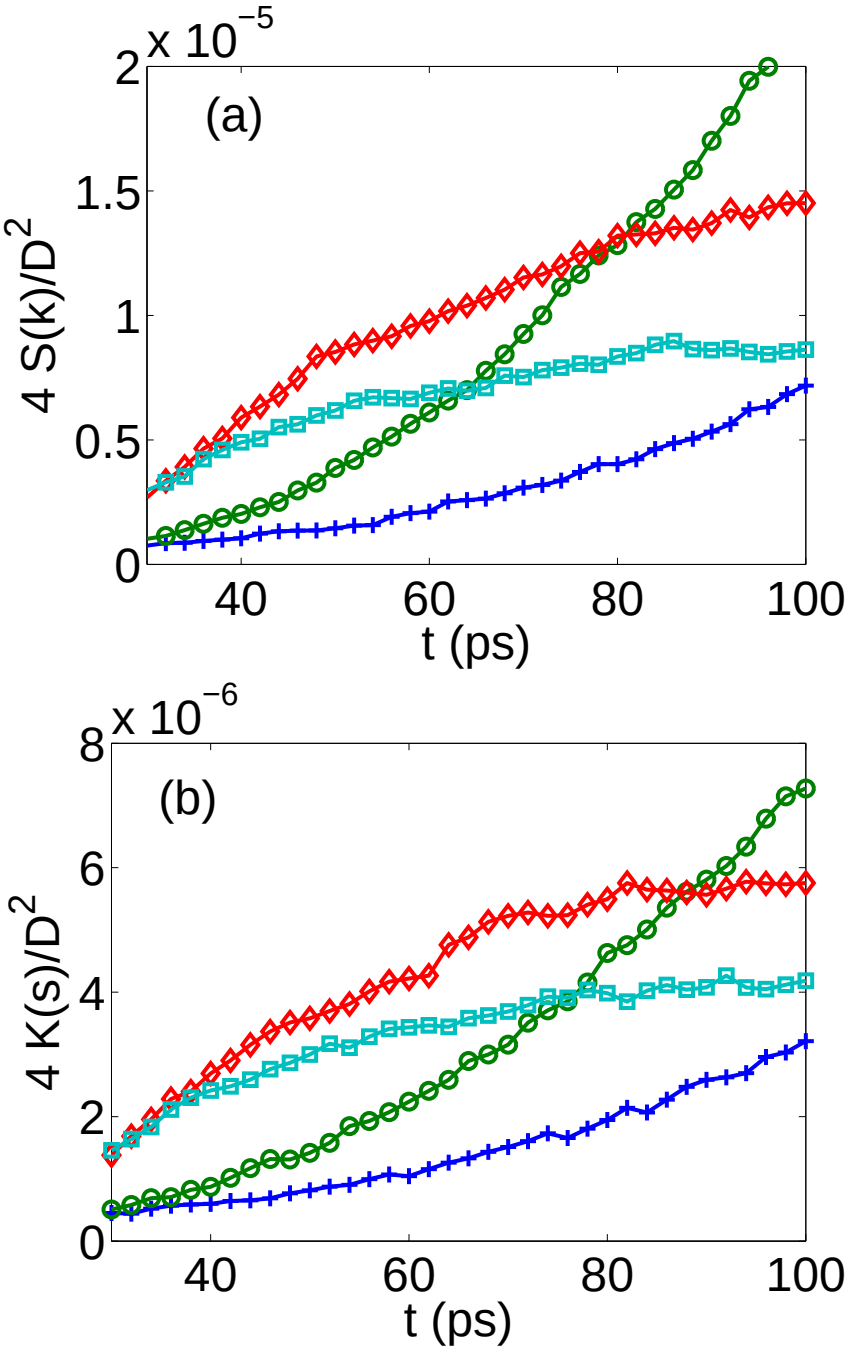


**Figure 17:** The time evolution of the structure functions of various wavenumbers. (a) The diameter (D) of the nanobridge is 6 nm. The "+","○","◇",and "□" lines are structure functions of the perturbations of wavenumbers $8\pi$/L, $18\pi$/L, $60\pi$/L, and $80\pi$/L respectively. (b) The diameter of the nanobridge is 8 nm. The "+","○","◇",and "□" lines are structure functions of the perturbations of wavenumbers $8\pi$/L, $14\pi$/L, $60\pi$/L, and $70\pi$/L respectively. Note that the growth of the perturbations with large wavenumbers satuated after some time; only those perturbations with small wavenumbers keep growing.

peak of the structure function moves to near $k = 2/D$ with a broad width (see the "$\triangle$" curves in Fig. 16). Note that, this does not imply that the perturbation with a large wavenumber has a positive growth rate. As shown in Fig. 17, since the peak of the structure function moves to the region with smaller wavenumbers as the time elapses, the growth of the perturbation with a large wavenumber actually saturates after some time. Only those perturbations with small wavenumbers keep growing with time.

The evolution of the structure function (as displayed in Fig. 17) shows that perturbations with a wavenumber greater than $2/D$ do not damp. This seems contrasted to the prediction from the growth rate dispersion curves, which states that the perturbation modes of wavenumber great than $2/D$ decrease exponentially. However, this phenomenon is the result of the complicate nonlinear interactions between perturbations of different wavenumbers. For a macroscopic bridge, these saturated perturbation structures are hidden by the perturbation of positive growth rates after enough evolution time; while for a nanobridge, the saturated perturbations are comparable with the fast growing perturbation, which makes the break-up profile looks rough and irregular.

## *6.5 Summary*

Using large scale molecular dynamics simulations, we have measured for the first time the growth rate of a propane nanobridge in vacuum. The measurements show clearly that the length-to-diameter-ratio criterion for the occurrence of the instability on a nanobridge is $\pi$. By comparing the molecular dynamics simulation data with the growth rate formula first derived by Chandrasekhar (which can also be obtained by the linear instability analysis based on the stochastic lubrication equations [55]), we reveal that the instability first emerges in the interfacial surface layer of a nanobridge. With the introduction of the concept of structure functions to describe the shape change of

a nanobridge, we find that the perturbations with large wavenumbers actually do not decay when the perturbations are provided by thermal fluctuations, they grow first and then saturate after some time. This makes the surface profile of a nanobridge have more components of large wavenumbers during its pinch-off process, and leads to a breakup profile characterized by swells with rough surfaces and sizes fluctuated around an averaged length.

Our investigations on the instability not only may be used to guide the design and applications of nanofluidic devices, it also sheds some light to the instability of macroscopic liquid bridges or jets at very early stage. Methodologically, our investigation (together with Moseler and Landman's [55] and Kadau et al.'s [40, 39]) shows that quantitative study of hydrodynamics on the nanoscale using molecular dynamics simulations is practical. It provides a powerful way to study the hydrodynamical problems involving atomic scales.

# CHAPTER VII

# NANOBRIDGES IN GASEOUS ENVIRONMENT – CROSSOVER OF UNIVERSAL BREAKUP PROFILES

Generation, stability and breakup of fluid structures with reduced dimensions (nanoscale jets and bridges) are topics of basic interest due to the unique behavior of liquids at extreme small sizes, as well as fundamental questions pertaining to the applicability of the Navier-Stokes continuum hydrodynamics for liquids miniaturized to the limit of molecular dimensions [55]. Added interest derives from technological considerations in the areas of surface patterning, printing [93], droplet formation [47], spraying [97], and drug delivery [22]. Recently, it has been shown through molecular dynamics simulations [55] that coherent liquid (propane) jets and bridges, with a diameter as small as 6 nm, can indeed be formed in vacuum, and that the stability and breakup processes of these structures close to pinch-off differ radically from those found at larger sizes. In particular, it is commonly observed for larger fluid structures that the breakup profile exhibits an extended thin long thread with an asymmetric profile of the liquid about the pinching point [95, 17] (in agreement with the deterministic lubrication approximation to the Navier-Stokes equations). The long-thread profile has been shown [17] to be a universal solution (i.e., independent of initial conditions) of the deterministic lubrication equations.

For liquid structures of reduced size a qualitatively new universal breakup profile, resembling two cones joined at their apexes (called the double-cone profile) and leading to a symmetric pinch-off, was unveiled through molecular dynamics simulations [55]. These findings led to derivation of a stochastic hydrodynamic lubrication equations with size-dependent stress fluctuations included, that successfully reproduced

the simulation results [55]. Subsequent analysis of the stochastic lubrication equations confirmed [18] that indeed symmetric pinch-off is the most probable outcome of the stochastic lubrication equations and that fluctuations speed up the breakup process, dominating over the effect of surface tension. We remark that the focus here is on the occurrence probabilities of various solutions, and in particular on finding the most probable solution (when it exists).

Here we discovered through molecular dynamics simulations of propane nanobridges in a gaseous environment (propane or nitrogen), that at sufficiently high partial gas pressure two breakup profiles occur with essentially equal probabilities: one is the aforementioned symmetric, double-cone solution (discussed before in the context of a vacuum environment [55]), and the other one is the asymmetric, long thread profile. The reappearance of the long thread breakup profile of the nano-bridge, caused by the gaseous environment, is particularly surprising, since this universal solution has been discussed previously only for macroscopic liquid systems [95, 17]. We find that the microscopic origin of the emergent crossover of universal breakup regimes discussed by us in this chapter, involves the effect of the surrounding gas on evaporation-condensation processes of the nanobridge. One of the main achievements of this study is the formulation of a modified stochastic lubrication equation description where a curvature-dependent term, representing the dependence of the evaporation-condensation flux on the presence of the surrounding gas, is included in the continuity equation. Integration of the newly derived modified stochastic lubrication equations is shown to yield results that agree well with the molecular dynamics computer experiments.

## *7.1 Methodology*

The methodology and interaction potentials for propane ($C_3H_8$) employed in our molecular dynamics simulations have been described in chapter 2 and Ref. [55], and

the $N_2$ intermolecular interaction was chosen after Ref. [28] , with a soft spring (K = 112 J/m$^2$) connecting the nitrogen atoms (refer to chapter 2 for details). The interaction between the propane and nitrogen molecules was described by a 6-12 Lennard-Jones potential with the potential well depth $\epsilon$, and the distance parameter $\sigma$, obtained from the Lorentz-Berthelot mixing law [56]. The simulations were performed in a three dimensional cubical calculational cell with a side length of 30 nm, and an initially cylindrical liquid bridge of length L = 30 nm and a radius h = 3 nm was placed in the center of the cube; two short cylindrical end caps (made of frozen liquid propane, with the atoms remaining static throughout the molecular dynamics simulation), each with a diameter of 8 nm and a thickness of 2 nm, were placed at both ends of the bridge.

When the propane bridge developed in the presence of its own vapor the system was closed through the use of reflective boundary conditions at the computational cell boundaries. In simulations of a liquid bridge system in a nitrogen gas environment, propane molecules that reach the computational cell boundaries were removed, while nitrogen molecules were confined by the similar reflective cell boundaries. Prior to the start of the simulation of the dynamic evolution of the bridge, the liquid nanostructure and the ambient gas (when present) were thermalized to a temperature of 185 K, which is below the boiling temperature (230 K) and well above the melting temperature (84 K) of propane. In our simulations we considered nitrogen densities up to 34.85 kg/m$^3$ (corresponding pressure of $\sim$ 1.7 MPa), to avoid condensation.

## *7.2 Simulation results*

Fluctuation noise dominates the breakup behavior of liquid structures (liquid bridges in particular) whose diameter, d = 2h, is comparable to the thermal length scale (of the order of a nanometer), determined by the relation between the thermal energy, $k_BT$, and the surface tension $\gamma$, i.e. $L_T = \sqrt{k_BT/\gamma}$ [55]. In addition, observation of

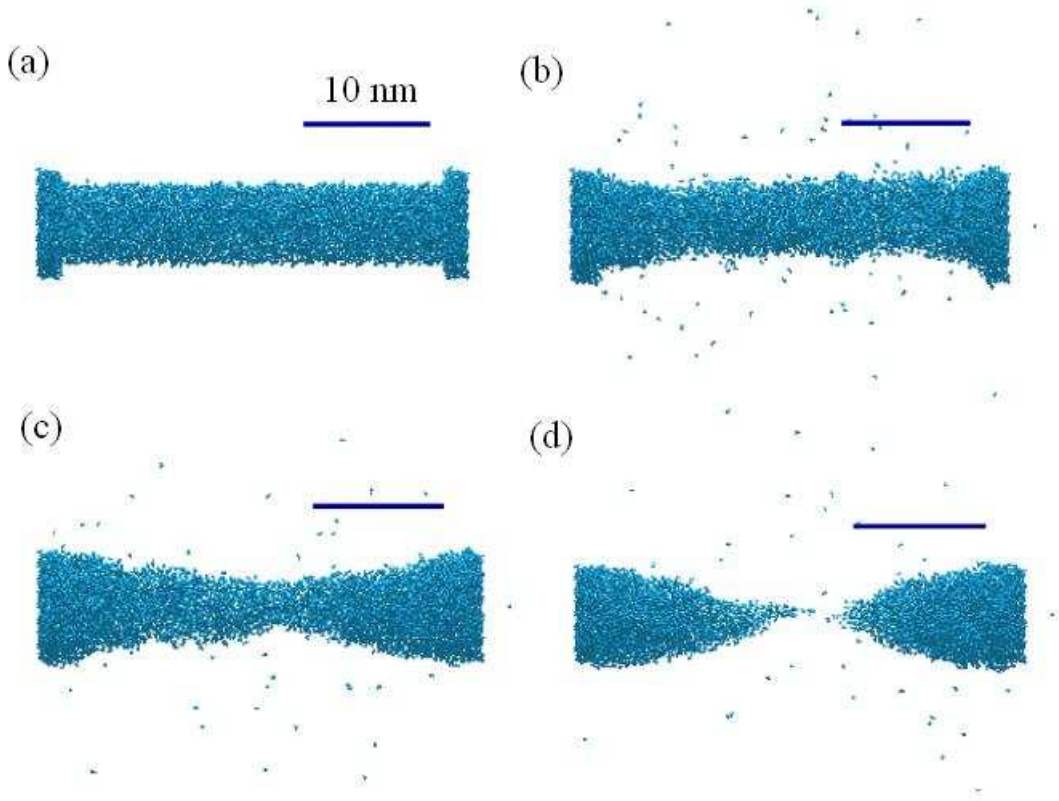


**Figure 18:** A typical breakup processes of a propane liquid bridge in vacuum at 185K, recorded in a molecular dynamics simulation, at t = 0 (a), 200 ps (b), 400 ps (c), and 547 ps (d). The breakup profile is shown in (d), exhibiting a geometry of two cones joined at the apex and pinching in the middle. The length of the nanobridge is 30 nm and its initial average radius is 3nm. Note also some evaporation of the bridge molecules.

breakup requires that the length of the liquid bridge will obey L $> \pi d$, which is the smallest wavelength of a perturbation that leads to instability of the liquid bridge [17]; this is satisfied for all our systems.

We have showed in chapter 5 through molecular dynamics simulations that for a sufficiently large liquid bridge (i.e. initial configuration with L=120 nm and d = 24 nm, containing over $1.3 \times 10^6$ particles), asymmetric long thread breakup occurs. This breakup mode is also found by the lubrication equations, as well as the stochastic lubrication equations, which yields a long-thread breakup profie with a high probability, $P_{LT} = 0.7$. Reducing the initial diameter of the liquid bridge results in the emergence

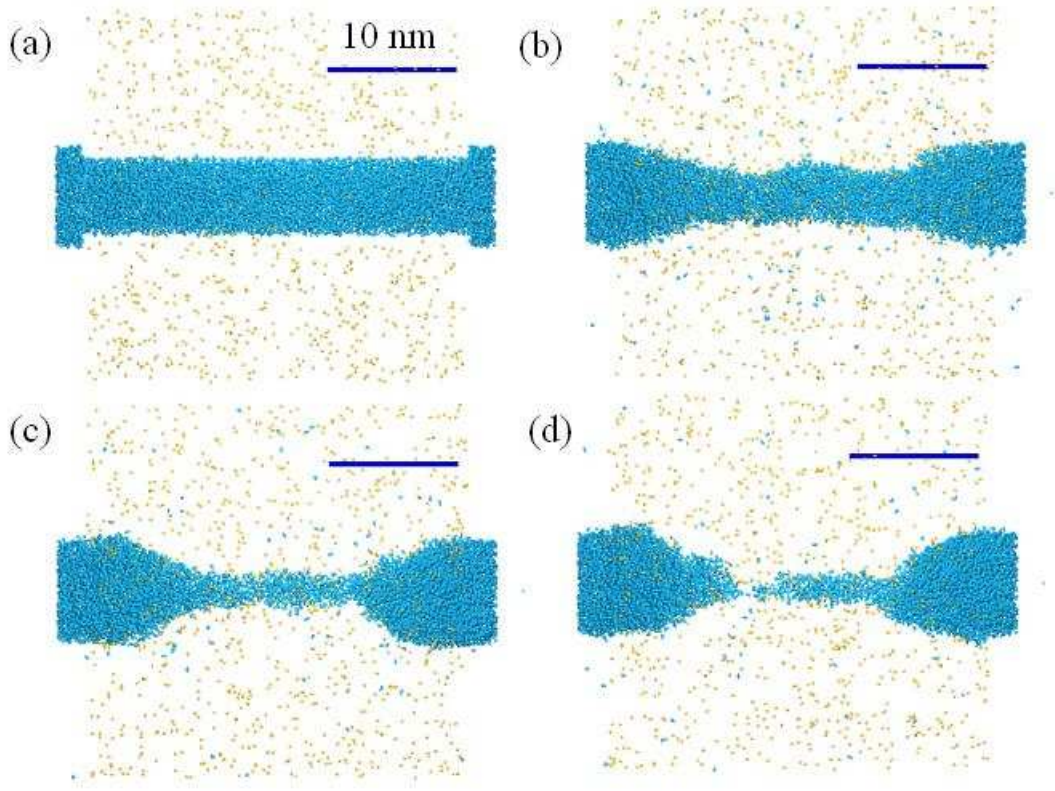


**Figure 19:** A typical breakup processes of a propane liquid bridge (blue) at 185K in an ambient nitrogen gas (yellow) environment (density of 6.0 kg/m$^3$, with a corresponding partial pressure of 0.36 MPa), recorded in a molecular dynamics simulation at t = 0 (a), 400 ps (b), 760 ps (c), and 840 ps (d). The breakup profile is shown in (d), exhibiting a geometry of a long-thread pinching on the left. The length of the nanobridge is 30 nm and its initial average radius is 3nm.

of a new universal breakup density profile (see chapter 4 for details). The development of a double-cone pinch-off profile [55] is reproduced in Fig. 18 (for comparison with the nanobridge in gaseous environment), through selected configurations taken from molecular dynamics simulations of a smaller size propane bridge (L = 30 nm, and d = 6 nm). In this case the stochastic lubrication equations yielded a double-cone profile with a probability of $P_{DC}$= 0.7, and $P_{LT}$ =0.3.

When adding ambient gas (here we use molecular nitrogen) to the bridge system the shape of the most probable breakup profile changes in a remarkable manner. In these simulations the density of the gas was increased up to 34.85 kg/m$^3$ (the density

of air under common conditions is about 1.22 kg/m$^3$). For low ambient gas densities the double-cone pinch-off profile maintains. However, when the ambient gas density is increased to above 3.5 kg/m$^3$ (a corresponding partial pressure of about 0.19 MPa, or about 2 atm) another breakup configuration emerges, characterized by a long thread (Fig. 19), with its probability of occurrence rising to a saturation value $P_{LT} = 0.5$ over a relatively narrow partial pressure range. Simulations of a propane liquid bridge in a closed empty calculation box show similar results to the case of surrounding $N_2$ gas. Here, the breakup of the bridge in contact with its vapor exhibits a long-thread pinch-off profile with a 0.5 probability when the vapor pressure is about 0.8 MPa. While for the double-cone configuration the nanobridge pinch-off occurs in the middle of the bridge (and the liquid profile is symmetric), for the new long-thread pinch-off profile breakup occurs at either end of the bridge (and the profile is asymmetric).We recall that the long-thread breakup profile is commonly observed for macroscopic systems, and it is indeed the universal solution [17] for the breakup configuration described through the lubrication equations.

## *7.3 Modification of the stochastic lubrication equations*

Observation of a new, double-cone breakup profile in molecular dynamics simulations of liquid jets and bridges of nano-scale sizes (see Fig. 18 and top panel in Fig. 20(a)), and the failure of the lubrication equations to account for the new behavior (see middle panel in Fig. 20(a)) provided the impetus for reformulation of the hydrodynamic equations for systems of reduced dimensions [55]. This led to derivation of the stochastic lubrication equations where size-dependent fluctuations are included. These equations have been shown numerically [55] and analytically [18] to result in symmetric breakup with a double-cone pinch-off geometry (see bottom panel in Fig. 20(a)) which replaces the long thread as the most probable universal breakup profile. In light of these developments, the reemergence of the long-thread

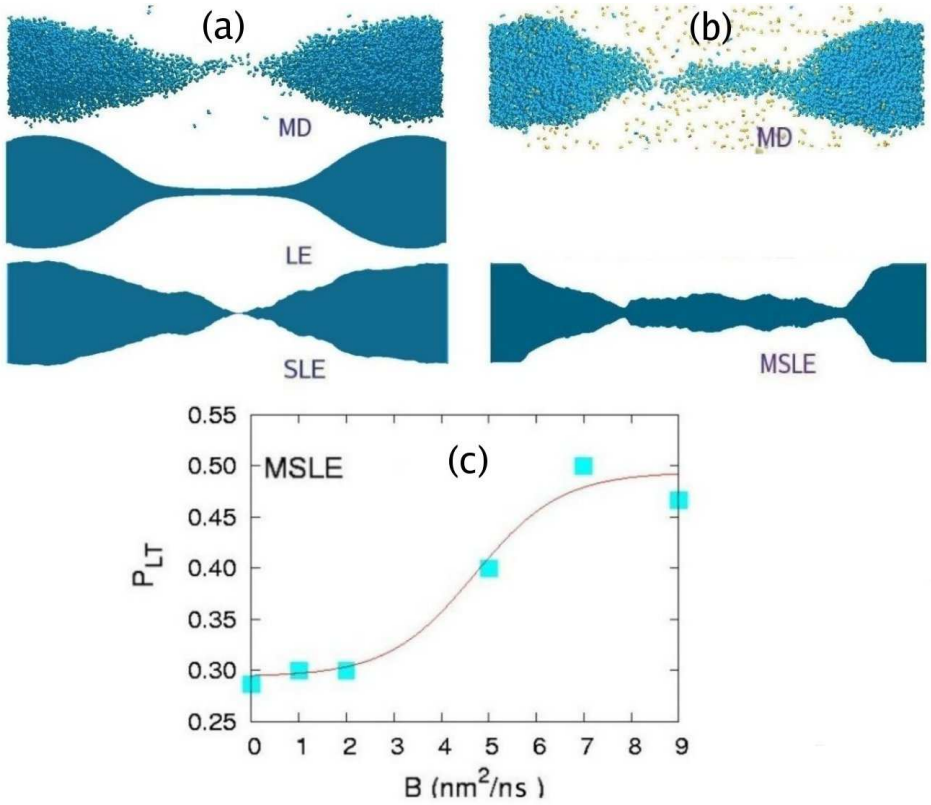


**Figure 20:** (a, b) Breakup configurations of propane bridges taken from microscopic molecular dynamics (MD) simulations and from continuum hydrodynamic lubrication equations (LE) (Eqs. (7.5) and (7.6) without the last term on the right of Eq. (7.5) and B = 0 in Eq. (7.6)) , stochastic lubrication equations (SLE) (Eqs. (7.5) and (7.6) with B = 0) and modified stochastic lubrication equations (MSLE) calculations (Eqs. (7.5) and (7.6)). (c) The occurrence probability of the LT break-up profile for a propane bridge in an $N_2$ gaseous environment, obtained from solution of the MSLE, for a range of values of the coefficient B in Eq. (7.6). (a) top: DC breakup configuration from MD simulations of a propane bridge at 185K; middle: the LT breakup configuration for the propane bridge obtained from the continuum LE equations; bottom: the DC profile obtained through solution of the SLE equations. (b) top: The breakup profile exhibiting a LT obtained from MD simulations of the propane bridge in an $N_2$ gaseous environment described in the caption to Fig. 19; bottom: the LT breakup configuration obtained from solution of the MSLE (B = 6.9 nm$^2$/ns). (c) Occurrence probability of the LT breakup profile obtained from solution of the MSLE for selected values of B. Each solid square was calculated from 20 simulations of the MSLE, each with a different random noise sequence. A line fit is added to guide the eye.

breakup profiles for nano-scale systems (liquid bridges and jets) in the presence of a surrounding gaseous environment, culminating in asymmetric pinch-off, is rather surprising. Furthermore, we have shown through extensive examination of the spectrum of fluctuations of these systems that the nature of fluctuations (white noise) that characterizes them is essentially indistinguishable from the one found for the same liquid systems in vacuum (see Fig. 21). Consequently the reemergence of the long-thread breakup can not be attributed to environmentally-induced decreased, or largely modified, contribution of the intrinsic size-dependent fluctuations underlying the stochastic lubrication equations description.

The effect of the environment on the liquid system can be incorporated into the continuum stochastic formalism by taking into account the leading microscopic contribution of the environmental particles. Several candidates are considered in the modeling process. (i) Variation of the surface tension of the fluid due to incorporation of gas molecules (nitrogen) are considered. However, this effect was not found in our simulations. (ii) When surface diffusional currents triggered by collisions of gaseous molecules with the liquid surface was incorporated we found that such currents are too small to influence our results. (iii) When the evaporation condensation was considered, we found it provided a perfect mechanism to the effect of the environment. The modification process of the stochastic lubrication equations are described as follows [64].

For a segment of the fluid with a local curvature $\kappa(z)$ (with the z axis along the bridge), the vapor pressure inside the liquid, $P(z)$, near equilibrium, is given by the following approximation to the Gibbs-Thompson equation

$$\Delta P(z)/P_0 = \kappa(z)\gamma v_0/k_B T, \tag{7.1}$$

where $P_0$ is the pressure of the environmental gas (assumed to be ideal) in equilibrium with a planar surface ($\kappa = 0$), $\Delta P(z) = P(z) - P_0$, $\gamma$ is the surface free energy of the fluid, and $v_0$ is the volume of a fluid molecule; note that since the bridge geometry

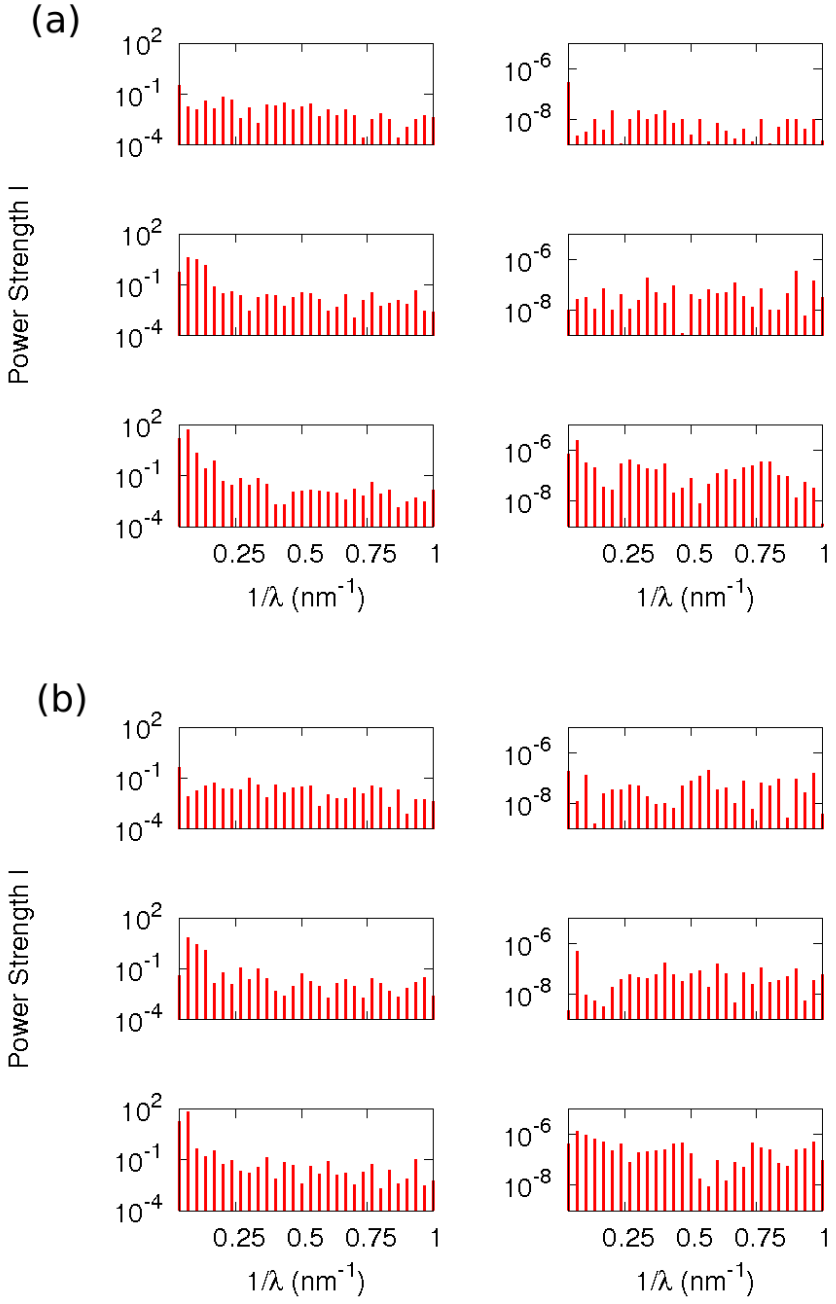


**Figure 21:** The Discrete Fourier Transform (DFT) of a liquid nanobridge at various times. The left columns are the DFT of the radius profile $h(z)$ and the right columns are the DFT of the axial velocity $v(z)$. (a) In vacuum (as displayed in Fig. 18). From top to bottom, the snapshot time of the first row is t = 0 ps; the time for the second row is t = 400 ps; and the time for the third row is t = 547 ps, which is just before the breakup of the nanobridge. (b) In nitrogen gas (as displayed in Fig. 19). From top to bottom, the snapshot time of the first row is t = 0 ps; the time for the second row is t = 400 ps; and the time for the third row is t = 840 ps, just before the breakup. No difference was found between the spectra of fluctuations in these two cases.

does not cause trapping of the surrounding gas, and since the mean-free path in the surrounding gas is sufficiently large, $P_0$ is essentially constant along the fluid structure. Using the fluid evaporation and condensation fluxes, given by

$$j_{ev} = P(z)/(2\pi M k_B T)^{1/2}, \tag{7.2}$$

where $M$ is the weight of a fluid molecule, with the condensation flux ($j_{cond}$) given by the same expression but with $P(z)$ replaced by $P_0$, we obtain for the net evaporation-condensation flux

$$j(z) = j_{ev} - j_{cond} = \Delta P(z)/(2\pi M k_B T)^{1/2} = B\kappa(z), \tag{7.3}$$

with

$$B = P_0 \gamma v_0^2/(2\pi M)^{1/2}(k_B T)^{3/2}. \tag{7.4}$$

The curvature dependence of the net flux $j(z)$ can now be included in the continuity equation (Eq. (7.6) below), which together with the stochastic lubrication equations' [55] velocity equation (Eq. (7.5) below) gives the modified stochastic lubrication equations for the velocity, $v(z,t)$, and radius, $h(z,t)$, of the fluid nanostructure

$$\begin{aligned} \partial_t v + v\partial_z v &= -\frac{\gamma}{\rho}\partial_z \kappa + 3\frac{\eta}{\rho}\partial_z(h^2\partial_z v)/h^2 \\ &\quad -\frac{1}{\rho}\sqrt{\frac{3k_B T\eta}{\pi}}\partial_z(h\Gamma)/h^2, \end{aligned} \tag{7.5}$$

$$\partial_t h + v\partial_z h = -(\partial_z v)h/2 - B\kappa. \tag{7.6}$$

The curvature is given by

$$\kappa(z,t) = 1/(h(z,t)\{1 + [\partial_z h(z,t)]^2\}^{1/2}) - \partial_z^2 h(z,t)/(\{1 + [\partial_z h(z,t)]^2)^{3/2}. \tag{7.7}$$

In dimensionless form the coefficient B in Eq. (7.6) becomes $\mathrm{B}_0 = \mathrm{B}t_\eta/l_\eta^2 = \mathrm{B}(\rho/\eta)$, where $l_\eta = \eta^2/(\rho\gamma)$ and $t_\eta = \eta^3/(\rho\gamma^2)$ are the length and time scale. Another scale-free parameter appearing in the dimensionless form of Eq. (7.5) (see Ref. [55]), is $M_l = l_T/l_\eta$. For propane $\rho/\eta$ equals $1.3 \times 10^{-3}$ ns/nm$^2$, and the crossover from

double-cone to long-thread profiles occurs for $B_0 = 8.2 \times 10^{-3}$ (corresponding to B=6.3nm$^2$/ns in Fig. 20). In Eq. (7.5), $\eta$ and $\rho$ are, respectively, the fluid viscosity and density, and $\Gamma$ is a standard Gaussian (white) noise of with a correlation of $\langle \Gamma(t)\Gamma(t') \rangle = 2\delta(t - t')$ [55]. The first term on the right in Eq. (7.5) contains the partial derivative of the Young-Laplace expression [55] for the pressure in the fluid. The curvature dependence in Eq. (7.6) represents redistribution of molecules along the bridge due to evaporation-condensation processes. Such redistribution, resulting from backscattering of evaporating molecules due to collisions with gaseous ones, becomes effective for sufficiently high gas pressures; it does not occur in vacuum and correspondingly the curvature dependent term in Eq (7.6) is not included for a nanobridge in vacuum. We have found in separate simulations that the evaporation flux in an open system consisting of a liquid propane bridge in vacuum is independent of curvature.

In the calculations of the modified stochastic lubrication equations, we used $\gamma =$ 0.01 N/m; $\eta = 4.6 \times 10^{-4}$ Ns/m$^2$; and T = 185 K. The size and boundaries of the liquid bridge were the same as in the molecular dynamics simulations, i.e., prior to the start of the breakup process the radius of the liquid propane bridge was taken to be 3 nm and, as in the molecular dynamics simulation experiments, it is supported on both ends by two short holders of 4 nm radii; these static holders were kept at fixed positions throughout the integration of the modified stochastic lubrication equations. The modified stochastic lubrication equations were solved for each B values 20 times with a different random noise seed in each simulation. The probabilities $P_{LT}$ shown in Fig. 20(c) were computed from these calculations. In calculations of the coefficient B (see discussion in the context of Eqs. (7.5) and (7.6)), the mass of a propane molecule is $M = 44 \times 1.66 \times 10^{-27}$ kg, and in order to account for the reduced density at the surface region of the nanobridge we assign the propane molecules at that region a volume that is 3 times larger than the molecular volume in bulk liquid propane, $v_0 =$

$4 \times 10^{-28}$ m$^3$.

Direct numerical integration of the above modified stochastic lubrication equations shows the appearance of a long-thread breakup profile (see Fig. 20(b), bottom, where it is shown together with a configuration taken from the molecular dynamics simulation), with the long-thread occurrence probability $P_{LT}$ increasing for larger values of the coefficient of the curvature-dependent term, B, in Eq. (2) (see Fig. 20(c)). The range of values of the coefficient B covered in the calculation of the modified stochastic lubrication equations (Fig. 20(c)) coincides with that for which we have performed most of our molecular dynamics simulations of the nanobridge. As aforementioned, in these molecular dynamics simulations the long-thread occurrence probability was found to increase for surrounding gas pressures that are larger than 0.19 MPa (corresponding to B = 3.63 nm$^2$/ns, according to the above expression for B), showing saturation at $P_{LT} = 0.5$ for gas pressures equal to (or larger than) 0.33 MPa, corresponding to B = 6.3 nm$^2$/ns. The agreement between the results of our molecular dynamics experiments and the hydrodynamic modified stochastic lubrication equations formulation supports the validity of this continuum approach to nano-scale fluid systems; in addition to the nanobridges discussed here the modified stochastic lubrication equations also describe the appearance of a long-thread breakup profile as the most probable pinch-off mode for nanojets propagating in a gaseous environment.

## *7.4 Summary*

In summary, we have unveiled here through molecular dynamics simulation experiments a universality crossover of the pinch-off density profile of collapsing liquid propane nanobridges, from a symmetric double-cone shape in vacuum to an asymmetric breakup of a long-thread profile that emerges in a gaseous environment with a sufficiently high pressure. Underlying this phenomenon is the dependence of the evaporation-condensation processes of the nanobridge on the local curvature, when

in the presence of a surrounding gas. A modification of the stochastic hydrodynamic equations for liquid nanostructures to include this curvature dependence in the continuity equation, with an amplitude that can be calculated from gas kinetic theory, is shown to faithfully capture the universality crossover of the breakup shape profiles. This extends the applicability of the stochastic hydrodynamic treatment of nanobridges and nanojets [55] beyond vacuum conditions.

# CHAPTER VIII

# GENERATION AND CONTROL OF NANOJETS INJECTED THROUGH A HEATED VIRTUAL NOZZLE

## *8.1 Introduction*

Liquid jets of reduced size, in particular in the nanometer range, have been a subject of growing activity because of their fundamental interest and industrial applications [94, 4, 84]. Recently, the generation and application of nanojets become a new focus of this subject [2, 55, 18, 20, 79]. However, industrial applications of nanojets have not yet been realized because of difficulties encountered in their generation.

Molecular dynamics studies [55] have pointed out that there are two critical factors pertaining to the generation of nanojets. One is the size of the nozzle and the other is the minimum threshold driving pressure needed to generate a coherent jet. These two factors are related to each other. With the decrease of the nozzle's size the threshold pressure increases. This relation is expressed as [55]

$$P_{th} = 16\eta l \left(\frac{\gamma}{\rho R^3}\right)^{\frac{1}{2}} \tag{8.1}$$

where $P_{th}$ is the threshold pressure, $\eta$ is the viscosity of the liquid, $l$ is the ratio of the nozzle's characteristic length L to its radius R, $\gamma$ is the surface tension of the liquid, and $\rho$ is the density of the liquid. For a gold (Au) nozzle with a diameter of 6 nm, the threshold pressure to generate a coherent liquid propane nanojet is about 500 MPa (5000 atm) [55].

It has also been revealed that the threshold pressure of the nanojet can be adjusted by the internal shape and the wettability of the nozzle [55]. A convergent nozzle not only is helpful to decrease the threshold pressure, but also increases the

axial velocity of the nanojet. When the nozzle is wetting to the liquid, the liquid molecules jam at the exit of the nozzle impeding the formation of a coherent nanojet. Special techniques, such as heating the surface of the nozzle to a temperature above the boiling point of the liquid or changing the wettability of the nozzle, have to be employed to eliminate the blocking layer [55].

However, even with the state-of-art processing techniques, it is very difficult to build a nozzle of several nanometers diameter, and it is much more difficult to process a nanoscale nozzle having a particular geometry. Heating the surface or changing the wettability of the nozzle is also very difficult to realize at the nanoscale. Even if we could overcome all these difficulties; we still have to deal with the high driving pressure problem. First, building a nozzle which can work under over 5,000 atm (500 MPa) is a technical challenge. Second, it is equally difficult to maintain such a high pressure to generate a coherent nanojet.

We show in this chapter that the above difficulties can be overcome through a simple and effective technique, i.e., heating the nozzle. When a nozzle is heated to a very high temperature (above the boiling point of the liquid in use), the outer layer of the liquid jet, which is flowing through the nozzle, is heated to above its boiling point. When the liquid jet reaches the exit of the nozzle the outer layer is boiled away quickly due to strong vaporization and a jet with a shrinking diameter is generated. With this method, we can obtain a much smaller liquid jet from a nozzle of a much larger diameter. This technique also has extra bonuses. The increase of the diameter of the nozzle decreases the threshold pressure needed to push the liquid jet out of the nozzle. Because the temperature of the entire nozzle is above the boiling temperature of the liquid, the jam problem at the exit of the nozzle is solved at the same time.

We also find that a virtual convergent nozzle is formed by the hot liquid itself inside the real nozzle, and the axial velocity of the injected jet increases on account of the formation of the virtual self-convergent nozzle. The existence of the virtual nozzle also

provides a new possibility to control the direction of the nanojet through adjusting the temperature distribution of the nozzle. This technique is also demonstrated in this chapter through molecular dynamics simulations.

## *8.2 Technical remarks on molecular dynamics simulations*

First, we explore the feasibility of the heated virtual nozzle method through large scale molecular dynamics simulations. In the simulations, the nozzle is made of platinum (Pt) and the liquid is a common fuel, i.e., propane ($C_3H_8$). The propane molecules use the same model adopted in our previous studies of nano-hydrodynamic systems [55, 92]. The platinum nozzle is modeled using an embedded-atom method (EAM) potential with the potential parameters taken from Ref. [38]. The interaction between platinum atoms and propane segments ($CH_2$ and terminal $CH_3$ segments) are modeled as a 6-12 Lennard-Jones potential with $\epsilon = 1.3$ kJ/mol and $\sigma = 0.323$ nm after Ref. [12]. The temperature of the propane "stored" in a reservoir before entering the nozzle region is 150 K, which is well below the boiling point (230 K) of propane. The liquid is heated up when it passes through the nozzle. The temperature of the nozzle has been varied in the range of 150 K to 800 K in the exploratory simulations. The propane molecules are injected into a long rectangular box with a 30 nm $\times$ 30 nm square intersection in front of the nozzle. One of the ends of the box is the surface of the nozzle, and the other end of the box is 300 nm away from the nozzle with the same shape as the nozzle surface. For convenience, the z axis is placed perpendicular to the surface of the nozzle and along the long side of the simulation box. The propane molecules are removed from the simulation once they approach the boundary of the box. Since the total number of the particles in the simulation, including the platinum atoms in the nozzle and the segments of propane molecules, is over one million, specially designed algorithms are employed to adapt the simulations to large scale parallel computers.

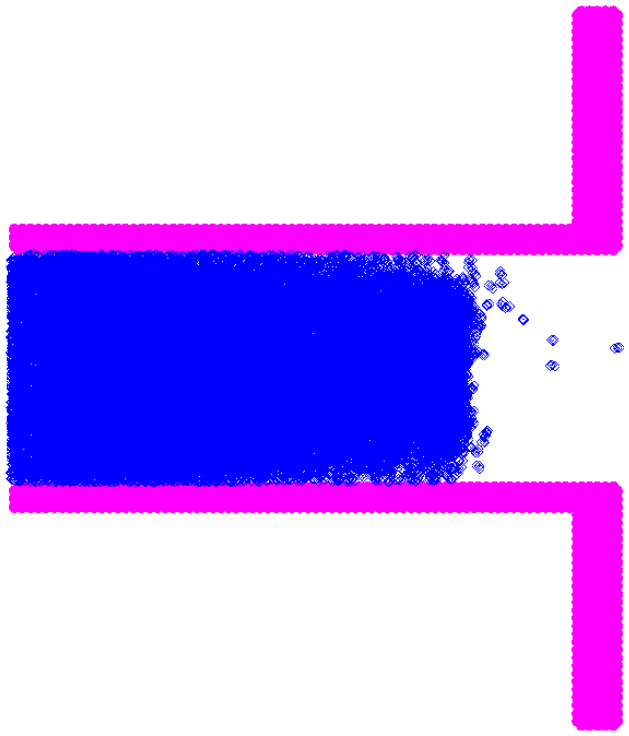

**Figure 22:** The cross-rsection of the nozzle used in the heated-nozzle technique. It is a straight cylindrical hole drilled in a square platinum plate with a surface of 30 nm $\times$ 30 nm. The length of the nozzle is 30 nm and the diameter of the nozzle is 12 nm. The liquid material in the nozzle is propane. To reduce the atom number in the simulation, only the atoms within the interaction range with propane are included.

The shape of the nozzle is displayed in Fig. 22. It is a straight cylindrical hole in a platinum plate of 30 nm thickness. Nozzles having a more complex geometry (such as that used in Ref. [55]) are not used here considering the difficulty of producing the complex shape in such a small nozzle. To reduce the number of platinum atoms, which are very time consuming in the simulations, only atoms within the interaction range with the propane molecules are included. The entire nozzle is kept at a constant temperature by contacting to a virtual thermostat using Brownian motion method [56].

The length of the nozzle is a critical parameter. It is determined by several factors including the heat transfer speed from the nozzle to the liquid, the diameter of the nozzle, the desired diameter of the nanojet outside of the nozzle, and the speed of the

liquid flow inside the nozzle. In the simulations, the length of the nozzle is optimized to obtain a smooth nanojet with a minimum diameter.

## *8.3 Nanojets from a heated nozzle and the formation of virtual self-convergent nozzle*

A typical nanojet emanating from the heated nozzle under the pressure of 220 MPa is displayed in Fig. 23. The nozzle is placed at z = 0 and is heated to 500 K. Strong vaporization is observed in front of the nozzle and no blocking layer of propane molecules is observed in the simulations. The propane vapor forms a vapor shell surrounding the liquid core of the nanojet, as displayed in Fig. 23. At the distance about 60 nm away from the nozzle, the diameter of the nanojet decreases to about half of the diameter of the nozzle; and near the other end of the simulation box, the diameter of the nanojet is just about one-third of the diameter of the nozzle. The intact length of the nanojet is longer than the length of the simulation box (300 nm). After the nanojet reaches its stationary state (after 2.0 ns) no break is observed in the box. Further increase of the nozzle temperature to 800 K makes most of the liquid propane of the nanojet become vapor, and no liquid nanojet can be observed in this condition. When the temperature of the nozzle is 500 K, the threshold pressure to generate a coherent nanojet is about 200 MPa.

In Fig 24, we show the escape flux of propane molecules from a cylindrical surface of 14 nm diameter enveloping the nanojet. Here, the escape flux is defined as the product of the number density of propane molecules at a certain point on the cylindrical surface and the radial component of their average velocity at that point. It indicates the change of the vaporization of the nanojet as a function of the distance z from the exit of the nozzle. As shown in the figure, the escape flux curve decreases quickly with the increase of the distance and it is well described by a function which is the sum of two exponential functions. With the total escape flux denoted as $R_{escape}$,

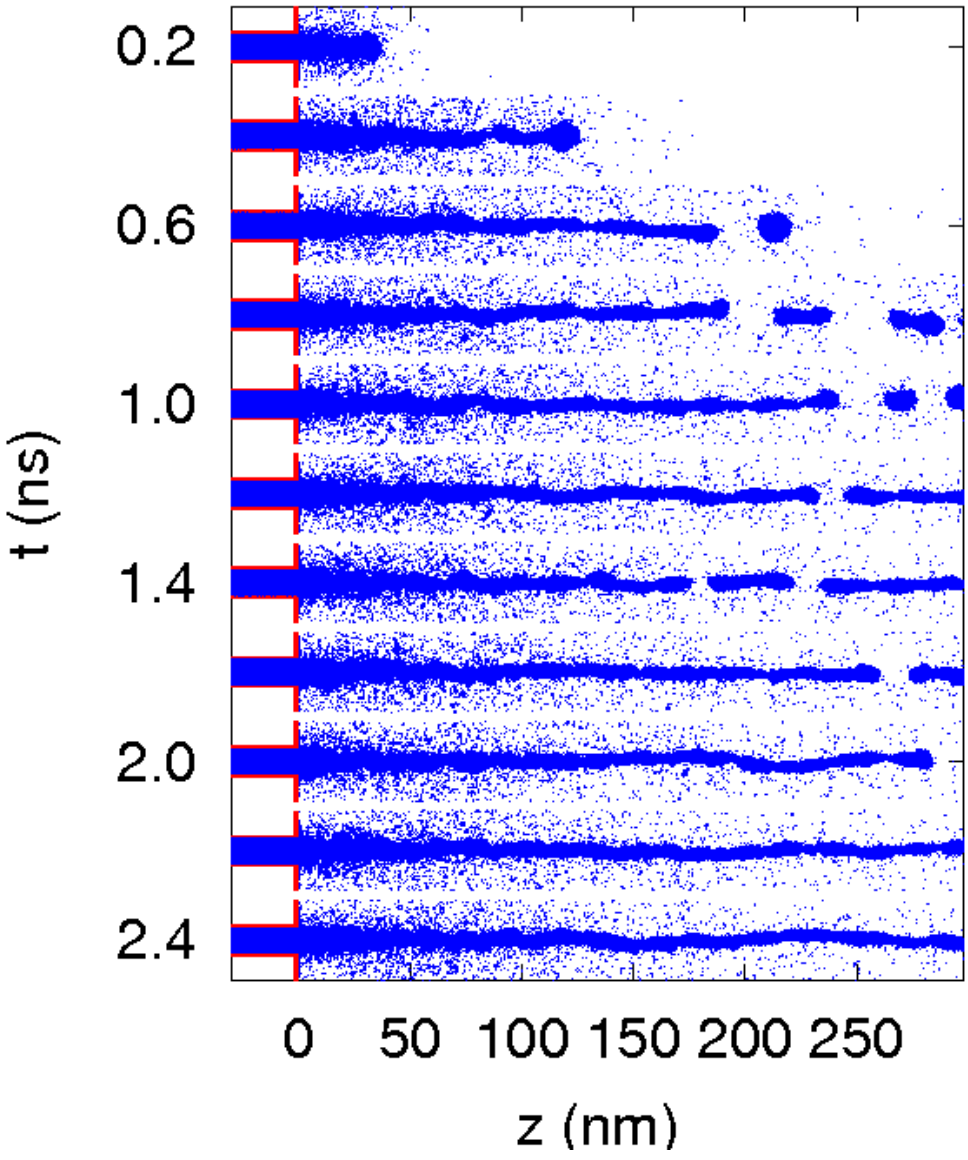


**Figure 23:** A typical propane nanojet emanating from a heated nozzle. The diameter of the nozzle is 12 nm and the nozzle is heated to 500 K. The pressure applied at the entrance of the nozzle is 220 MPa. Note that strong evaporations are observed near the exit of the nozzle. About 60 nm away from the nozzle, the diameter of the nanojet decreases to about half of the diameter of the nozzle.

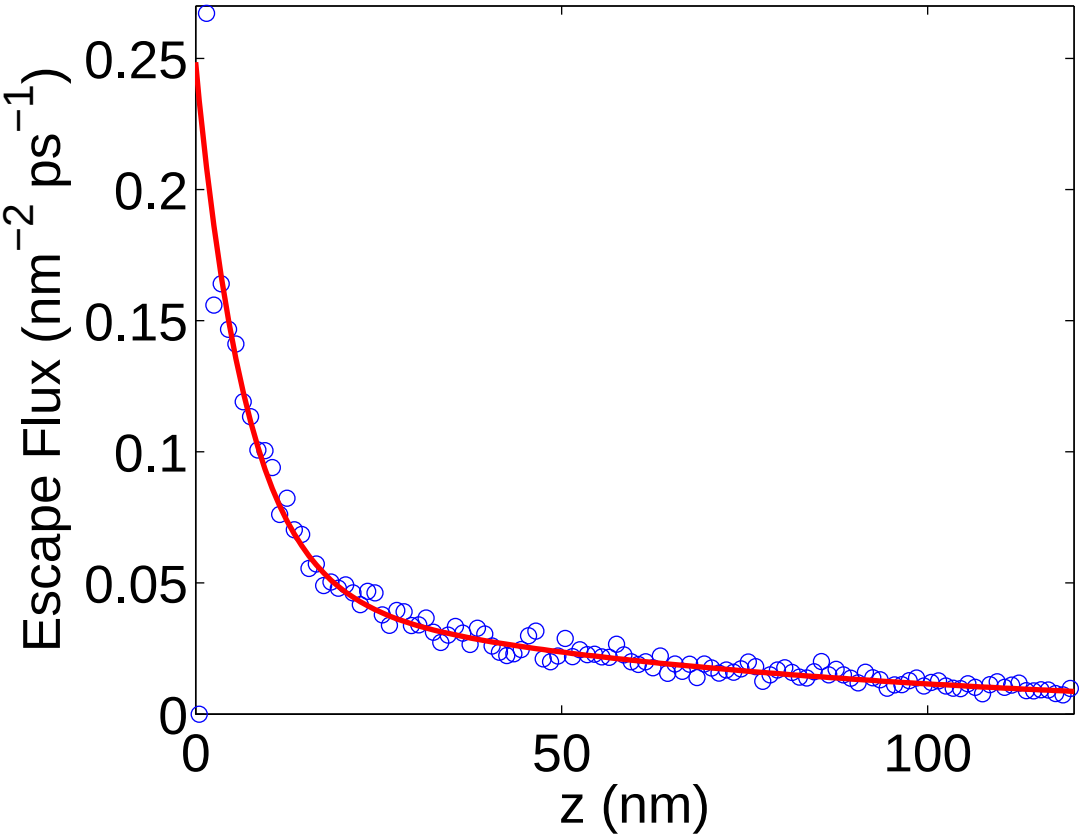


**Figure 24:** The escape flux as a function of the distance (from the nozzle) on a cylindrical surface of diameter 14 nm enveloping the nanojet. Hollow circles are measured from the molecular dynamics simulations and solid curve is the best fitting curve of Eq. (8.2), which is the sum of two exponential functions.

the function is expressed as,

$$R_{escape} = R_f \exp\left(-\frac{z}{l_f}\right) + R_s \exp\left(-\frac{z}{l_s}\right), \tag{8.2}$$

where, $R_f$ and $R_s$ represent the escape flux of a fast and a slow evaporation process respectively; and $l_f$ and $l_s$ are the characteristic length scales of these two processes. The best fitting curve (displayed as the solid curve in the figure) of the molecular dynamics simulation data (denoted as hollow circles) gives an escape flux function of $R_{escape} = 0.2\exp(-z/7) + 0.048\exp(-z/70)$, in a unit of nm$^{-2}$ ps$^{-1}$, with nm the unit of the distance. This result suggests the vaporization process of the nanojet be decomposed into two parts. The strong part (represented by the first term of $R_{escape}$)

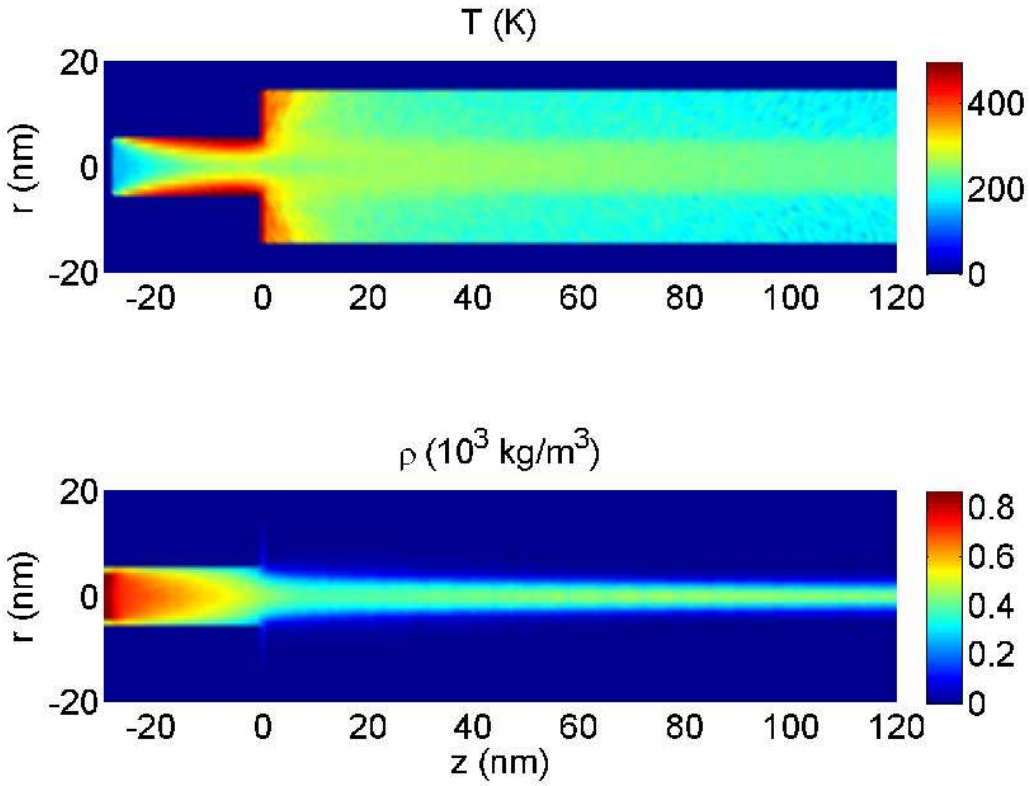


**Figure 25:** Temperature field and density distribution of the nanojet in the stationary state. The nozzle is placed at $z < 0$. The length of the nozzle is 30 nm and the diameter is 12 nm. The internal surface of the nozzle is heated to 500 K and a pressure of 220 MPa is applied to the nanojet. To obtain the figures, averages are performed in annular rings of 1 nm width and of 1 nm thickness.

decreases quickly. It describes the vaporization of the outer layer liquid of the nanojet at a temperature much higher than the boiling point of propane. The weak part (represented by the second term of $R_{escape}$) describes the process of evaporation of the liquid core whose temperature is lower than the boiling point. The evaporation of this part decreases at a slower rate. At a distance of 160 nm away from the nozzle, where the first part of $R_{escape}$ has already damped away, however, we can still observe the evaporation of the second part.

The temperature profile of the nanojet confirms the above descriptions. As shown

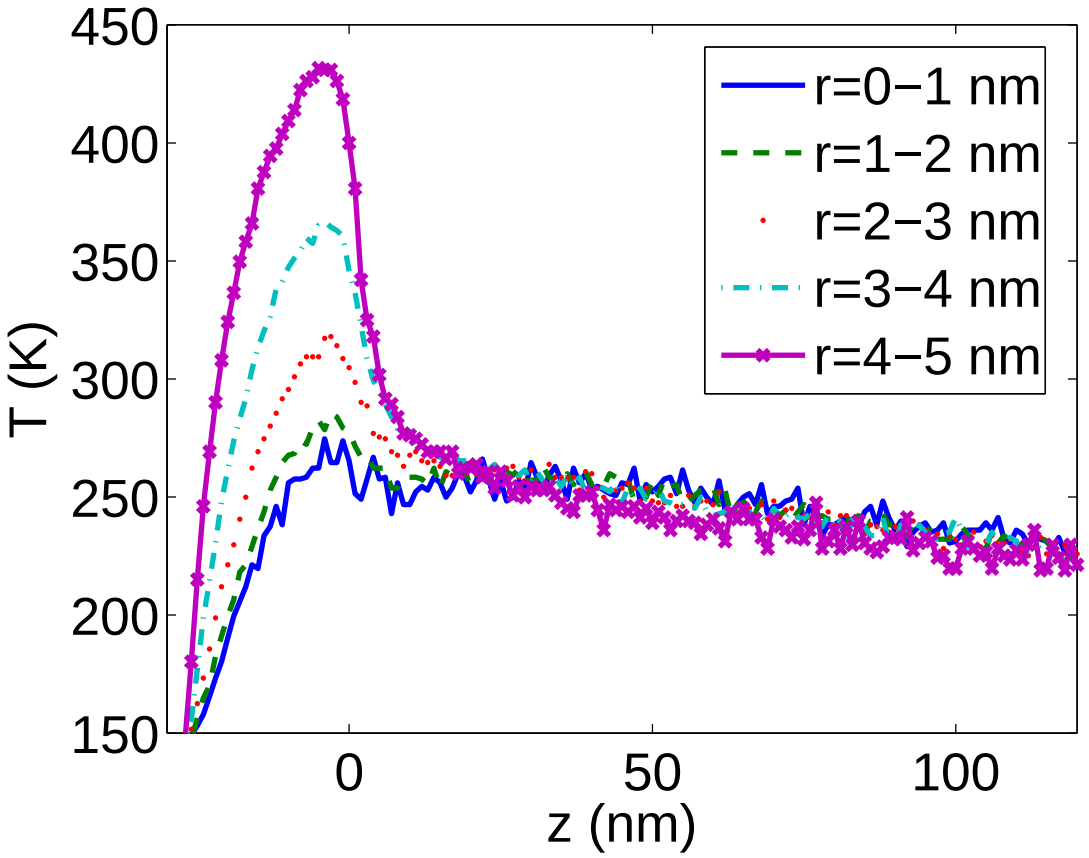


**Figure 26:** Average temperature of the nanojet as a function of the distance from the nozzle, which is placed at $z < 0$. The length of the nozzle is 30 nm and the disamter is 12 nm. The internal surface of the nozzle is heated to 500 K and a pressure of 220 MPa is applied to the nanojet. The average is performed in annular rings with a width of 1 nm and a thickness of 1 nm.

in the upper panel of Fig. 25 and in Fig. 26 for more details, the temperature of the outer layer of the nanojet decreases quickly in a short distance range in front of the nozzle, this implies a strong vaporization. Starting from about 20 nm away from the nozzle, the temperature of all the layers becomes uniform and it decreases with a speed much slower than before. The density profile, as displayed in the lower panel of Fig. 25 and Fig. 27, also shows a strong vaporization in the outer layers of the nanojet and a weak evaporation in the inner layer. For example, the density of the annular layer with its radius r between 4-5 nm decreases to near zero in a very short distance while the density of the layer between r= 2-3 nm is relatively a constant.

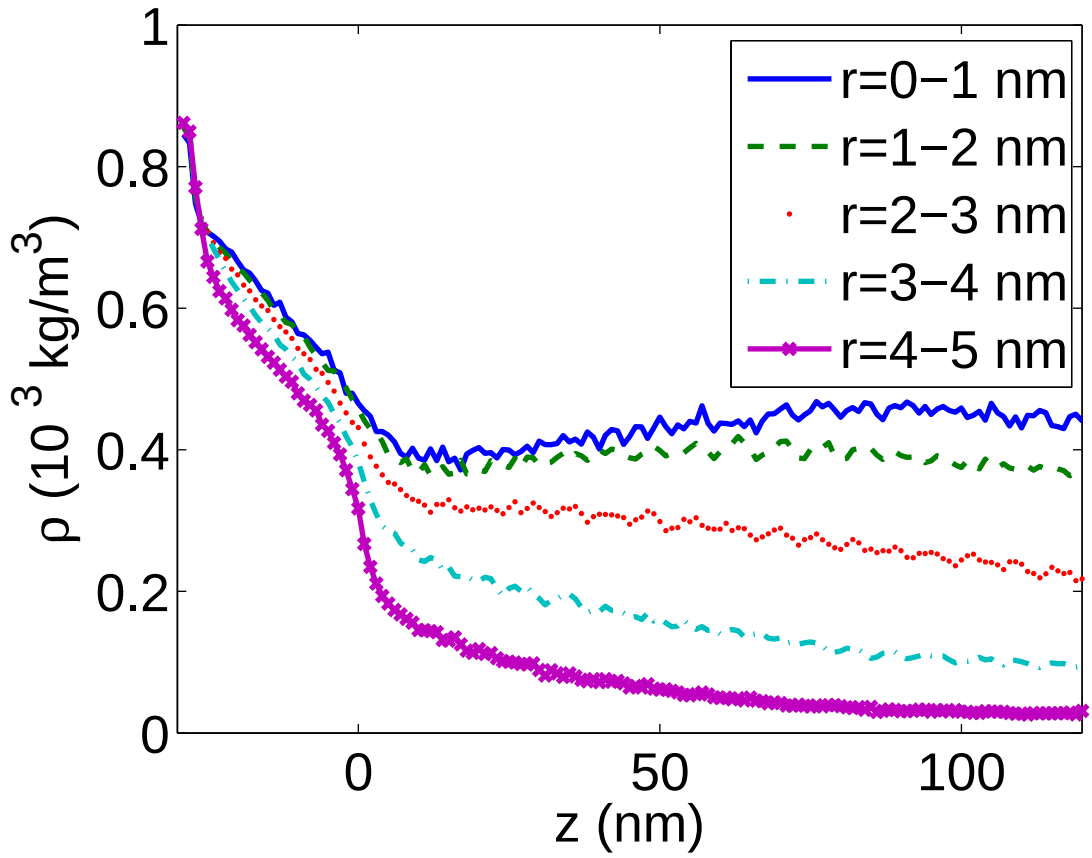


**Figure 27:** Average density of the nanojet as a function of the distance from the nozzle, which is placed at$z < 0$. The length of the nozzle is 30 nm and the disamter is 12 nm. The internal surface of the nozzle is heated to 500 K and a pressure of 220 MPa is applied to the nanojet. The average is performed in annular rings with a width of 1 nm and a thickness of 1 nm.

More interestingly, the density profile of the nanojet also shows a re-condensation process taking place in the core part of the nanojet. As displayed in Fig. 27, the density at the center of the nanojet (displayed as a solid curve) reaches its minimum value near the exit of the nozzle, and it recovers as the distance from the nozzle increases. This process is more clearly displayed in the lower panel of Fig. 25, where the formation of a core with higher density at the center of the nanojet can be observed as the distance increases. The re-condensation process suggests a rule of thumb to generate a nanojet through the heated-nozzle method, i.e., (1) keep the temperature of the propane liquid at a relatively low temperature when it enters the nozzle; and

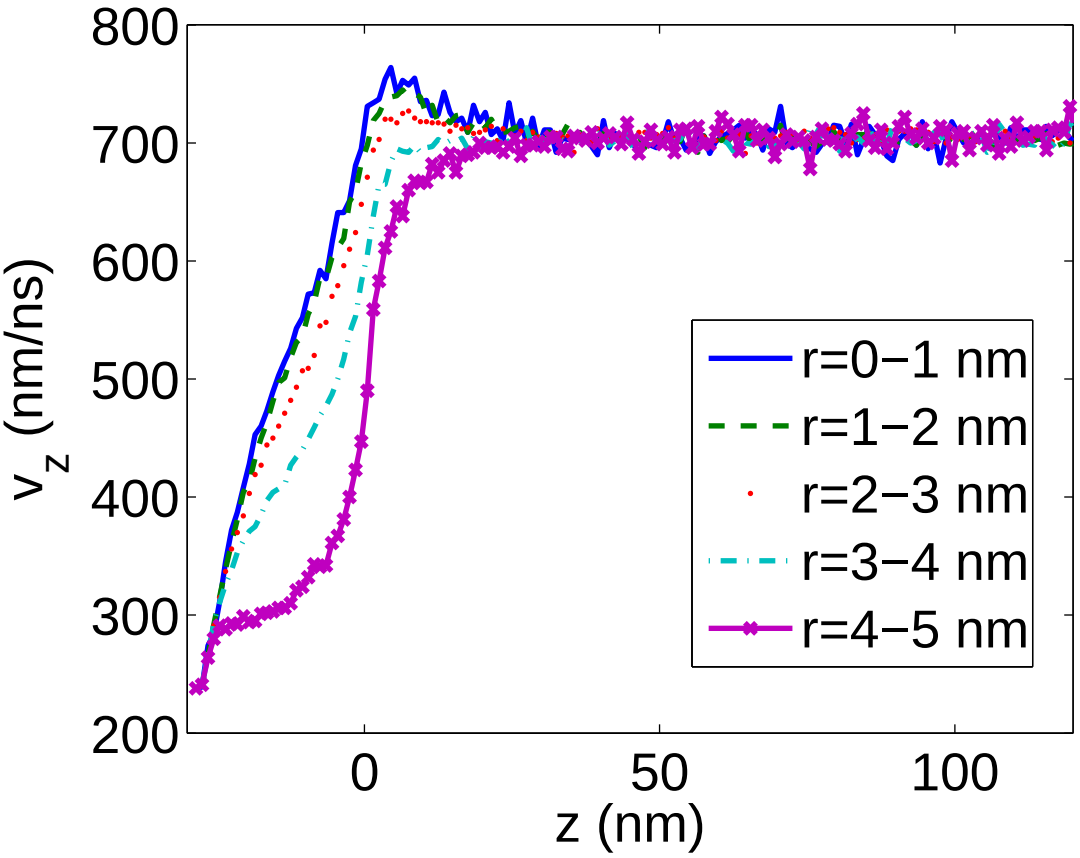


**Figure 28:** Average axial velocity of the nanojet as a function of the distance from the nozzle, which is placed at $z < 0$. The length of the nozzle is 30 nm and the diameter is 12 nm. The internal surface of the nozzle is heated to 500 K and a pressure of 220 MPa is applied to the nanojet. The average is performed in annular rings with a width of 1 nm and a thickness of 1 nm.

(2) heat the nozzle to a very high temperature as long as the nanojet has enough cold liquid core part when it leaves the nozzle.

With a straight cylindrical nozzle, the nanojet is sensitive to the fluctuations of the applied pressure. The fluctuations move as a wave packet along the nanojet and decreases the intact length [62] of the nanojet dramatically. Much effort has been spent on decreasing the pressure fluctuations and stabilizing the nanojet. In the simulations, this is achieved by assigning a large weight to the thermal reservoir [55], which decreases the amplitude of the pressure fluctuations effectively. In experiments, it corresponds to using a large liquid propane reservoir, since increasing the volume

of the propane liquid depresses the pressure fluctuations [48].

In Fig. 28, we show the axial velocity profile of the nanojet. The axial velocity of the nanojet reaches a constant value of about 700 nm/ns shortly after the nanojet leaves the nozzle, which means that the nanojet is in a stationary state. Note that in Fig. 28, the axial velocities of the nanojet inside the nozzle (the $z < 0$ region) increase monotonically, suggesting that a virtual convergent nozzle is formed inside the real nozzle automatically. Actually, the self-convergence of the nanojet from a heated nozzle is also reflected in other important properties besides the axial velocity profile. For example, in Fig. 25, both the temperature and density distributions of the nanojet inside the real nozzle display a self-convergent pattern. It suggests that the virtual self-convergent nozzle inside the heated real nozzle is a concrete idea that captures the essence of the process. To obtain a quantitative description and extend our prediction ability to a length scale beyond the capacity of molecular dynamics simulation methods, the formation of such virtual self-convergent nozzles is modeled using continuum hydrodynamic formulas as follows.

## *8.4 Modeling of the virtual self-convergent nozzle*

The self-convergence effect emerged in a propane nanojet emanating from a heated nozzle can be captured by a simple continuum hydrodynamic model, despite that direct numerical integration of the equation of motion inside the nozzle turns out to be very difficult. The physical properties, in particular the density and the phases, of the propane flow vary in a broad range as the pressure inside the nozzle decreases from 220 MPa to almost 0 MPa and the flow is heated from 150 K (in the reservoir) to 500 K (close to the internal wall of the nozzle). These two factors together make most of the commonly used numerical integration methods for the hydrodynamic equations of motion extremely unstable. However, with the help of molecular dynamics simulations of the flow inside the nozzle, we can simplify the hydrodynamic equation of motion

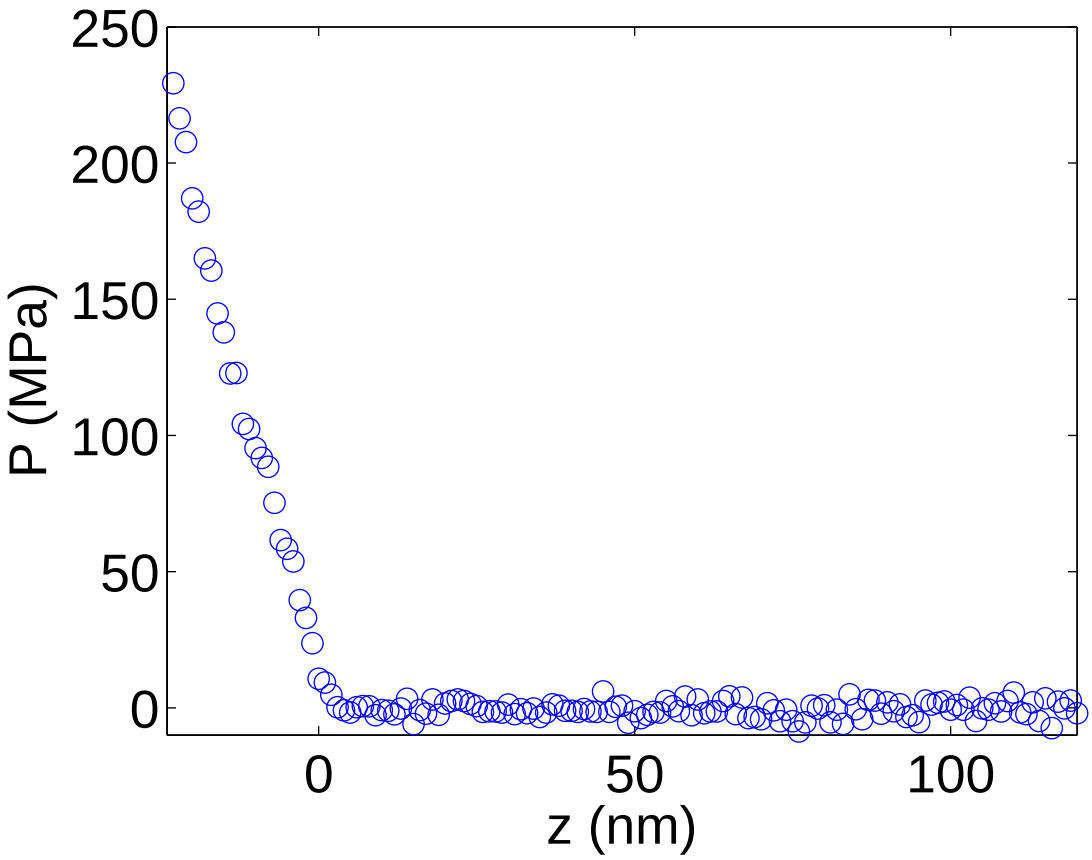


**Figure 29:** The pressure of the propane nanojet as a function of z, obtained from the molecular dynamics simulation, where the position of the nozzle is $z < 0$. It shows that the pressure change inside the nozzle can be well depicted by a linear function of z.

through reasonable approximations and obtain a fairly good continuum description of the self-convergence effect.

In the continuum model the boundary conditions and initial conditions of the nanojet inside the nozzle are kept the same as those in the molecular dynamics simulations (see Fig. 22 for details), i.e., the length of the nozzle is 30 nm and its diameter is 12 nm; the temperature of the nozzle is 500 K; and from the left end of the nozzle, where the local pressure is 220 MPa, a propane flow with a velocity of 250 nm/ns and a temperature of 150 K enters the nozzle. At the right exit of the nozzle, the pressure of the propane flow decreases to nearly 0.

Generally, the flow inside the nozzle is governed by the Navier-Stokes equations [62, 48]. With the axial symmetry of the flow, the equations are expressed in the cylindrical coordinates as [62, 48],

$$\frac{\partial u_r}{\partial t} + u_r \frac{\partial u_r}{\partial r} + u_z \frac{\partial u_r}{\partial z} = -\frac{1}{\rho}\frac{\partial p}{\partial r} + \nu \left\{ \frac{\partial}{\partial r}\left[\frac{1}{r}\frac{\partial}{\partial r}(r u_r)\right] + \frac{\partial^2 u_r}{\partial z^2} \right\}, \tag{8.3}$$

and

$$\frac{\partial u_z}{\partial t} + u_r \frac{\partial u_z}{\partial r} + u_z \frac{\partial u_z}{\partial z} = -\frac{1}{\rho}\frac{\partial p}{\partial z} + \nu \left[\frac{1}{r}\frac{\partial}{\partial r}\left(r\frac{\partial u_z}{\partial r}\right) + \frac{\partial^2 u_z}{\partial z^2}\right], \tag{8.4}$$

where ur and $u_r$, $u_z$ are the $r$, $z$ components of the velocity field respectively; $\rho$ is the density of the flow; $p$ is the local pressure; and $\nu$ is the kinematical viscosity of the flow, defined as the ratio of the viscosity $\mu$ to the density $\rho$. Usually, $\nu$ is a function of the local pressure $p$ and the local temperature $T$ of the propane flow; however, to simplify the problem, a constant effective kinematical viscosity $\nu = 2.8\times10^2$ nm$^2$/ns is used in the model. From the molecular dynamics simulations, we find that (as shown in Fig. 29) the pressure inside the nozzle is well described by a linear function of $z$, i.e., $\partial p/\partial r$ is 0 and $\partial p/\partial z$ is a constant. Note that these two conditions pertaining to the pressure are used as known conditions in our model. It is distinguished from the usual computational fluid dynamics (CFD) calculations[36, 13], where the pressure field $p(z, r, t)$ is an unknown variable in the equation of motion; and this is one of the major approximations of our continuum model, which simplifies the problem dramatically.

In our model, the variations in the energy density of the flow are depicted using the temperature field instead of the full energy conservation equations. The equation for the change of the temperature field, denoted as $T$, is

$$\frac{\partial T}{\partial t} + u_r \frac{\partial T}{\partial r} + u_z \frac{\partial T}{\partial z} = \kappa \left[\frac{1}{r}\frac{\partial}{\partial r}\left(r\frac{\partial T}{\partial r}\right) + \frac{\partial^2 T}{\partial z^2}\right], \tag{8.5}$$

where $\kappa$ is the thermometric conductivity of the fluid. Molecular dynamics simulations show that the temperature gradient of the propane flow is about 50 K/nm from the

internal wall of the nozzle to the center of the flow. Such a large temperature gradient implies that the variation of the flow's total energy is mainly the result of heat transfer. Besides, since the flow is confined in the nozzle, the volume change is small and therefore thermal expansion of the liquid accounts for a small fraction of the change of the flow s total energy. All these facts support that the change of the temperature field of the flow is a reasonable approximation to the total energy change. We also notice that the model can be further simplified by adopting a constant thermometric conductivity of $\kappa = 1.01\times10^2$ nm$^2$/ns.

The flow is also determined by the equation of state of the material (in our case, propane) inside the nozzle. In some parts of the flow inside the nozzle, the propane is under such a high pressure (over 200 MPa) that experimental data are not available. It is convenient for us to get an approximate equation of state for propane from the molecular dynamics simulation data. For the pressure and temperature range encountered in the modelling, the following simple equation of state turns out to work well. The equation of state for propane,

$$\rho(p,t) = \left[\rho_0 - \alpha\left(1 - \frac{p}{p_0}\right)\right]\left[1 - \beta(T - T_0)\right], \tag{8.6}$$

is an equation of density $\rho$, pressure $p$, and temperature $T$; where, $\rho_0(p_0, T_0)$ is a reference point in the phase space for the linear equation of state, and $\alpha$ and $\beta$ are baric and thermal coefficients respectively. In our model the reference point is $p_0 =$ 220 MPa, $T_0 = 150$ K, and $\rho_0 = 0.72\times10^3$ kg/m$^3$. The coefficients are $\alpha = 0.19\times10^3$ kg/m$^3$ and $\beta = 1.2\times10^{-3}$ K$^{-1}$.

Since we have assumed that the pressure is known *a priori*, Eqs. (8.3-8.6) form a complete set of equations with respect to variables $u_z$, $u_r$, $T$ and $\rho$. Note that the continuity equation,

$$\frac{\partial\rho}{\partial t} + \frac{1}{r}\frac{\partial}{\partial r}(r\rho u_r) + \frac{\partial}{\partial z}(\partial\rho u_z) = 0, \tag{8.7}$$

is only used as an auxiliary equation to gauge the performance of the approximations

in the continuum model.

Besides the aforementioned boundary conditions, to make the model a well-posed problem, we still need to know how fast the flow moves on the internal wall of the nozzle, or, in another word, how sticking the wall is. The molecular dynamics simulation shows that the wall is entirely non-sticking after a short transient distance, i.e., the velocity on the wall decreases from 250 nm/ns to 150 nm/ns in a transient distance of 2-3 nm and remains a constant after that. In our model, we simply ignore the short transient distance and assume the velocity of the flow on the internal wall of the nozzle along the surface with a magnitude of 150 nm/ns.

In principle, as indicated by the molecular dynamics simulations, the flow inside the nozzle forms a stationary state after a transient period. Though it is more sophisticated to solve the stationary problem using some relaxation methods, keeping the time partial derivatives in Eqs. (8.3-8.6) does not change the final stationary state of the flow. It only decreases the complexity of the numerical algorithm.

The model is solved using a finite difference numerical method [36, 13] on a regular 30×12 grid network. The entire volume in the nozzle is divided into 30 grid points along the axial direction ($z$ direction), and 12 grid points along the radial direction. In order to make the time integration of Eqs. (8.3-8.6) convergent, the Maccormack s technique [36, 13] is employed with a small time step of 1.0 fs. The numerical solutions of $u_z$, $u_r$, $T$ and $\rho$ are displayed in Fig. 30 and Fig. 31 (left columns), compared with their counterparts obtained from molecular dynamics simulations (right columns). They show that the quantities obtained from the continuum model are very close to the molecular dynamics simulation results, except in some places near the internal wall or the left entrance of the nozzle, where the shapes of the curves obtained by the two methods differ slightly. This implies that our simple continuum model captures the main picture of the nanojet in the heated nozzle and we have a simple way to predict the self-convergent effect inside it. As displayed in Fig. 31(left of the first row), the

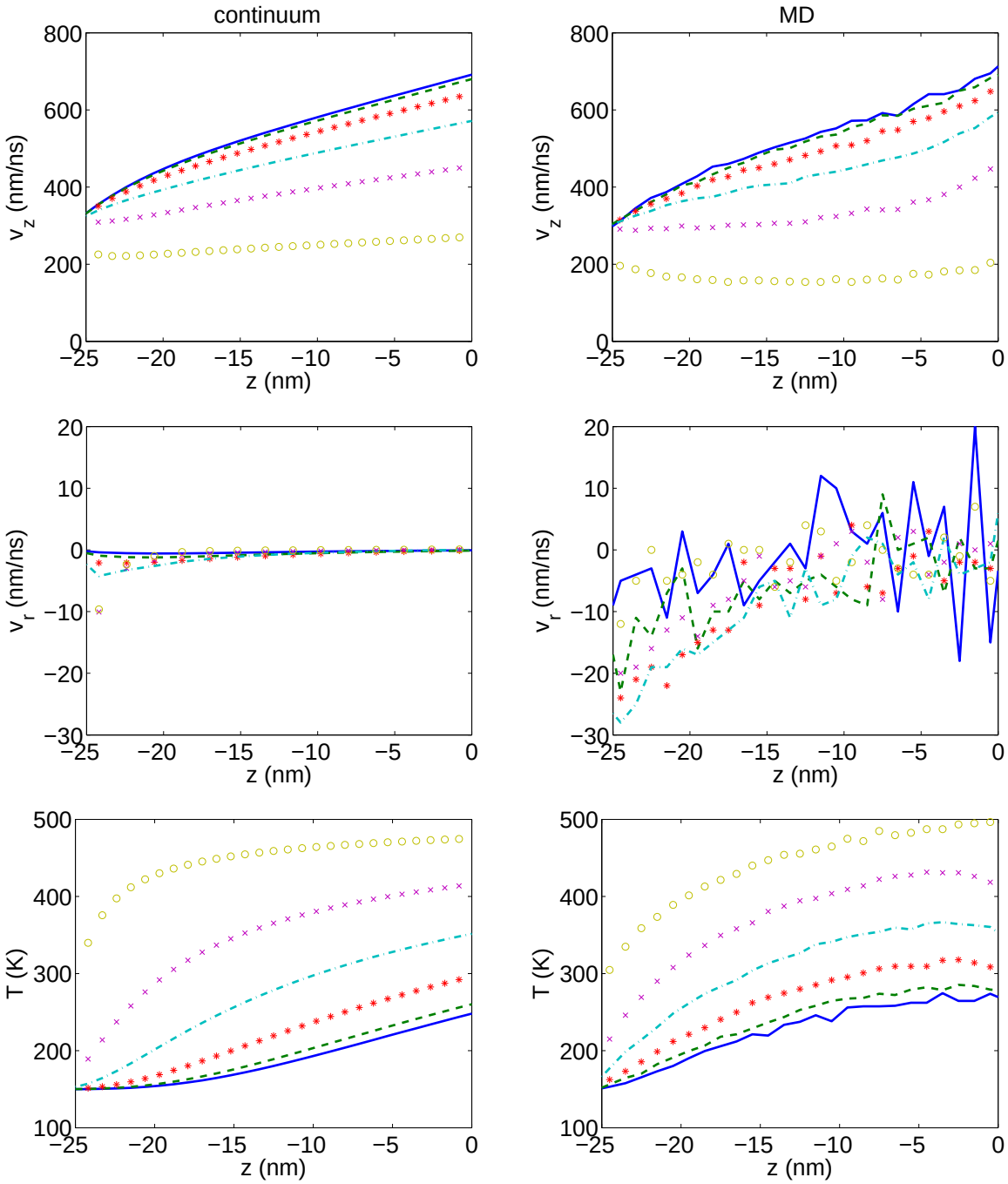


**Figure 30:** The comparison of the numerical integration of the continuum model and the molecular dynamics simulation results. The left column is the numerical results and the right column is the molecular dynamics results. The (blue) solid curve is the average value in a center disk of radius r = 1 nm; the (green) dashed curve is the value on the ring of r = 1 - 2 nm; the (red) asterisk curve is the value on the ring of r = 2 - 3 nm; the (sky blue) dash-dot curve is the value on the ring of r = 3 - 4 nm; the (purple) cross curve is for the ring of r = 4 - 5 nm; and the (yellow) hollow-circle curve is for the ring of r = 5 - 6 nm.

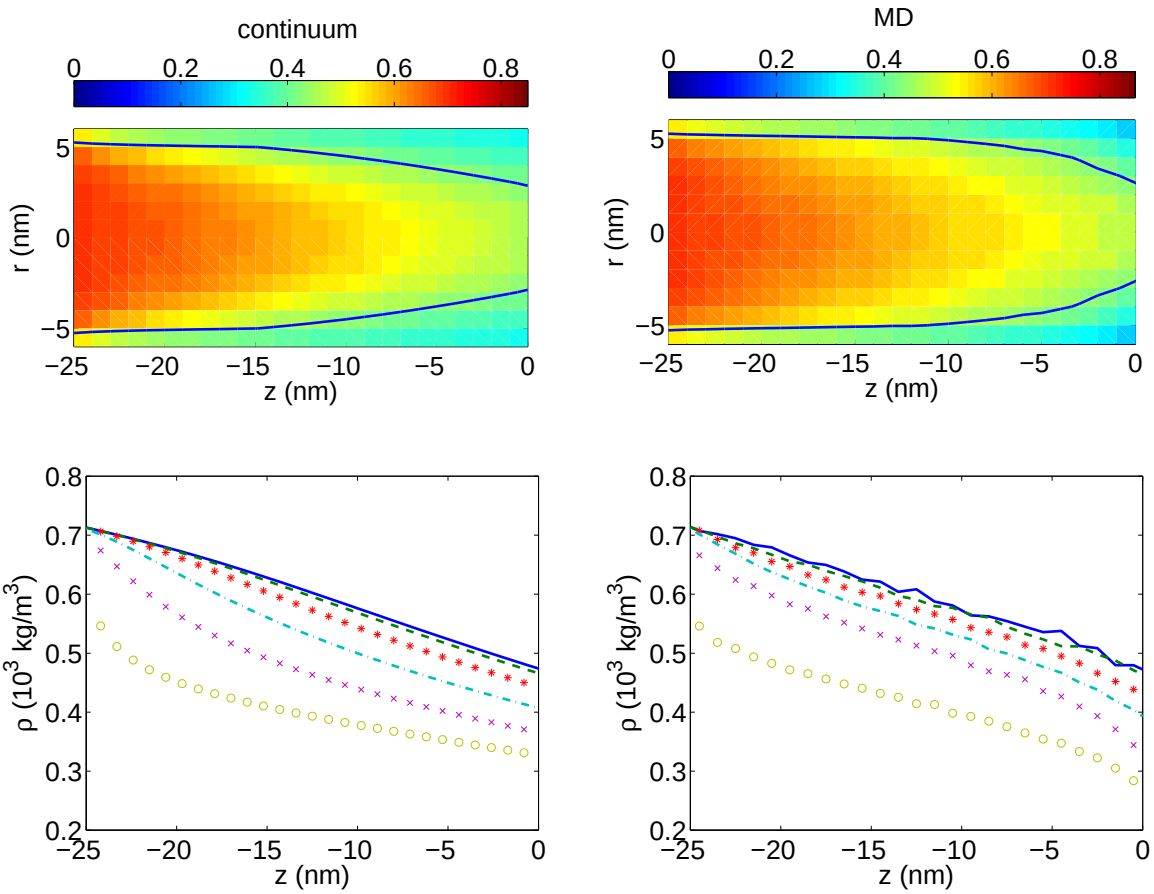


**Figure 31:** The density profile of propane inside the heated nozzle. The left column is obtained from numerical solution of the continuum model, while the right column is obtained from molecular dynamics simulations. The first row is the color density distribution, where the unit of the density is $10^3$ kg/m$^3$. The (blue) solid curves are the contour lines of the density $0.4\times10^3$ kg/m$^3$, they show explicitly the shape of the virtual convergent nozzle. The second row is the average density profile in annular rings. The meaning of the symbols is the same as in Fig. 30.

density distribution of propane inside the nozzle is depicted in colors. The high density region is concentrated in the center part of the nozzle, forming a virtual cone. To highlight the shape of the virtual cone, the contour lines for the density of $\rho$=$0.4\times10^3$ kg/m$^3$ are plotted in the same figure in blue solid curves. Note that the average density of the core of the nanojet outside of the nozzle is about $\rho$=$0.4\times10^3$ kg/m$^3$, as displayed in Fig. 27. It is reasonable to use this particular density as a criterion to determine the boundary of the virtual self-convergent nozzle. We can double check

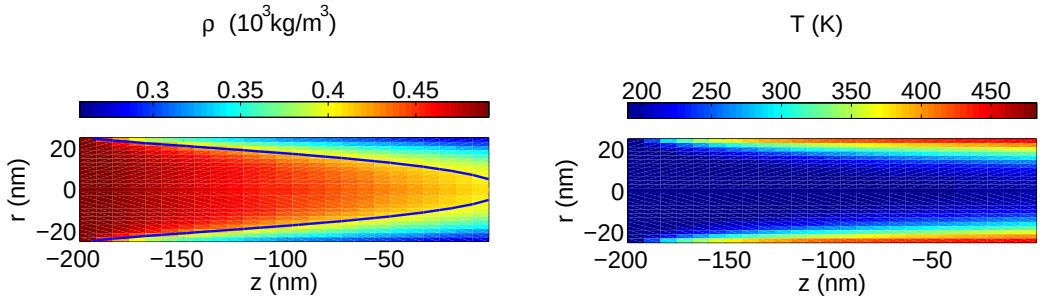


**Figure 32:** Density profile and temperature distribution of a nanojet in a nozzle with a diameter of 58 nm and a length of 200 nm. The figures are obtained from the numerical integration of the continuum hydrodynamics model newly devised for the virtual self-convergent nozzle. The upper panel is the density profile of the propane nanojet inside the nozzle. The unit of the density is $10^3$ kg/m$^3$. The shape of the virtual nozzle, which has a convergent exit of 14 nm diameter, is illustrated by the contour surface of the density $0.4\times10^3$ kg/m$^3$ (blue curves) in the figure. The lower panel is the temperature distribution of the propane nanojet inside the nozzle. The unit of the temperature is K. Note that the exit of the nozzle is located at z = 0.

the prediction of the convergence effect by comparing the density distribution with the molecular dynamics simulation result, which is also displayed in Fig. 31 (right of the first row). It turns out that they agree with each other very well.

The success of the continuum model enables us to predict the shape of virtual self-convergent nozzles on a much larger length scale. In Fig. 32, we show a virtual self-convergent nozzle of 58 nm diameter using our continuum model. The length of the real nozzle is 200 nm and the pressure applied at the entrance of the nozzle is 100 MPa. To decrease the length of the nozzle, the temperature of the propane nanojet at the entrance of the nozzle is 190 K. The other boundary conditions and parameters are kept the same as those in the simulation with a 12 nm-diameter nozzle. The new continuum model is solved on a $25\times14$ grid using a time step of 0.1 ps.

The resulting nanojet obtains an exit velocity of 460 nm/ns, and the virtual nozzle has a convergent exit of 14 nm diameter, as displayed in the upper panel of Fig. 32. The shape of the virtual nozzle is shown by the blue curves in the figure.

The lower panel of Fig. 32 shows the temperature distribution of the propane nanojet inside the nozzle. Compared with the hot outer layer, the core of the nanojet keeps a temperature about 200 K, which is still below the boiling point of propane. Therefore, injected form the exit of the nozzle, a nanojet will be generated with approximately the same diameter as the exit of the virtual convergent nozzle. Similar results have already been displayed in the previous molecular dynamics simulation of the nanojet from a heated nozzle of 12 nm diameter.

## *8.5 Control of a nanojet by adjusting the nozzle's temperature distribution*

The control of a nanojet generated through the heated nozzle method can be easily realized by changing the temperature pattern on the internal wall of the nozzle. Here, we demonstrate this method using molecular dynamics simulations with a simple temperature pattern, i.e., the upper and lower parts of the nozzle have different temperatures. Fig. 33 displays the deflection of a nanojet, where the temperature of the upper part and the lower part of the nozzle is 300 K and 600 K respectively. The shape of the nozzle and the driving pressure are the same as in the previous molecular dynamics simulations.

As displayed in Fig. 33, the nanojet responds promptly to the temperature change. It takes only about 1 ns for the deflected nanojet to reach its stationary state. When the temperature of the upper part of the nozzle is fixed at 300 K and the temperature of the lower part varies in the range of 500 K to 700 K, the nanojet always bends toward the direction of lower temperature. The deflection angle, measured as the angle between the main stream of the nanojet and the z axis (the symmetrical axis of the nozzle), increases monotonically from $3.08^o$ to $4.95^o$ as the temperature of the lower part of the nozzle changes from 500 K to 700 K.

The deflection of the nanojet results from the shape change of the virtual convergent nozzle and the strong evaporation of the outer layer of the nanojet at the exit

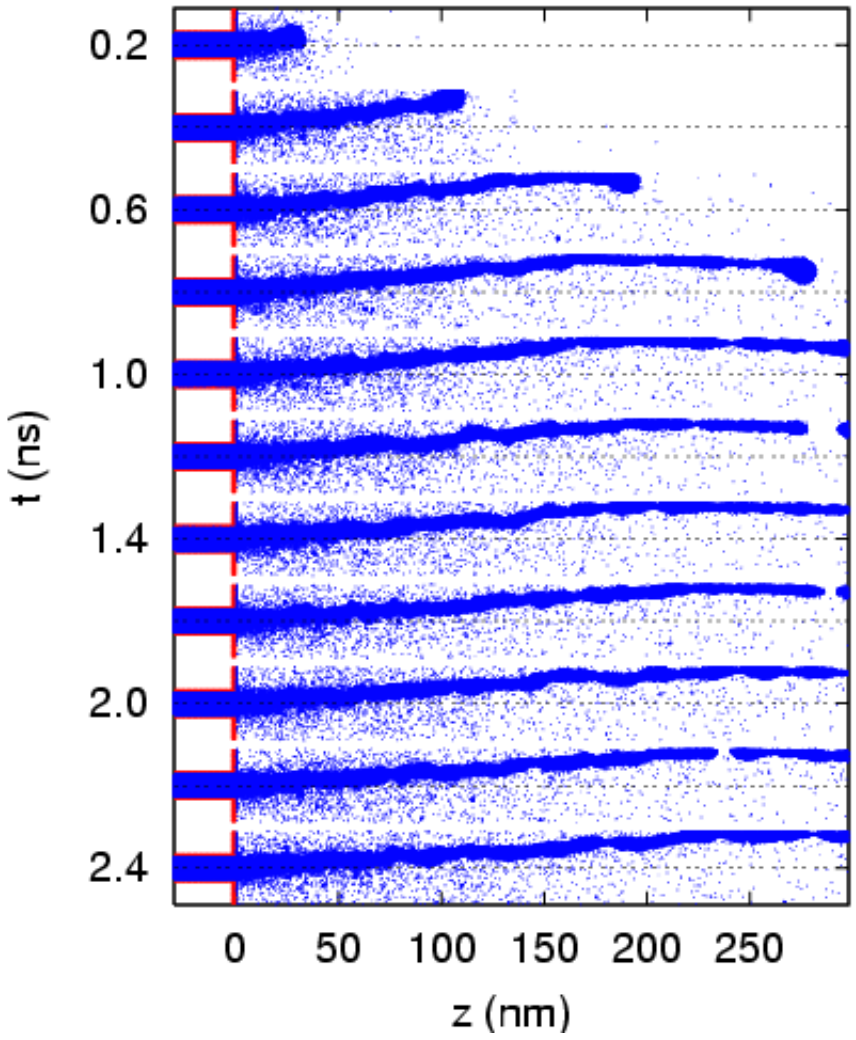


**Figure 33:** A typical deflection sequence of a nanojet from a nozzle with a temperature difference. The temperature of the upper half of the nozzle is 300 K, while the temperature of the lower half is 600 K. The diameter of the nozzle is 12 nm and the pressure applied at the entrance of the nozzle is 220 MPa. The dashed lines in the figure are the symmetrical axes of the nozzle.

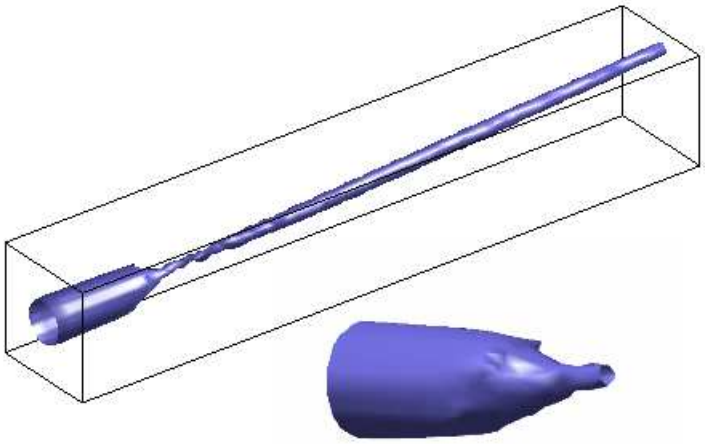

**Figure 34:** The density contour surface of $\rho = 0.4\times10^3$ kg/m$^3$ of the deflected nanojet described in Fig. 33. The dimension of the frame in the upper panel is 30 nm $\times$ 30 nm $\times$ 190 nm. The lower panel is the enlargement of the contour surface inside the nozzle. It shows the shape of the virtual nozzle, which is not cylindrically symmetrical.

of the nozzle. The shape change of the virtual convergent nozzle takes place inside the real nozzle. Fig. 34 displays the nanojet's density contour surface of $\rho$=$0.4\times10^3$ kg/m$^3$. The enlargement of the contour surface inside the nozzle clearly shows the shape change of the virtual convergent nozzle, i.e., the exit of the virtual convergent nozzle has a small angle with the symmetrical axis (z axis) of the real nozzle. Another evidence for the symmetry break of the virtual nozzle is the density contour of the propane nanojet at the exit of the nozzle. As displayed in Fig. 35, the center of mass of the propane nanojet favors the direction of lower temperature. The corresponding temperature profile of the same transversal intersection (at the exit of the nozzle) is plotted in Fig. 36 as a reference.

However, the shape change of the virtual convergent nozzle itself is not enough to account for the deflection of the nanojet. As displayed in Fig. 37, the displacement

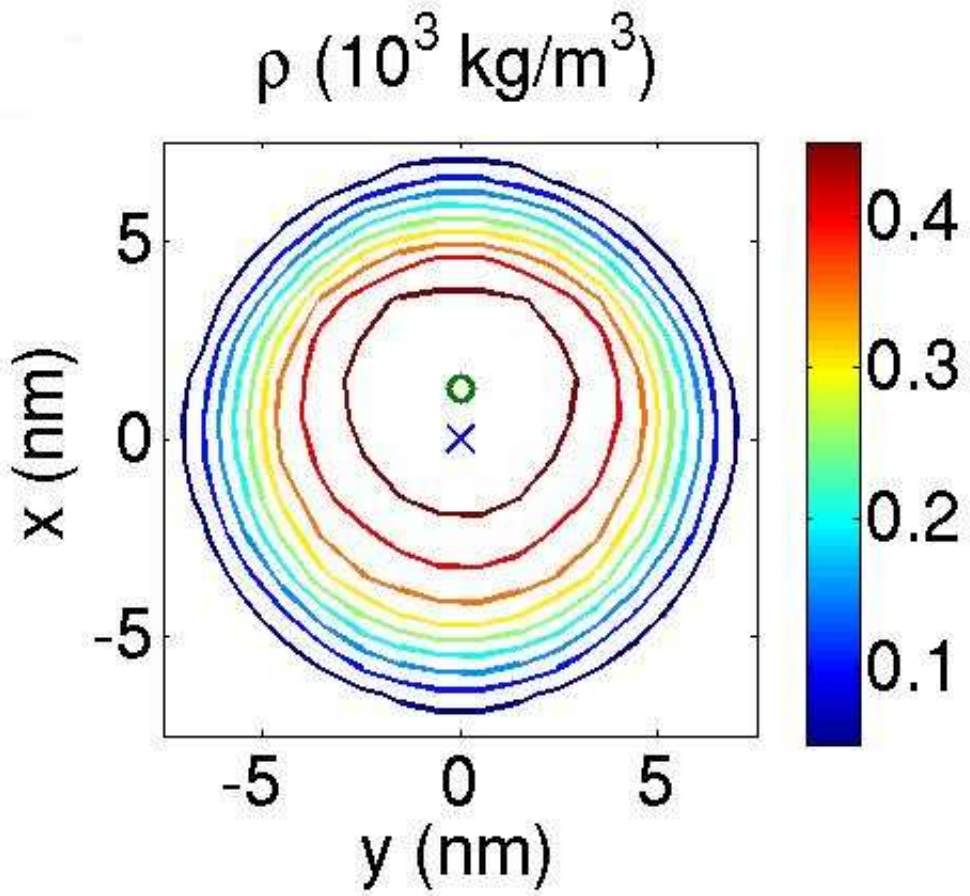


**Figure 35:** The density contour of the deflected propane nanojet described in Fig. 33 at the exit of the nozzle. The unit of the density here is $10^3$ kg/m$^3$. It shows the breakup of the symmetry. The center of mass of the nanojet favors the location of lower temperature (the x>0 part).

of the center of mass of the nanojet in the direction (denoted as x) in which the temperature of the nanojet has a gradient, is less than 0.5 nm from the symmetrical axis z (blue circle curve in the figure) inside the nozzle (the $z < 0$ part). The transversal velocity of the nanojet's center of mass is 9.8 nm/ns at the exit of the nozzle, as displayed by the blue circle curve in Fig. 38. Note that the axial velocity of the nanojet is 700 nm/ns, the deflection angle thus formed is about $0.8^o$, which is much smaller than the value measured in simulations.

Fig. 38 shows that at the vicinity of the exit of the nozzle, the transversal velocity of the nanojet's center of mass is boosted in a very short distance from 9.8 nm/ns

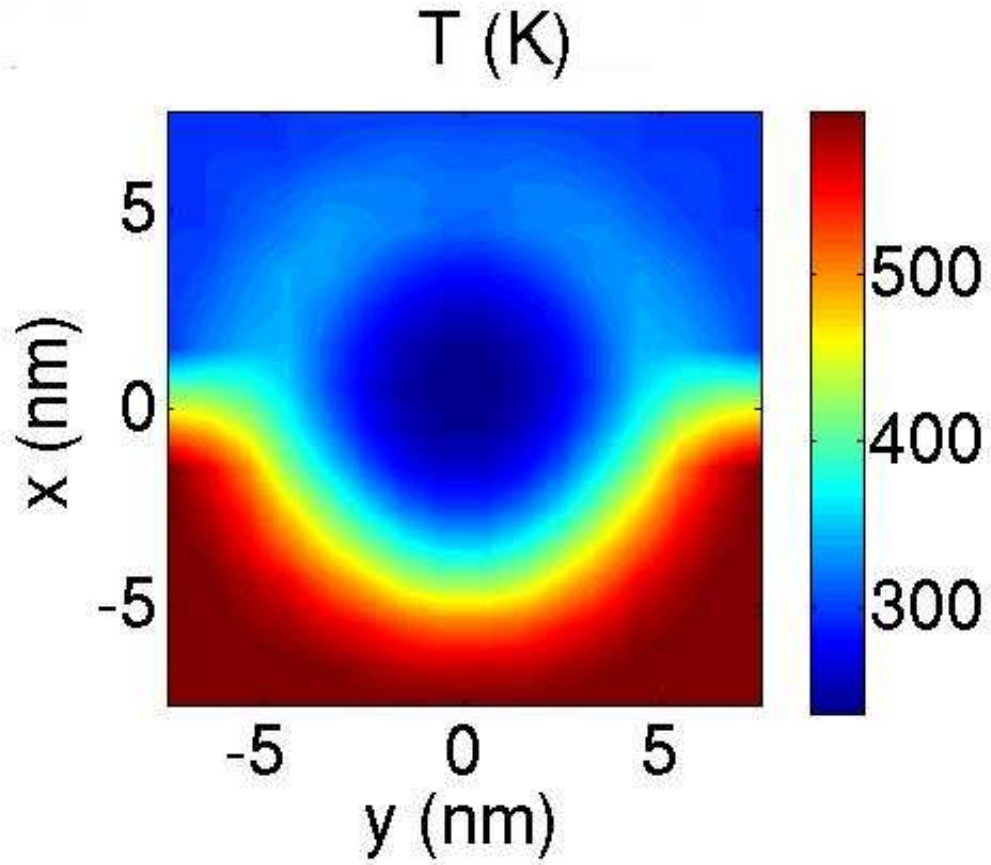


**Figure 36:** The temperature distribution of the deflected nanojet described in Fig. 33 at the exit of the nozzle. The unit of the temperature is K.

to about 45 nm/ns. This change is also reflected in Fig. 37 as that the slope of the displacement curve (blue circle curve) of the nanojet's center of mass increases abruptly at the exit of the nozzle. The increase of the velocity can only attributed to the strong evaporation at the exit of the nozzle. Because the temperature of the lower half of the nanojet inside the nozzle is higher than that of the upper half, as displayed in Fig. 36, the average speed of the gaseous propane molecules in the lower part is larger than in the upper part. Since the total momentum in the transversal plane is conserved, after the gaseous propane is evaporated the liquid core of the nanojet yields a velocity pointing to the direction of lower temperature and the nanojet bends upwards, as in Fig. 33.

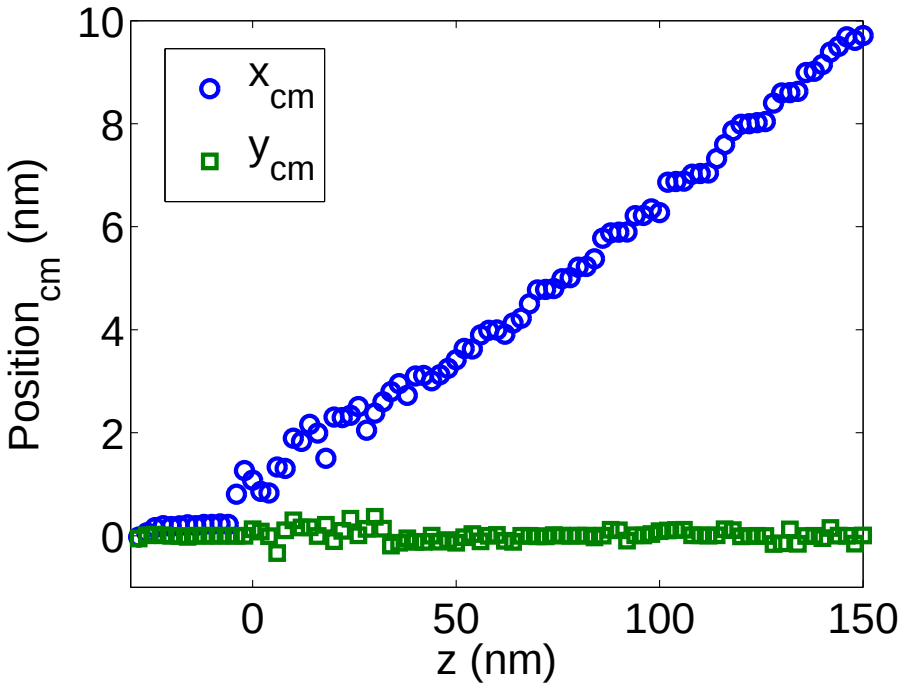


**Figure 37:** The displacement of the center of mass of the deflected nanojet described in Fig. 33. The blue circle curve is the displacement in the x direction, while the green square curve is the displacement in the y direction. Both the x and y direction are perpendicular to the symmetrical axis of the nozzle and they are perpendicular to each other. Note that the exit of the nozzle lies at z = 0.

Though the evaporation process contributes 3/4 to 4/5 of the velocity of the nanojet's center of mass, it should be noticed that the evaporation process itself cannot deflect the nanojet without the shape change of the virtual nozzle and the temperature difference. In this case, the shape change process of the virtual nozzle initializes the deflection of the nanojet and the deflection is boosted by the evaporation at the exit of the nozzle because of the temperature difference.

## *8.6 Summary*

In summary, we propose a heated-nozzle technique to generate nanojets from a nozzle of much larger diameter. Large scale molecular dynamics simulations show that the technique can effectively decrease the diameter of a nanojet and reduce the threshold pressure to generate a nanojet. The heated nozzle method also solves the problem

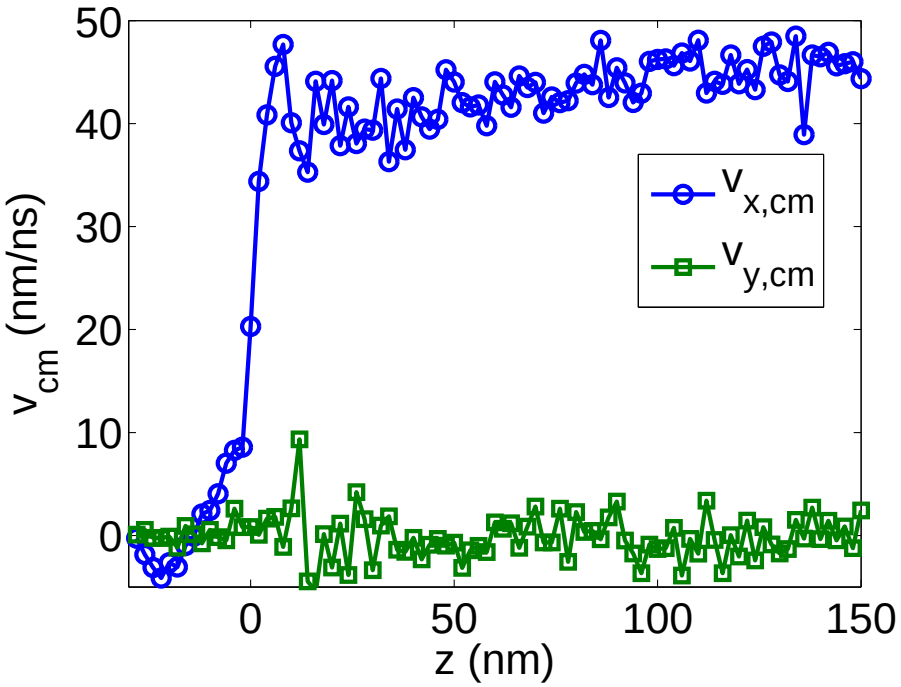


**Figure 38:** The transverse velocity components of the center of mass of the deflected nanojet described in Fig. 33. The blue curve (circles) is the velocity component along the x direction and the green one (squares) is the velocity component in the y direction. Note that the exit of the nozzle lies at z = 0.

of jamming due to fluid molecules' buildup on the nozzle's exterior. Inside the real nozzle, a virtual self-convergent nozzle is formed automatically by the flow itself. The formation of the virtual self-convergent nozzle is captured by a simple continuum hydrodynamic model. Numerical integration of the continuum model yields results close to the molecular dynamics simulations. With the help of the continuum hydrodynamic model, we can predict the generation of self-convergent nozzles on a much larger length scale.

It is also demonstrated through molecular dynamics simulations that the control of the direction of the nanojet can be realized by adjusting the temperature pattern of the external nozzle. In a word, the heated-nozzle technique we propose provides an experimentally promising method that can both generate and control a nanojet in an easy way.

# REFERENCES


[1] A.-L. Barabasi, H. E. S., *Fractal concepts in surface growth*. Cambridge, UK: Cambridge University.

[2] A. V. Prinz, V. Ya. Prinz, V. A. S. *Microelectron. Eng.*, vol. **67/68**, p. 782, 2003.

[3] Alper, J. *Science*, vol. **305**, p. 1895, 2004.

[4] Alper, J. *Science*, vol. 305, p. 1895, 2004.

[5] B. J. Alder, T. E. W. *J. Chem. Phys.*, vol. **27**, p. 1208, 1957.

[6] B. J. Alder, T. E. W. *J. Chem. Phys.*, vol. **31**, p. 459, 1959.

[7] B. Smit, S. Karaborni, J. I. S. *J. Chem. Phys.*, vol. **102**, p. 2126, 1995.

[8] Barenblatt, G. I., *Scaling, self-similarity, and intermediate asymptotics*. Cambridge, UK: Cambridge University.

[9] Chandrasekhar, S., *Hydrodynamic and Hydromagnetic Stability*. Oxford, UK: Oxford University.

[10] D. Frenkel, B. S., *Unerstanding molecular simulation: from algorithms to applications*. San Diego: Academic.

[11] D. H. Peregrine, G. Shoker, A. S. *J. Fluid Mech.*, vol. **212**, p. 25, 1990.

[12] D. Huang, Y. Chen, K. A. F. *J. Chem. Phys.*, vol. **101**, p. 11021, 1994.

[13] Dale A. Anderson, John C. Tannehill, R. H. P., *Computational Fluid Mechanics and Heat Transfer*. Washington: Hemisphere Publishing.

[14] (Ed.), D. R. L., *CRC Handbook of Chemistry and Physics*. Coca Raton, FL: CRC.

[15] Eggers, J. *Phys. Rev. Lett.*, vol. **71**, p. 3458, 1993.

[16] Eggers, J. *Phys. Fluids*, vol. 7, p. 941, 1995.

[17] Eggers, J. *Rev. Mod. Phys.*, vol. **69**, p. 865, 1997.

[18] Eggers, J. *Phys. Rev. Lett.*, vol. **89**, p. 084502, 2002.

[19] F. J. Garcia, A. C. *Phys. Fluids*, vol. **6**, p. 2676, 1994.

[20] F. Song, L. He, H. Z. J. W. J. Z. G. W. *Appl. Phys. Lett.*, vol. 89, p. 193104, 2006.

[21] Feynman, R. P. *Phys. Rev.*, vol. **56**, p. 340, 1939.

[22] Furth, P. A. *Mol. Biotechnol.*, vol. 7, p. 139, 1997.

[23] G. C. Fox, M. A. Johnson, G. A. L. S. W. O. J. K. S. D. W. W., *Solving Problems on Concurrent Processors*, vol. 1. Englewood Cliffs, NJ: Prentice hall, 1988.

[24] H. Goldstein, C. Poole, J. S., *Classical Mechanics*. Reading, MA: Addison Wesley.

[25] Hentschel, H. G. E. and Family, F. *Phys. Rev. Lett.*, vol. **66**, p. 1982, 1991.

[26] Hu, G., *Stochastic forces and nonlinear systems*. Shanghai, China: Shanghai Scintific and Technological Education.

[27] J. B. Keller, M. J. M. *SIAM J. Appl. Math.*, vol. **43**, p. 268, 1983.

[28] J. Barojas, D. L. *Phys. Rev. A*, vol. **7**, p. 1092, 1973.

[29] J. Eggers, T. F. D. *J. Fluid Mech.*, vol. **262**, p. 205, 1994.

[30] J. Gao, W. D. Luedtke, U. L. *Science*, vol. **270**, p. 605, 1995.

[31] J. Garcia-Ojalvo, J. M. S., *Noise in spatially extended systems*. New York: Springer.

[32] J. I. Siepmann, S. Karaborni, B. S. *Nature*, vol. **365**, p. 330, 1993.

[33] J. Koplik, T. S. Lo, M. R. *Phys. Fluids*, vol. 18, p. 032104, 2006.

[34] J. Koplik, R. B. *Phys. Fluids A*, vol. **5**, p. 521, 1992.

[35] J. P. Ryckaert, A. B. *Chem. Phys. Lett.*, vol. **30**, p. 123, 1975.

[36] John D. Anderson, J., *Computational fluid dynamics: the basics with applications*. New York: McGraw-Hill.

[37] Johnson, R. A. *Phys. Rev. B*, vol. **37**, p. 3924, 1988.

[38] Johnson, R. A. *Phys. Rev. B*, vol. **39**, p. 12554, 1989.

[39] K. Kadau, C. Ronsenblatt, J. L. B. T. C. G. Z. H. P. C. B. J. A. *Proc. Natl. Acad. Sci. USA*, vol. **104**, p. 7741, 2007.

[40] K. Kadau, T. C. Germann, N. G. H. P. S. L. G. D. B. L. H. B. J. A. *Proc. Natl. Acad. Sci. USA*, vol. **101**, p. 5851, 2004.

[41] Kadanoff, L. P., *Statistical Physics: Statics, Dynamics and Renormalization*. Singapore: World Scientific.

[42] Kawano, S. *Phys. Rev. E*, vol. **58**, p. 4468, 1998.

[43] Kolmogorov, A. N. *Proc. R. Soc. Lond. A*, vol. **434**, p. 9, 1991.

[44] Koplik, J. *Phys. Fluids A*, vol. **5**, p. 521, 1993.

[45] Kowalewski, T. A. *Fluid Dyn. Res.*, vol. **17**, p. 121, 1996.

[46] Kramers, H. A. *Physica*, vol. **7**, p. 284, 1940.

[47] Kuo, K., *Recent Advances in Spray Combustion: Spray Atomization and Drop Burning Phenomena*, vol. 1 and 2. Reston, VA: American Institute of Aeronautics and Astronautics, 1996.

[48] L. D. Landau, E. M. L., *Fluid Mechanics*. Oxford, UK: Pergamon.

[49] L. D. Landau, E. M. L., *Statistical Physics*. Oxford: Pergamon.

[50] Lin, S. P., *Breakup of Liquid Sheets and Jets*. Cambridge: Cambridge University.

[51] M. C. Cross, P. C. H. *Rev. Mod. Phys.*, vol. 65, p. 851, 1993.

[52] M. J. Stott, E. Z. *Phys. Rev. B*, vol. **22**, p. 1564, 1980.

[53] M. Mondellon, G. S. G. *J. Chem. Phys.*, vol. **103**, p. 7156, 1995.

[54] M. Moseler, U. L., "private notes,"

[55] M. Moseler, U. L. *Science*, vol. **289**, p. 1165, 2000.

[56] M. P. Allen, D. J. T., *Computer Simulation of Liquids*. Oxford: Clarendon.

[57] M. S. Daw, M. I. B. *Phys. Rev. Lett.*, vol. **50**, p. 1285, 1983.

[58] M. S. Daw, M. I. B. *Phys. Rev. B*, vol. **29**, p. 6443, 1984.

[59] Ma, S. K., *Modern Theory of Critical Phenomena*. Reading, Massachusetts: Benjamin/Cummings.

[60] McQuarrie, D. A., *Statistical Mechanics*. New York: Harper and Row.

[61] Meakin, P., *Fractals, scaling and growth far from equilibrium*. Cambridge, UK: Cambridge University.

[62] Middleman, S., *Modeling axisymmetric flows: dynamics of films, jets and drops*. San Diego: Academic Press.

[63] Moyal, J. E. *J. Roy. Stat. Soc. (London)*, vol. **B11**, p. 150, 1949.

[64] Mullins, W. W. *J. Appl. Phys.*, vol. 28, p. 333, 1957.

[65] N. W. Ashcroft, N. D. M., *Solid State Physics*. Saunders College, PA: Brooks Cole.

[66] Ott, E., *Chaos in dynamical systems*. Cambridge, UK: Cambridge University.

[67] P. Hohenberg, W. K. *Phys. Rev. B*, vol. **136**, p. 864, 1964.

[68] P. van der Ploeg, H. J. C. B. *J. Chem. Phys.*, vol. **76**, p. 3271, 1982.

[69] Pankaj Doshi, Itai Cohen, W. W. Z. *Science*, vol. 302, p. 1185, 2003.

[70] Plimpton, S. *J. Comput. Phys.*, vol. **117**, p. 1, 1995.

[71] R. G. Parr, W. Y., *Density-Functional Theory of Atoms and Molecules*. New York: Oxford University.

[72] Rahman, A. *Phys. Rev. A*, vol. **136**, p. 405, 1964.

[73] Rayleigh, W. S. *Proc. Lond. Math. Soc.*, vol. **4**, p. 10, 1878.

[74] Reichl, L. E., *A Modern Course in Statistical Physics*. New York: Jones Wiley & Sons.

[75] Reynolds, O. *Philos. Trans. R. Soc. London*, vol. 177, p. 157, 1886.

[76] Reynolds, O. *Proc. R. Soc. London*, vol. 40, p. 191, 1886.

[77] Risken, H., *The Fokker-Plank Equation: Methods of Solution and Applications*. Berlin, Germany: Springer.

[78] S. E. Bechtel, M. G. Forest, K. J. L. *stability appl. anal. continuous media*, vol. **2**, p. 59, 1992.

[79] S. Murad, I. K. P. *Nano Lett.*, vol. 7, p. 707, 2007.

[80] Smit, B. *J. Chem. Phys.*, vol. **96**, p. 8639, 1992.

[81] Stratonovich, R. L., *Topics in the Theory of Random Noise*. New York: Gordon and Breach, 1967.

[82] T. Halicioglu, G. M. P. *Phys. Stat. Sol. (a)*, vol. **30**, p. 619, 1975.

[83] T. K. Xia, J. Ouyang, M. W. R. U. L. *Phys. Rev. Lett.*, vol. **69**, p. 1967, 1992.

[84] V, Mironov, N. R. B. D. *Tissue Eng.*, vol. 12, p. 631, 2006.

[85] V. Mironov, N. Reis, B. D. *Tissue Eng.*, vol. **12**, p. 631, 2006.

[86] Verlet, L. *Phys. Rev.*, vol. **159**, p. 98, 1967.

[87] W. C. Swope, H. C. Andersen, P. H. B. K. R. W. *J. Chem. Phys.*, vol. **76**, p. 637, 1982.

[88] W. Kohn, L. J. S. *Phys. Rev.*, vol. **140**, 1965.

[89] W. L. Jorgensen, J. D. Madura, C. J. S. *J. Am. Chem. Soc.*, vol. **106**, p. 6638, 1984.

[90] Weber, C. *Z. angew. Math. Mech.*, vol. **190**, p. 561, 1931.

[91] Wei Kang, U. L., "summary," *unpublished*.

[92] Wei Kang, U. L. *Phys. Rev. Lett.*, vol. **98**, p. 064504, 2007.

[93] Williams, C. *Physics World*, vol. **19**, p. 24, 2006.

[94] Williams, C. *Physics World*, vol. 19, p. 24, 2006.

[95] X. D. Shi, Michael P. Brenner, S. R. N. *Science*, vol. **265**, p. 219, 1994.

[96] Y. Hennequin, D. G. A. L. Aarts, J. H. v. d. W. *Phys. Rev. Lett.*, vol. 97, p. 244502, 2006.

[97] Yarin, A. L., *Free Liquid Jets and Films: Hydrodynamics and Rheology*. Essex, UK: Longman.

# VITA

Wei Kang was born on August 3rd, 1976 in Ji'an, Jiangxi Province, China. He started his study of physics at Department of Physics of Beijing Normal University, Beijing, China in 1994. After 7 years, he received a Bachelor degree and a Master degree of Science there. In 2001, he went to Liquid Crystal Institute at Kent State University, Ohio, USA to study liquid crystal and soft condensed matter. After a short period, in the fall of 2002, he transferred to School of Physics, Georgia Institute of Technology, Georgia, USA, and since 2003, he has been working with Professor Uzi Landman on molecular dynamics simulations and microscopic hydrodynamics of nanoscale liquid structures for his PhD thesis.